

**Application of microfluidics in the study of bilateral sensory neurons of *C. elegans* and femtolitre-droplet based single-molecule-counting immunoassay for renal graft failure detection**

Jinyang Chung

Submitted in accordance with the requirements for the degree of  
Doctor of Philosophy

The University of Leeds

School of Physics and Astronomy

August 2019

## Intellectual Property Statement

The candidate confirms that the work submitted is his own and that appropriate credit has been given where reference has been made to the work of others.

This copy has been supplied on the understanding that it is copyright material and that no quotation from the thesis may be published without proper acknowledgement.

The right of Jinyang Chung to be identified as Author of this work has been asserted by Jinyang Chung in accordance with the Copyright, Designs and Patents Act 1988.

© 2019 The University of Leeds and Jinyang Chung

## **Acknowledgements**

First of all, I would like to give the best gratitude to my supervisor, Dr Jung-uk shim, who graciously accepted me into his team. He provided me with invaluable guidance, which was critical for myself who did not have a physics background. I would not able to complete the research without his support, encouragement and critical advice. Also, I appreciate my co-supervisor Professor Stephen Evans for advice and encouragement throughout my PhD.

I appreciate Professor Netta Cohen for critical discussion on the overall study of *C. elegans*. This research has been carried out by a team which has included Christopher A. Brittin. My own contribution, fully and explicitly indicated in the thesis, has been the development of microfluidic device and operation of the system. The other members of the group and their contribution have been as follows, the molecular biology for *C. elegans*, and development of flow controlling and imaging software.

Also, I would like to thank Liam Hunter in the same group sharing ideas and carrying out the experiment together, especially for the femtodroplet study.

Thanks all in Molecular Nano Physics group in Leeds. Not only having critical discussions at the meeting, but I also had inspiration during daily talks in the university. Also, being alone in the UK, the warm-hearted MNPeople encouraged me a lot until I finish the research.

Finally, I would like to express my gratitude and love to all my family members, my parents and brother, who supported through all my many years of school.

## **Abstract**

Microfluidics has been instrumental in studying biological process and biomedical applications. This thesis covers application of microfluidics to in-vivo neuroscience and disease diagnostics.

The nematode *Caenorhabditis elegans* is a leading model system for studying in genetics, development and neurobiology. How one animal takes information of environment and transduces it into one's behaviour is one of the large questions in the field of neuroscience. With the exception of whole-brain imaging studies, simultaneous imaging studies for one or more pairs of bilateral neurons has been avoided since the animal lies on its left or right side. This limits our understanding of symmetry and asymmetry in sensory response and information flow.

We develop rotatable (PDMS) microfluidic device denoted the side view chip that allows us to image a pair of bilateral neurons in a single focal plane of an epi-fluorescence microscope. We prove the utility of the device by recording the responses of immobilised worms to controlled stimuli, focusing on the responses of two classes of head sensory neurons to changes in NaCl concentration. This can pave the way for researching laterally parallel neurocircuit

Then, we expand the idea to develop another microfluidic device to study how the pair of asymmetric sensory neurons encode the head movement to establish chemotaxis behaviour to NaCl. The device aims to trap the worm with its head allowed to freely move around and treat the gradient of the stimulus from the left to the right of the head of the worm. Reinforced trap for partial immobilisation of the nematode and a module for transposing the flow is developed.

Diagnosing disease in early stage increases effectiveness in treatment. To achieve this, a platform development for detecting low abundant biomarker is required. Prostate cancer specific antigen (PSA) is investigated using immunoassay in microfluidic platform. The components of the immunoassay have been characterised.

## Table of Contents

<b>Acknowledgements</b> .....	<b>iii</b>
<b>Abstract</b> .....	<b>iv</b>
<b>Table of Contents</b> .....	<b>v</b>
<b>List of Tables</b> .....	<b>ix</b>
<b>List of Figures</b> .....	<b>x</b>
<b>List of Abbreviations</b> .....	<b>xiii</b>
<b>Chapter 1 Introduction</b> .....	<b>1</b>
1.1 Microfluidics .....	1
1.1.1 Laminar flow and diffusion.....	3
1.1.2 Fabrication of the microfluidic device .....	4
1.1.3 Flow controls .....	5
1.1.3.1 Syringe pump and pressure system.....	5
1.1.3.2 Back-pressure.....	5
1.1.4 Droplet formation.....	6
1.1.5 Femtolitre droplets .....	6
1.2 <i>Caenorhabditis elegans</i> .....	6
1.2.1 The nervous system of <i>C. elegans</i> .....	7
1.2.1.1 Neurocircuit of <i>C. elegans</i> .....	7
1.2.1.2 Signal transduction pathway to initiate the depolarisation.....	9
1.2.1.3 Synapse .....	10
1.2.1.4 Gap junctions .....	10
1.2.1.5 Head sensory neuron of <i>C. elegans</i> .....	11
1.2.2 Chemotaxis .....	12
1.2.3 ASH neurons.....	12
1.2.4 ASE neurons .....	14
1.2.5 Cell visualisation and measurement of neuroactivity of <i>C.</i> <i>elegans</i> .....	15
1.2.6 Imaging system for tracking the activity of neurons.....	15
1.2.7 Fast 3d imaging of neural activity .....	17
1.2.8 Microfluidic device for the study of <i>C. elegans</i> .....	18
1.2.8.1 Worm immobilisation.....	18
1.2.8.2 Worm immobilisation with controlled orientation .....	20

1.2.8.3	The behaviour of the worm in microfluidic devices.....	23
1.2.8.4	Other applications of microfluidics in <i>C. elegans</i> study .....	24
1.3	Femtolitre droplet and single-molecule assay .....	25
1.3.1	Single-molecule analysis using femtolitre chamber.....	25
1.3.2	Single-molecule immunoassays .....	26
1.3.3	Limit of detection .....	27
1.3.4	Renal transplantation rejection.....	28
1.4	Overview .....	29
<b>Chapter 2</b>	<b>Methodology.....</b>	<b>31</b>
2.1	Microfabrication.....	31
2.1.1	Overview of the PDMS device fabrication .....	31
2.1.2	Multilayer master and PDMS device .....	34
2.1.2.1	Multilayer master.....	34
2.1.2.2	Multilayer PDMS device fabrication .....	34
2.2	Fluid control.....	36
2.2.1	Air-pressure driven fluid control.....	36
2.2.2	Worm loading and treating stimulus flow to the amphid of the immobilised <i>C. elegans</i> .....	37
2.3	Image acquisition and analysis .....	38
2.3.1	Fluorescence image acquisition .....	38
2.3.2	Tracking and calcium image analysis of the bilateral sensory neurons of <i>C. elegans</i> .....	38
2.4	Molecular biology and culture of <i>C. elegans</i> .....	39
2.4.1	Molecular biology .....	39
2.4.2	Worm culture and screening .....	39
2.5	Femtodroplet immunoassay .....	40
2.5.1	Enzyme reaction kinetics .....	40
2.5.2	Fluidic setup and valve operation for femtodroplet immunoassay device.....	40
2.5.3	Measurement enzyme reaction in the femtolitre droplet .....	41
2.5.4	Capture bead preparation and immunocomplex formation .....	41
2.5.5	Immunoassay in the femtolitre droplet .....	43

<b>Chapter 3</b>	<b>Development of rotatable microfluidic device and simultaneous study of bilateral sensory neurons in <i>C. elegans</i></b>	<b>45</b>
3.1	Introduction .....	45
3.2	Device fabrication.....	46
3.2.1	<i>C. elegans</i> was injected into a straight PDMS device .	46
3.2.2	The 1 <sup>st</sup> design of the device .....	47
3.2.2.1	A modified straight device with diverted inlet and traps .....	47
3.2.2.2	T device .....	48
3.2.3	Trap design .....	49
3.2.4	Rotatable device .....	52
3.2.4.1	Device fabrication .....	52
3.2.5	Surface treatment of side view device to enhance the transparency .....	53
3.2.5.1	Time course imaging of ASH neuron response .....	55
3.2.6	A new design of side-view device .....	57
3.2.7	Master fabrication for side view device .....	62
3.2.8	Fluorescence acquisition.....	66
3.3	Simultaneous measurement for the response of ASE neurons to the stimulus .....	68
3.4	Simultaneous measurement of the response of ASH neurons to the stimulus .....	70
3.4.1	Cross-Correlation between ASHL and ASHR .....	72
3.4.2	Independence test between ASH left and right neurons .....	73
<b>Chapter 4</b>	<b>Development of a microfluidic device for imaging head movement and neuronal activity of bilateral sensory neuron</b>	<b>79</b>
4.1	Introduction .....	79
4.2	Development of the wormhead device to image bilateral sensory neuron and the head movement.....	79
4.2.1	Multidepth channel fabrication using two PDMS blocks .....	79
4.2.2	Development of flow transposition module.....	80
4.2.3	Design of the wormhead device .....	84
4.2.4	Master fabrication for the wormhead device .....	87
4.2.5	Fork operation .....	89

4.2.6	Flow test.....	91
4.3	Conclusion .....	95
<b>Chapter 5</b>	<b>Immunoassay in femtolitre-sized droplet .....</b>	<b>96</b>
5.1	Introduction .....	96
5.2	Validation of microfluidic device for femtodroplet immunoassay .....	96
5.3	Measurement of the catalytic reaction rate of free $\beta$ -galactosidase and streptavidin conjugated $\beta$ -galactosidase.....	99
5.4	Enzyme reaction in the droplet.....	101
5.5	Bead-based immunocomplex construction and femtodroplet immunoassay .....	106
5.5.1	Capture bead construction .....	106
5.5.2	Qualification of the conjugation by intrinsic fluorescence of the protein .....	106
5.5.3	Estimation of the amount of capture antibody bound on the microbead. ....	109
5.5.4	Femtodroplet Immunoassay.....	109
5.6	Conclusion .....	111
<b>Chapter 6</b>	<b>Discussion and conclusion.....</b>	<b>112</b>
<b>Reference.....</b>		<b>115</b>

## List of Tables

<b>Table 1.1 Head sensory neurons. ....</b>	<b>11</b>
<b>Table 5.1 Finding the condition of PDMS spin coating on the master for the bottom layer.. ....</b>	<b>99</b>

## List of Figures

<b>Figure 1.1</b> Numbers of published articles including the keyword 'microfluid' on Web of Science. ....	<b>2</b>
<b>Figure 1.2</b> Signal transduction pathways in a) ASE chemosensory neurons and b) ASH neurons. ....	<b>9</b>
<b>Figure 1.3</b> a) The scheme of the neurons in the head of <i>C. elegans</i> (lateral view) (b) 3D scheme of ASE and ASH neuron. ....	<b>13</b>
<b>Figure 1.4</b> Scheme of the Image-free, optomechanical system. ....	<b>16</b>
<b>Figure 1.5</b> Scheme of light-field microscopy. ....	<b>17</b>
<b>Figure 1.6</b> Example of confocal microscopy setup for imaging multiple neurons in the brain of <i>C. elegans</i> .....	<b>18</b>
<b>Figure 1.7</b> Previous study of <i>C. elegans</i> immobilisation. ....	<b>20</b>
<b>Figure 1.8</b> Orientation of the body of <i>C. elegans</i> . ....	<b>21</b>
<b>Figure 1.9</b> Example of microfluidic system for multiangle imaging of <i>C. elegans</i> . ....	<b>22</b>
<b>Figure 1.10</b> smooth-sided PDMS devices for multi-angle imaging. ....	<b>23</b>
<b>Figure 1.11</b> Compartmentalisation for single-molecule analysis. ....	<b>26</b>
<b>Figure 2.1</b> Scheme of PDMS device fabrication. ....	<b>33</b>
<b>Figure 2.2</b> Scheme of the process to fabricate multilayer master. ....	<b>35</b>
<b>Figure 2.3</b> Scheme of the process to fabricate a Multilayer PDMS device. ....	<b>36</b>
<b>Figure 2.4</b> solenoid valve controller. ....	<b>37</b>
<b>Figure 2.5</b> The scheme of bioconjugation for capture bead construction. ....	<b>43</b>
<b>Figure 2.6</b> Scheme of the immunocomplex formed on a capture bead. ....	<b>44</b>
<b>Figure 3.1</b> Movement of the worm in a straight PDMS channel. ....	<b>46</b>
<b>Figure 3.2</b> GCaMP fluorescence in ASH neuron of CX10979 strain in the microfluidic channel. ....	<b>47</b>
<b>Figure 3.3</b> Scheme of modified straight device and image of the worm in the channel. ....	<b>48</b>
<b>Figure 3.4</b> Scheme of T device and images of the worm in the channel. ....	<b>49</b>
<b>Figure 3.5</b> Measurement of the size of the worm for the trap modification .....	<b>50</b>
<b>Figure 3.6</b> Revision of the trap design .....	<b>51</b>
<b>Figure 3.7</b> Scheme of Side-view T device and images of the worm in the channel. ....	<b>52</b>

<b>Figure 3.8</b> a) Scheme of side view device fabrication. b) Top view and side view setup of the side-view device on a microscope. ....	<b>54</b>
<b>Figure 3.9</b> Side view images of the channel a) before and b) after smoothing.. ..	<b>55</b>
<b>Figure 3.10</b> Multiangle image of the worm immobilised in the side view chip. ....	<b>55</b>
<b>Figure 3.11</b> Time course imaging of the ASH neuron.....	<b>56</b>
<b>Figure 3.12</b> Interface formed between stimulus and buffer flow. ....	<b>57</b>
<b>Figure 3.13</b> Scheme of the microfluidic system for side view device ..	<b>58</b>
<b>Figure 3.14</b> Side view device (left) and the fluorescence images of the immobilised worm in the device (right). ....	<b>59</b>
<b>Figure 3.15</b> Semi-automatic delivery device.....	<b>59</b>
<b>Figure 3.16</b> The broad entrance region of the worm trap. ....	<b>60</b>
<b>Figure 3.17</b> Distribution of the twisted angle of immobilised worms ...	<b>62</b>
<b>Figure 3.18</b> Stimulus redirection. ....	<b>62</b>
<b>Figure 3.19</b> Master image dependent on UV dose and baking time. ..	<b>63</b>
<b>Figure 3.20</b> Master image dependent on the length of post-exposure bake. ....	<b>64</b>
<b>Figure 3.21</b> SU-8 photoresist pattern partially detached from the silicon wafer. ....	<b>64</b>
<b>Figure 3.22</b> OmniCoat™ treatment.....	<b>65</b>
<b>Figure 3.23</b> Comparison of Two-step bake and Ramping bake.....	<b>65</b>
<b>Figure 3.24</b> The 1st method of ROI setting.....	<b>66</b>
<b>Figure 3.25</b> Fluorescence of the axon extends to the other side. ....	<b>67</b>
<b>Figure 3.26</b> The 2 <sup>nd</sup> method of ROI setting.....	<b>67</b>
<b>Figure 3.27</b> Neuronal activity of ASEL and ASER in response to upstep and downstep of the NaCl concentration, between 50 mM and 100 mM for 120-second duration .....	<b>69</b>
<b>Figure 3.28</b> Neuronal activity of ASHL and ASHR within <i>C. elegans</i> in response to a 3-second pulse of NaCl. ....	<b>72</b>
<b>Figure 3.29</b> Cross-correlation of the responsive ASHL and ASHR. ....	<b>73</b>
<b>Figure 3.30</b> Fisher's exact test. ....	<b>74</b>
<b>Figure 3.31</b> The measured fraction of the synchronous neuron pairs compared with the calculated probability of synchrony. ....	<b>76</b>
<b>Figure 3.32</b> <i>inx-19</i> knock-out strain. ....	<b>77</b>
<b>Figure 4.1</b> Multilayer PDMS device fabrication for multiple depths of the channel. ....	<b>80</b>
<b>Figure 4.2</b> Master design of the flow transposing channel.....	<b>81</b>
<b>Figure 4.3</b> Transposition of the flow.....	<b>83</b>

<b>Figure 4.4</b> Fluorescence intensity through z-axis of the channel after transposition.....	84
<b>Figure 4.5</b> a) Cross-sectional scheme of the device and the master design. b) Scheme of the device.....	86
<b>Figure 4.6</b> Master for layer 1 and layer 3.....	88
<b>Figure 4.7</b> Issue 1 in the multi-layer master fabrication (layer 2). 35 $\mu\text{m}$ pattern and 160 $\mu\text{m}$ pattern are not aligned. ....	88
<b>Figure 4.8</b> Width of the trap depending on the applied pressure to the fork. ....	90
<b>Figure 4.9</b> The half-immobilised worm in the trap.....	91
<b>Figure 4.10</b> Flow at the redirection module with the pressure of 5 psi in the supply flow ((1) and (2)). ....	92
<b>Figure 4.11</b> Flow at the redirection module with the pressure of 10 psi in the supply flow ((1) and (2)).....	93
<b>Figure 4.12</b> Flow at the redirection module in the device without multidepth channel.....	94
<b>Figure 4.13</b> Vertical gradient was not formed.....	94
<b>Figure 5.1</b> The scheme of the femtodroplet immunoassay device .....	97
<b>Figure 5.2</b> The scheme of the femtodroplet immunoassay device.. ...	98
<b>Figure 5.3</b> Kinetic study of streptavidin- $\beta$ -galactosidase. ....	101
<b>Figure 5.4</b> Fluorescein production by $\beta$ -galactosidase in the femtodroplets.. ....	104
<b>Figure 5.5</b> Enzyme reaction in femtodroplet. ....	105
<b>Figure 5.6</b> Autofluorescence of the polystyrene microbead and capture bead.....	108
<b>Figure 5.7</b> Femtodroplet immunoassay. ....	111
<b>Figure 6.1</b> 3D device for horizontal interface.....	114

## List of Abbreviations

BSA	bovine serum albumin
CTX buffer	Chemotaxis buffer
ELISA	enzyme-linked immunosorbent assay
EMCCD	Electron-multiplying charge-coupled device
FDG	fluorescein-di- $\beta$ -D-galactopyranoside
FMG	fluorescein-monogalactopyranoside
GABA	Gamma-aminobutyric acid
GFP	Green fluorescence protein
LOD	Limit of detection
MALDI-MS	matrix-assisted laser desorption/ionisation mass spectrometry
MHC	Major histocompatibility complex
MSC-MS	microchip electrophoresis mass spectrometry
NGM	Nematode growth medium
PBS	Phosphate buffered saline
PC	poly(carbonate)
PCR	Polymerase chain reaction
PDMS	polydimethylsiloxane
PMMA	poly(methyl methacrylate)
PSA	Prostate specific antigen
PTFE	polytetrafluoroethylene
PUFAs	polyunsaturated fatty acids.
RFP	Red fluorescent protein
RT	room temperature
UV	Ultraviolet

## Chapter 1 Introduction

### 1.1 Microfluidics

Microfluidic technology has increased dramatically in the last three decades. It is the scientific and technological field that processes low volumes (nano litres and picolitres) of fluids in channels with dimensions on the micrometre to the nanometer scale.[1] Microfluidics has been regarded as revolutionary technique, especially in the processes that are difficult or even impossible to achieve in macro-scale. The scientific and technological discussions have been discussed based on several review articles [2-8]. There are reasons why microfluidic technology experiences such demands.

First, the flow in the microchannel is typically laminar. Therefore, precise control comparing to bulk process is available. The mixing occurs only by diffusion at the interface between two fluids in laminar environment. Conversely, the faster mixing can be achieved by integrating mixers[9-11].

Second, reaction time is considerably decreased due to the shorter diffusion distances in the confined spaces of a microchannel, giving better mass transfer. Also, the high surface to volume ratios provide faster heat transfer. For example, polymerase chain reaction (PCR), the well-known technique, has been realised on-chip scale. Kopp *et al.* reported 20 cycle PCR application of 176-pair fragment of DNA in the reaction times of 90 seconds to 18.7 minutes.[12] The same amplification using typical PCR system, in microlitre scale tubes, takes a couple of hours.

Third, various devices can be integrated into the microfluidic device. For example, pumps and valves for fluid control, electrodes for electrochemical sensor or particle manipulation, any magnetised components.

Fourth, microfluidics enables use of a minimal volume of solution to perform operations which would require greater volumes in the macro system. Conventional macroscale procedures such as an assay performed in an Eppendorf tube is considered as “small volumes” and typically requires microlitre scale, whereas on-chip the same assay would occur in nano- to picolitre scale, or less. Using smaller volumes can be also beneficial for safety as the performer would handle a small amount of hazardous material.[13]

With these advantages, microfluidics has experienced popularity. Base on the Web of Science search for the keyword 'microfluid', resulted in 232 publications in 2000, yields 2,740 in 2010 and reaches 4,603 in 2018 (**figure 1.1**).

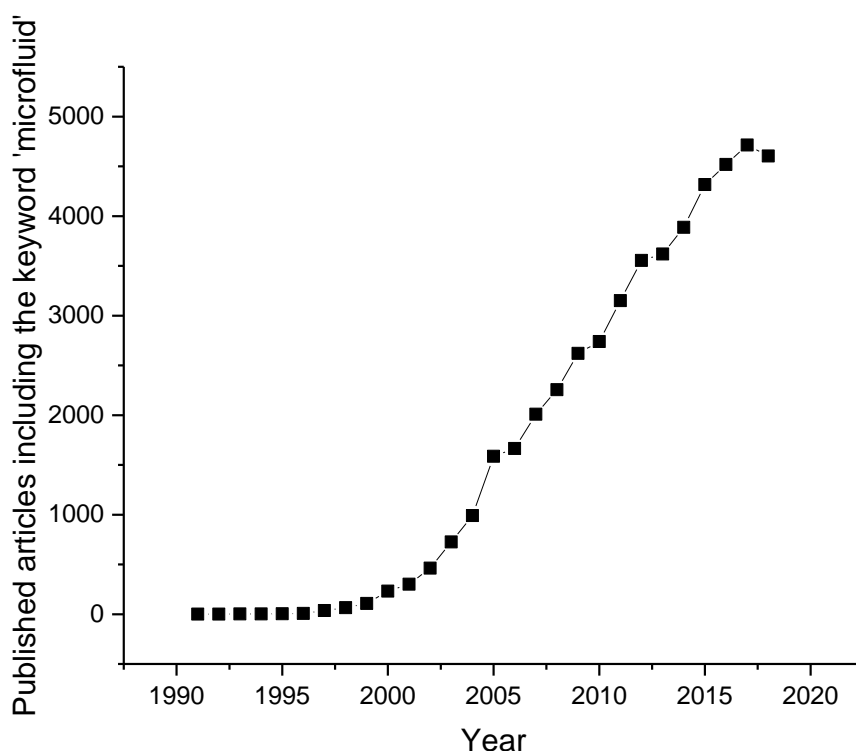


**Figure 1.1** Numbers of published articles including the keyword 'microfluid' on Web of Science. (Accessed on the 21<sup>st</sup> February 2019)

Microfluidic systems have been used extensively as promising experimental and manufacturing tools in the fields of chemistry [10, 14], biotechnology [15], diagnosis [16], pharmaceuticals [17], and environmental engineering [18], interrogating of cells [19], tissue [20], and even small animals such as *C. elegans* and *Drosophila melanogaster* [21, 22].

Microfluidics has been applied to DNA studies such as the polymerase chain reaction (PCR) and gene sequencing. It is used in PCR to decrease volume and simplify the process and developed to perform single-DNA amplification in the 1990s.[23] Since then, the technology has been commercialised (e.g., Fluidigm, Bio-Rad etc.) and used in clinical studies, for instance, in diagnosing genetic disorders. Tsui *et al.* diagnosed haemophilia in a foetus by detecting foetal genotypes from maternal plasma samples using microfluidic digital PCR.[16] Additionally, microfluidics technology has been applied to the first-

generation of sequencing for automation and parallelisation of the process and computation of the analysis. Margulies *et al.* developed a system to isolate and amplify DNA fragments by an emulsion-based method and to perform pyrosequencing in picolitre-sized wells.[24] Since then, lab-scale gene sequencing equipment using microfluidics has been produced (e.g., Fluidigm).

Microfluidics has been also applied in drug screening by controlling single cells. Wang *et al.* developed a microfluidic hydrodynamic trapping system for single-cell assays in anticancer drug screening with ~90% single-cell trapping efficiency.[17] In this study, single HeLa cells were trapped in the microfluidic device and the responses from five different clinical chemotherapeutic reagents were observed successfully.

Microfluidics has been applied in environmental bacteria screening. Chung *et al.* applied a microfluidics platform for continuous detection of environmental indicator bacteria using aptameric conjugated fluorescent nanoparticles.[18] *E. coli* labelled with aptameric conjugated nanoparticles were injected into a microchannel. The labelled microorganism was excited by a fibre-coupled laser and fluorescence emitting from tagged bacteria was measured quantitatively by a photon counter.

Microfluidic devices have been integrated into analytical devices to enhance speed and resolution in the analysis. Currently, Li *et al.* have developed microchip electrophoresis mass spectrometry (MSC-MS) by connecting the microfluidic device to electrospray ionization mass spectrometry to study chiral analysis.[25] Enantiomeric separation of three neuroactive compounds, i.e., 3,4-dihydroxyphenylalanine (DOPA), glutamic acid (Glu), and serine (Ser), were achieved within 3 min and stereochemical preference in living neuronal cells was studied. Additionally, Küster *et al.* integrated matrix-assisted laser desorption/ionisation mass spectrometry (MALDI-MS) with droplet-based microfluidic systems and studied the concentration change of angiotensin I and II through the reaction of an angiotensin-converting enzyme.[26]

### **1.1.1 Laminar flow and diffusion**

Mixing chemicals in a batch container is achieved via turbulence in the liquid, in which the flow is unstable and chaotic. However, laminar flow dominates in the microfluidic system, with a well-defined interface between two flows. The mixing between solutions occurs only due to the diffusion into each other in laminar flow.

Laminar flow occurs when the viscous forces dominate the inertial forces in the system.[27] Reynold number (Re) is the calculation for determining whether the flow is laminar or turbulent, as shown in equation 1.1

$$Re = \rho v D_h / \eta \quad (\text{Equation 1.1})$$

, where  $\rho$  is the density of the fluid,  $v$  is the velocity of the fluid,  $\eta$  is its dynamic viscosity, and  $D_h$  is the hydraulic diameter.

Hydraulic diameter ( $D_h$ ) is calculated as equation 2 [28]

$$D_h = 4A / P \quad (\text{Equation 1.2})$$

, where  $A$  is the cross-sectional area of the channel, and  $P$  is the wetted perimeter of the channel. The laminar flow occurs when Re is smaller than 2,300, and turbulent flow occurs when Re is larger than 2,900.[29, 30] The flow systems we used in this study have the Re between 0.1 and 20, which are in the range of laminar flow.

Diffusion time is dependent on distance and molecular characteristics and can be determined using the Einstein-Smoluchowski equation as shown in Equation 3.[31]

$$t = d^2 / 2D \quad (\text{Equation 1.3})$$

, where  $t$  is the diffusion time,  $d$  is the extent of diffusion of a molecule, and  $D$  is the diffusion coefficient. For example, it takes 3.5 hours for a 5-nm-diameter protein with a diffusion coefficient of  $40 \mu\text{m}^2 / \text{s}$  to travel 1 mm. This parameter can be used to determine the size of the device and the reaction time of biochemical reactions in the device.

### 1.1.2 Fabrication of the microfluidic device

Microfluidic devices can be fabricated from a number of materials, depending on the desired properties. Glass is selected due to its optical transparency and stability to harsh chemicals.[32] This is fabricated using photolithography and wet etching method. Transparent polymers, on the other hand, have become popular due to their economic and fast production, although it is less stable than glass device.[33] The rapid-prototyping procedure for soft-lithography enables shortening of the time to less than one day for the fabrication of the master from the designed pattern and soft-lithography to mould the polymer device.[34] Various polymers have been introduced, including poly(carbonate) (PC) [35], poly(methyl methacrylate) (PMMA) [36-38] and cyclic olefin copolymer (COC) [39] and poly(dimethylsiloxane) (PDMS) [40, 41].

Among polymers, poly(dimethylsiloxane) (PDMS) has several advantages when it is used for biological application in aqueous solution. (i) Microchannels can be made by replica moulding with high fidelity; (ii) PDMS is optically transparent in UV/Visible light; (iii) PDMS cures in low temperature and is non-toxic; (iv) its surface chemistry can be altered easily; (v) it is elastomeric [42].

### 1.1.3 Flow controls

The standard method to supply liquid into the device is to use syringe pumps and pressure system.

#### 1.1.3.1 Syringe pump and pressure system

A syringe pump is the most common system to inject liquid into microfluidic devices. Based on a linear actuator system composed of a stepper motor and a lead screw, the pumps compress a set of syringes connected to the device containing the purposed liquid to supply the microfluidic system. The syringe pumps are operated with controlled volumetric flow rates. The simplicity and robustness of the system ensure the longevity, and using syringes enables to use of large volumes (This is dependent on the volume of the syringe). On the other hand, the syringe pump is often inappropriate to use for the condition that consistent pressure is critical. For example, when an organism is delivered into the trap using a syringe pump, and eventually the immobilised worm blocks the channel, internal pressure would increase until the worm is pressed and flushed out.

A pressure system is operated by a pressurised liquid storage chamber. The liquid is flown and controlled by valves out of the device or installed into the microfluidic system. A high-cost system such as Elveflow made by Fluigent has valves which are controlled by a feedback loop for stable flow rates. The principal advantage of the pressure system is the quick response times, typically on the order of 100 ms. Moreover, the volume flow rate is very stable. On the other hand, the pressure system is not the first selection for systems which need to control flow rate. An additional flow sensor is required to control the flow rate in the pressure system.

#### 1.1.3.2 Back-pressure

Continuous flow in the narrow microfluidic channel induces back-pressure. It is estimated from Poiseuille's law.

$$\Delta P = \frac{8\mu LQ}{\pi r^4} \quad (\text{Equation 1.4})$$

, where  $\Delta P$  is the pressure drop,  $\mu$  is the viscosity, L is the length of the channel, Q is the volumetric flow rate, and r is the radius of the channel. Strong

hydrodynamic backpressure can induce issues such as delamination of the device, expansion of the device made of elastic material and tubing connection failure while operating the microfluidic device.

#### 1.1.4 Droplet formation

Droplet generation takes place at a nozzle structure where the instability of the flow occurs. Introduction of one flow into the other leads to the formation of the droplet. The surface tension acting across the interface allows the interface to resist the viscous force, and the size of the droplet depends on the ratio of the viscous force and surface tension. Thus, Capillary number ( $Ca$ ), defined as

$$Ca = \frac{U\mu}{\gamma} \quad (\text{Equation 1.5})[31]$$

, where  $U$  is the total linear flow velocity,  $\gamma$  is the surface tension at the interface and  $\mu$  is the viscosity of the fluid, governs the droplet generation. Additionally, the fraction of the flow rate of the water phase to the oil phase controls the size of the droplet. When the aqueous phase flows slower, the shear force on the aqueous phase becomes higher. Therefore, the diameter of the droplet increases when the water fraction increases.

#### 1.1.5 Femtolitre droplets

Microdroplets production in microfluidics offers promising opportunities in biological, chemical and pharmaceutical research. Comparing to batch emulsion production, the size of the droplet can be precisely controllable and reproducible. Monodisperse microdroplet enables quantitative studies.

Microfluidic droplet emulsion is produced by shearing one liquid into the other immiscible liquid. The competing stresses drive the interface when two immiscible liquids meet each other: surface tension between the liquids acts to reduce the interfacial area, and viscous stresses extend and drag the interface downstream. These stresses destabilise the interface and form droplets. Several techniques of droplet production have been introduced, such as co-axial injection device [43, 44], T-shaped device [45, 46], and flow focusing device [47], referring a few.

## 1.2 *Caenorhabditis elegans*

*C. elegans* is a sub-millimetre to a millimetre sized roundworm constituting the phylum *Nematoda* and found on the soil. The nematode *C. elegans* is a brilliant model organism for studying neural dynamics because of its compact

and well characterised nervous system.[48-50] Since proposed and settled a model organism by Sydney Brenner in 1965, it has been widely studied in the fields of developmental biology, molecular biology, neuroscience, genetics.[51-57] ?

This worm has potential for genetic analysis and molecular biology.

First, it has a rapid life cycle. An egg grows up to the egg-laying adult in 3.5 days at 20°C or 3 days at 25°C. Also, a single adult produces 300-350 progeny. It means it takes less than ten days to get approximately a million progenies from a single parent by three generations of production.

They exist mainly as hermaphrodites, each organism producing eggs and sperms to self-fertilise, combined with the ability to cross hermaphrodites with a male. This self-fertilising provides some advantages for genetic study. First, self-fertilisation reduces the efforts in maintaining stocks because a single worm can rise to an entire population just by culturing. Moreover, self-fertilisation follows the standard Mendelian rules so that heterozygous parents will produce the standard 1:2:1 pattern of segregation in their genotype (25% of dominant homozygotes, 50% of heterozygotes and 25% of recessive homozygotes).

Also, the body of the *C. elegans* is transparent and individual cells, and organs are easily imaged on compound microscopes. Transparency enables studies using fluorescent protein tags. Fluorescent protein enables genetic screening to identify mutants in various cellular processes. Furthermore, fluorescent protein-based reporter (such as calcium indicator GCaMP or Cameleon) which fluoresce in response to calcium concentration in the cell, provides the information of calcium flux in neurons and allows measurement of the neuro-response *in vivo*. [58]

Additionally, they have an invariable number of somatic cells which can trace the lineage during differentiation from the newly fertilised cell to adult cells.

The simplicity of the body structure is one of the advantages as well. One organism has 959 somatic cells. Among them, 302 cells are neurons. *C. elegans* shows both primitive (feeding, locomotion and reproduction) and complex (learning, mating and social) behaviour.

## **1.2.1 The nervous system of *C. elegans***

### **1.2.1.1 Neurocircuit of *C. elegans***

*C. elegans* has been widely used as a model animal especially for research on neuroscience. This worm has 302 neurons, of which the connection is

highly stereotyped. It allows definition of all synaptic connections among neurons and establishes a functional mapping of the neurocircuit.[48] Of these, 282 neurons belong to the somatic nerve system and the remaining 20 cells to a pharyngeal nerve system.[48, 53, 59, 60]

Connectomics, the study of comprehensive maps of neuronal connections, has been extensively researched. The comprehensive map of the neural connections (connectome) has been revealed and reconstructed by serial electron microscopy images. A nearly completed connectome of *C. elegans* has been established. [48, 61] Recently this connectome study has been improved through computational analysis.[62]

The established map of the neural wiring is a pivotal tool for correlating the neuronal activity and the worm's behaviour. If a neuron is identified as involved in a specific response or behaviour, the connectivity diagram provides critical implication to infer other neuron involved in the process. Two or more neurons are connected through chemical synapses or physical gap junctions. And the motor neurons are connected to the musculature through the neuromuscular junction. Approximately 6,400 synapses, 900 connections with gap junctions, and 1,500 neuromuscular junctions have been identified.

However, the connectivity alone is insufficient to understand and predict the behaviour of the organism because it lacks how the connection relates to the behaviour, i.e. the synaptic connection could be either excitatory or inhibitory, and any connection could show stochastic activation. To understand how the comprehensive nervous system encodes information of the environment into their behaviour, the experimental data of neurophysiological and behavioural studies need to be integrated with connectivity data.[63, 64]

The ensemble of the neuro-muscular activity forms behaviours. The worm demonstrates not only basic behaviours including locomotion, feeding and defecation but also complex behaviours such as mating, sex-specific behaviours and convoluted movement, namely omega turns or pirouettes. *C. elegans* also exhibits sensory-related behaviours such as nociception, chemosensation, olfaction and mechanosensation. [54, 65-70]

The neural circuits responsible for the sensory responses are composed of three levels of organisation[70]. The first level is sensory neurons which transduce external stimuli into a depolarisation state of the neurons. Total 16 pairs of bilaterally symmetric neurons are known as chemosensory neurons which respond to volatile or soluble stimuli. The information is transmitted to the next level of neurons called interneurons. Interneurons deliver the signal from the



### 1.2.1.3 Synapse

The transmission of information from neurons to other neurons occurs through a synapse or gap junctions.

A synapse is a knoblike structure that each terminal of the neuron swells for transmitting the information from one neuron to the other. Synaptic transmission occurs across the cleft between pre-synaptic neurons to the post-synaptic cells (either neuron or muscle). Chemical features deliver the electric impulses; neurotransmitters synthesised in the pre-synaptic neuron release into the cleft and are bound to post-synaptic receptors. This process occurs through steps including neurotransmitter synthesis, loading the neurotransmitters into vesicles, vesicle transport to the axon terminal, the fusion of the vesicle to the membrane, the release of the neurotransmitter into the cleft, diffusion of the neurotransmitter across the cleft, and binding of the neurotransmitters to post-synaptic receptors. Then, the conformational change of the receptor initiate reactions which open the  $\text{Ca}^{2+}$  voltage channels, and the flux of the ions rapidly shifts electric charge across the post-synaptic membrane. Consequently, this produces the change in postsynaptic potential.[71]

Several neurotransmitters in *C. elegans* have been discovered. Acetylcholine, Dopamine, Octopamine, Serotonin, Tyramine, Glutamate, and Gamma-aminobutyric acid (GABA) are common neurotransmitters of them.[72]

It was known that the neurons in *C. elegans* has no action potential and are graded rather than spiking.[73, 74] The synaptic release is also graded as roughly proportional to the membrane potential: when the membrane is depolarised, more neurotransmitter is released. Conversely, in hyperpolarised condition, the release of neurotransmitter is decreased or stopped. However, recently, it was reported that some neurons in the nematode demonstrated to be capable of exhibiting action potentials, and voltage-gated calcium and potassium channel do roles in action potential dynamics. [75]

### 1.2.1.4 Gap junctions

Another method of the transmission between two neurons is through gap junctions.[48, 76-78] Gap junctions are intercellular channels connecting the cytoplasm between adjacent cells. These gap junctions are expressed in all cells of the organism (alimentary system, reproductive system, excretory system, epithelium, nervous system, mesoderm).[77, 79-81] And they are responsible for determining the fate of the cell in embryogenesis by cell-to-cell communication.[79] They allow direct passage of ions or small molecules

between two cells, enabling metabolites or signalling molecules to be delivered from one cell to the other. Therefore, these junctions function as a mechanism of rapid signal transmission between the connected cells. Influx or efflux of ions alters the membrane potential of neurons and these ions can diffuse from the cytoplasm of one neuron to the other through gap junctions thus altering the membrane potential of the adjacent neuron.

Gap junctions are composed of a protein family called connexins in vertebrates or innexins in invertebrates.[82] Connexin and innexin families have a similar function, but there is no sequence homology.[82] In *C. elegans*, 22 different innexin genes have been discovered. Six subunits of connexin or innexin form the hemichannel of the gap junctions at the cell membrane in one of the partners, homotypic (six subunits are identical), heterotypic (two different homotypic hemichannels form a channel), or heteromeric (a mixture of subunit composition).

**1.2.1.5 Head sensory neuron of *C. elegans***

The *C. elegans* senses hundreds of chemicals that reflect bacterial food source or noxious environment.[69, 83] Two of the head sensory organs, called amphids, function as the main olfactory and chemosensory organs, and are positioned anteriorly on the left and right sides. Amphids contain 12 left-right pairs of sensory neurons with long cilia that extend to the tip of the body and are exposed to the outside and with cell bodies in the nerve ring, where they synapse onto other neurons in the sensory integration and decision making circuits.[77, 84] **Table 1.1** shows the neuron pairs and their functions.

**Table 1.1** Head sensory neurons. Adapted from wormatlas.[49]

Neuron	Function	
ASH	polymodal	Nociception: Osmotic avoidance, Nose touch avoidance, Chemical avoidance, Social feeding
ADF	soluble chemosensory	Dauer formation, Chemotaxis (minor)
ADL		Avoidance (minor), Social feeding
ASE		Water-soluble chemotaxis
ASG		Dauer formation (minor), Lifespan, Chemotaxis (minor)
ASI		Dauer formation, Chemotaxis(minor), Navigation

ASJ		Dauer formation and recovery, Chemotaxis (minor), Lifespan
ASK		Avoidance (minor), Chemotaxis (minor), Lifespan, Navigation
AWA	volatile chemosensory	Volatile chemotaxis, Lifespan (minor)
AWB		Volatile avoidance
AWC		Volatile chemotaxis, Lifespan, Navigation
AFD	Thermosensory	Thermosensory

11 out of 12 head sensory neurons are for the detection of molecules and all but two pairs of neurons, ASE and AWC, are functionally symmetric.[85, 86] [87] ASE left neuron respond to the increase of sodium ions and right neuron to the decrease of chloride ions. [86]. Despite their different sensory functions, both ASE neurons mediate salt attractive behaviours.

On the other hand, AWC is responsible for sensing volatile molecules such as benzaldehyde, butanone, isoamyl alcohol, 2,3 pentanedione and 2,4,5 trimethylthiazole.[49]

These neurons exhibit a different feature of asymmetry. ASE neurons show directional asymmetry, which means left and right cells express the same different invariably. The initial symmetry breaking occurs at the stage of the embryogenesis, at the 6-cell stage. [88, 89] In contrast, the ASE neurons display stochastic asymmetry, which means both subtypes ( $AWC_{on}$  and  $AWC_{off}$ ) are differentiated with equal chances to be located on the left or right side. It was revealed that cell to cell communication between the AWCL and AWCR in late embryogenesis directs the asymmetry.[84, 90]

### 1.2.2 Chemotaxis

Chemotaxis is defined as a strategy of the organism for moving toward the chemical source.[91] This is one of the critical behaviours of the worm to navigate toward where the vital source is abundant, so that increases the chance to survive. A conventional chemotaxis test has been carried out by placing the worm in an area and observation the movement induced in response to chemical substances.[69, 83, 91-98]

### 1.2.3 ASH neurons

ASH is a representative nociceptive neuron located in the head (**figure 1.3**), which senses noxious stimuli, such as mechanical nose touch,

hyperosmolarity, heavy metals ( $\text{Cd}^{2+}$ , and  $\text{Cu}^{2+}$ ), detergents, volatile repellent chemicals (1-octanol), an alkaloid (quinine) and light [99-103]. This neuron leads to rapid avoidance movement from the stimuli.[91, 94, 101, 102, 104] The role of ASH to respond to various stimuli, including both mechanical and chemical cues define it as a polymodal nociceptor, which is an analogue of pain-sensing polymodal nociceptive neurons in the vertebrate.[105] The response of ASH neuron to the stimuli have been studied *in vivo* with a genetically-encoded calcium indicator.[56, 106]

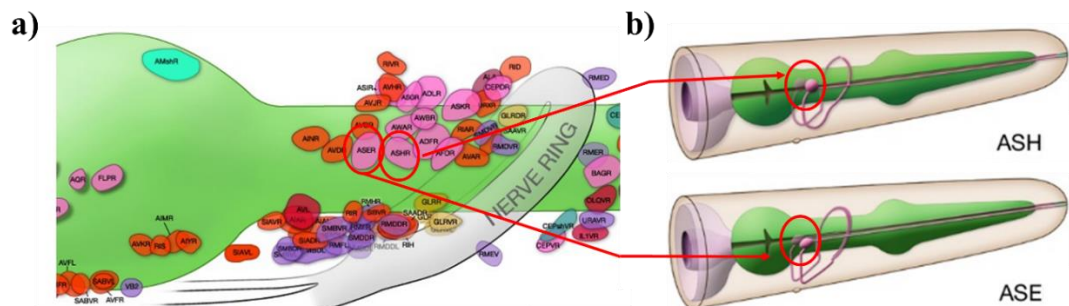


**Figure 1.3** a) The scheme of the neurons in the head of *C. elegans* (lateral view) (b) 3D scheme of ASE and ASH neuron. The pair of neurons are located in the left and right side of the head. Reconstructed from Wormatlas.[49]

ASH neuron is responsible for light sensing. Ward *et al.* carried out an ablation study and found that ASJ, AWB, ASK and ASH neurons together have a role in sensing the light and initiating the reverse locomotion, while ablation of an individual neuron does not yield a significant functional deficit.[107]

It is known that the downstream signalling in ASH is stimulus-specific: Hart *et al.* and Maricq *et al.* showed that a mutation in the glutamate receptor subunit, *glr-1* gene removes the response to nose touch but not to osmotic stimuli.[54, 108]. Similarly, Walker *et al.* revealed that  $\text{IP}_3\text{R}$ , the inositol 1,4,5-trisphosphate receptor encoded by *itr-1* takes a role in the responses to benzaldehyde and nose touch but not to other known ASH-mediated behaviours.[109]

Chatzigeorgiou *et al.* discovered that transmembrane like channel gene *tmc-1* encodes a sodium sensor in ASH neuron. The expression of *tmc-1* in ASH neuron is required for NaCl-evoked neuronal activity and avoidance to high concentrations of NaCl.[110]

The worm immediately reverses and turns its body to change the direction of movement in response to a variety of chemical and other repulsive cues.[104] ASH neurons are connected as synapses with AVA, AVB, and AVD, which are interneurons inducing forward and backward movement. [48, 49]

ASH mediates social feeding behaviour with ADL in response to repulsive stimuli such as high O<sub>2</sub> concentrations. Ablation of ASH and ADL eliminates the social feeding behaviours and alters the animal into solitary feeders.[111] This response is known to be modified by memory or environment. Acute alteration of the partial pressure of oxygen affects locomotory speed, turning, and reversal.[112]

#### **1.2.4 ASE neurons**

ASE left and right are a pair of functionally asymmetric neurons among the head sensory neurons (location is shown in **figure 1.3**). ASE senses Na<sup>+</sup>, Cl<sup>-</sup>, cAMP, biotin and lysine.[105] ASEL responding to the upshift and ASER downshift of the salt concentration.[86] ASE left and right were individually tested and found that ASEL primarily senses Na<sup>+</sup>, whereas ASER does Cl<sup>-</sup> and K<sup>+</sup>. [83, 105, 113] There is no known direct anatomical connection between ASEL and ASER.

Several sensory neurons are responsible for sensing sodium chloride, and among them, ASE neurons were proven to do a pivotal role in chemotaxis by ablation studies.[83] Worms simultaneously ablated for all amphid and phasmid neurons except ASE kept the behaviour of chemotaxis. Additionally, the damage in ASE neurons weakens the responses in ADF, ASG, ASI, ASK and ASJ.[105]

For the avoidance by detecting repellents, it is known that ASH, ADL, ASK and ASE neurons are responsible for the stimuli sensation. Among them, ASH neurons do a major role in avoiding behaviours. The rest of them play minor roles; they are apparent only when ASH neurons are not functioning.[99-101]

ASE is one of the primary CO<sub>2</sub> sensors with AFD and BAG. As opposed to the asymmetric response to NaCl, both ASEL and ASER respond to the increase of CO<sub>2</sub>. [114]

In the sense of behaviour, when the worm senses the increase in sodium chloride, the possibility of forwarding locomotion is increased. The decrease in sodium chloride gave the opposite effect. These result the worm move toward the NaCl, the attractant by a biased random walk.[115] On the other hand, ASE induces food-leaving behaviour. In the well-fed *C. elegans*, when food becomes limited or depleted, the attraction to salt alters to repulsion. DAF-2 insulin receptor in ASER and INS-1 dependent feedback from AIA to ASER are involved in the alteration of the preference.[116, 117]

### **1.2.5 Cell visualisation and measurement of neuroactivity of *C. elegans***

The character that the body of the worm is transparent allows for direct observation of the internal structures. Taking advantage of the easy visualisation, cellular patterning of the tissue and organ, tracking the cell lineages in embryogenesis and cell division have been widely studied.

Development of green fluorescent protein (GFP) and molecular biology to express the protein in the cell boosts the research of *C. elegans*. GFP is a helical barrel structure protein consisting of 238 amino acids. Osamu Shimomura purified the protein from *Aequorea victoria*, the jellyfish.[118, 119] Since then, efforts to improve the photostability or modifying the fluorescence wavelength has been carried out.[120-127] Currently, the fluorescent protein palette covers all wavelength of the visible spectrum and extending into the infrared.

The neuron study has taken advantage of the genetically encoded fluorescent calcium indicator as it enables us to observe the calcium ion-dependent neuroactivities of an alive organism. GCaMP is a fusion protein of GFP, calmodulin and M13 peptide sequence, and used as a calcium indicator which is genetically encoded and expressed in the cell.[128] This indicator enables to image and analyse the dynamics of calcium ions in living organisms. The circularly permuted structure represses the fluorescence of the GFP motif of GCaMP. When calcium ion exists, the calmodulin motif, with high affinity to the  $Ca^{2+}$  ion, binds the ion and undergoes a conformational change to recovers the fluorescence of the GFP motif. Since the first GCaMP has been introduced, many improved versions of the indicator called GCaMP2 through GCaMP 8 have been reported.[129-131]

### **1.2.6 Imaging system for tracking the activity of neurons**

Imaging of neuronal activity from unrestrained microscopic animals requires tracking as they are freely moving. The tracking in early recordings was done manually, adjusting a microscope stage to keep the worm centred.[132] Then, automated tracking systems were developed to track the worm by adjusting a motorised x-y stage. [133, 134] It is required to use a high magnification objective lens to resolve neurons in the organism. However, the field of view of such lens is small relative to the travel speed of the organisms, as worms and the larvae of a fly are known to crawl at speed up to 500  $\mu\text{m}$  /second and 2,000  $\mu\text{m}$  /second, respectively. [97, 135] They set up multiple objective lenses to obtain wide of field enough to observe the behaviour in motion using

a lower magnification lens and resolution enough to distinguish neurons using a higher magnification lens. (example of the system in **figure 1.4**) Similar systems were used for larvae of zebrafish. [136, 137] and *Drosophila* larvae.[138]

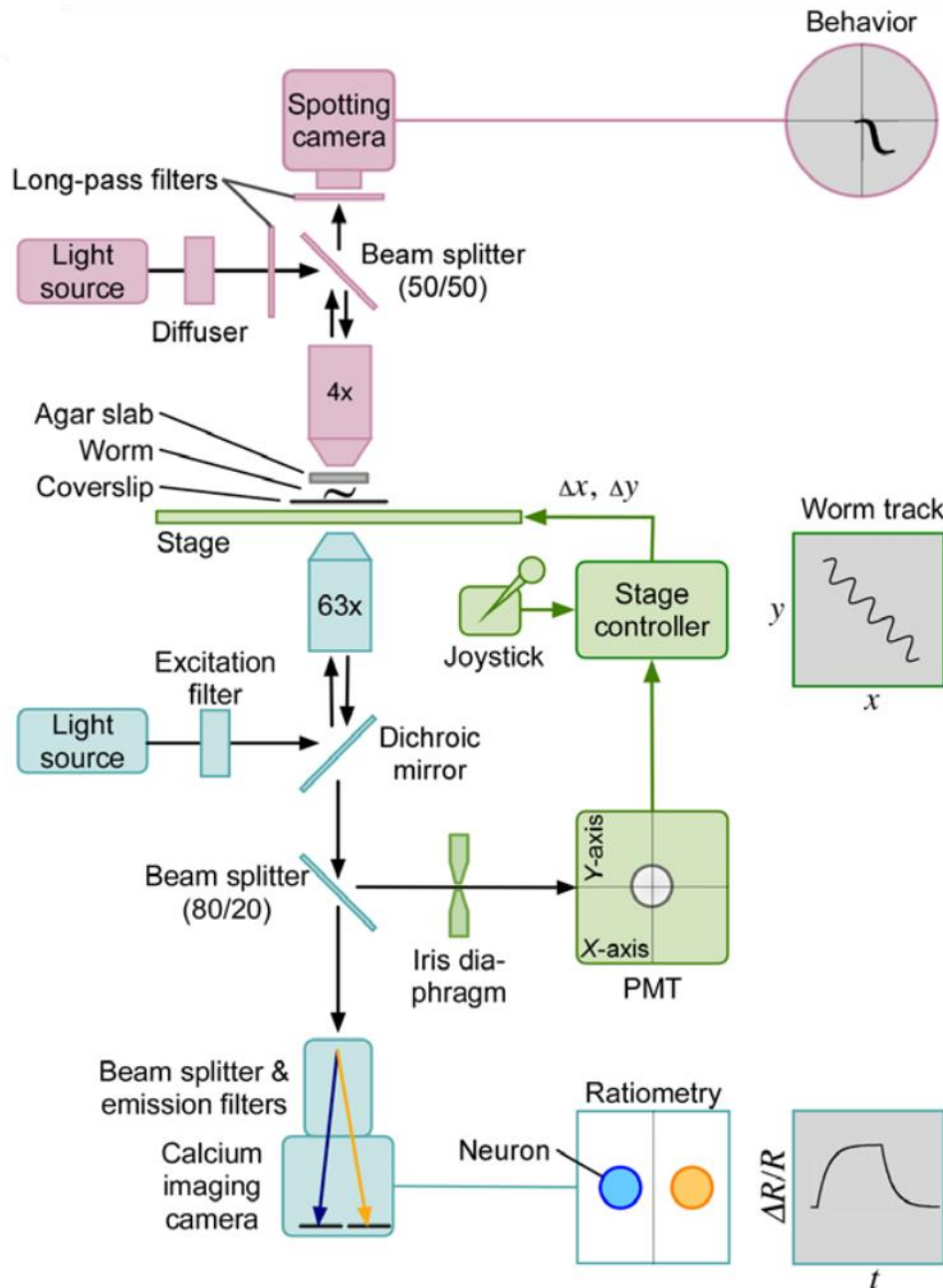


**Figure 1.4** Scheme of the Image-free, optomechanical system (adapted from Faumont *et al.* [134])

### 1.2.7 Fast 3d imaging of neural activity

Recordings from large numbers of neurons are required to understand how the ensembles of neurons encode the information of the environment taken by sensory neurons into behaviours. Fast 3D recordings of neural activity in an either fixed or free animal have been reported.

Light-field microscopy supports single-shot volumetric recording (**figure 1.5**). Microlens arrays in the instrument enable multiplexing of 2D-spatial and 2D directional information on the same image sensor. Taking advantage of the capability of instant 3d imaging by fast readouts, LFM has been used in observing neural activity in animals, such as *C. elegans* [139], *Drosophila* [140] and Zebrafish [141]. In most studies, the organisms for imaging were immobilised or anaesthetised to avoid the needs for tracking. However, recently, LFM imaging and tracking of neuronal activity of freely-moving zebrafish larvae has been reported. [142]

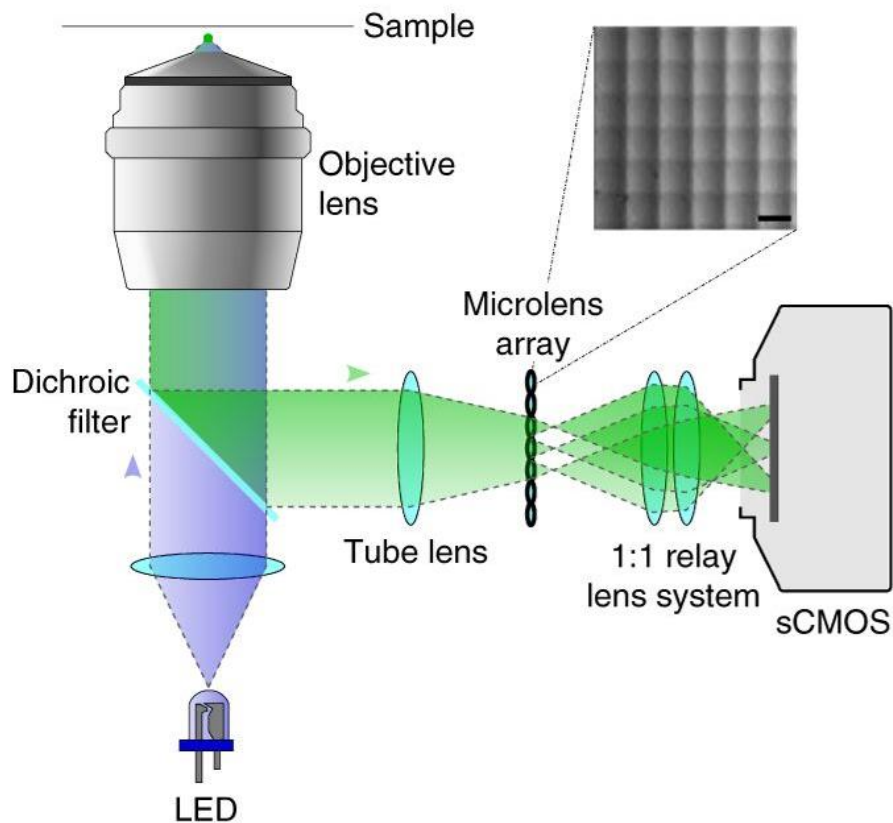


**Figure 1.5 Scheme of light-field microscopy. The Image was adapted from Prevedel *et al.* [139]**

Confocal microscopy is one of the conventional systems for 3D imaging (**figure 1.6**). [143] Either scanning or spinning disk confocal microscope system deliver broad illumination and collect the emitting photon from planes of interest. Nguyen *et al.* and Venkatachalam *et al.* have been shown brain-

wide imaging in moving *C. elegans* using a customised spinning disk confocal microscopy system in which tracking systems are integrated. [144, 145]

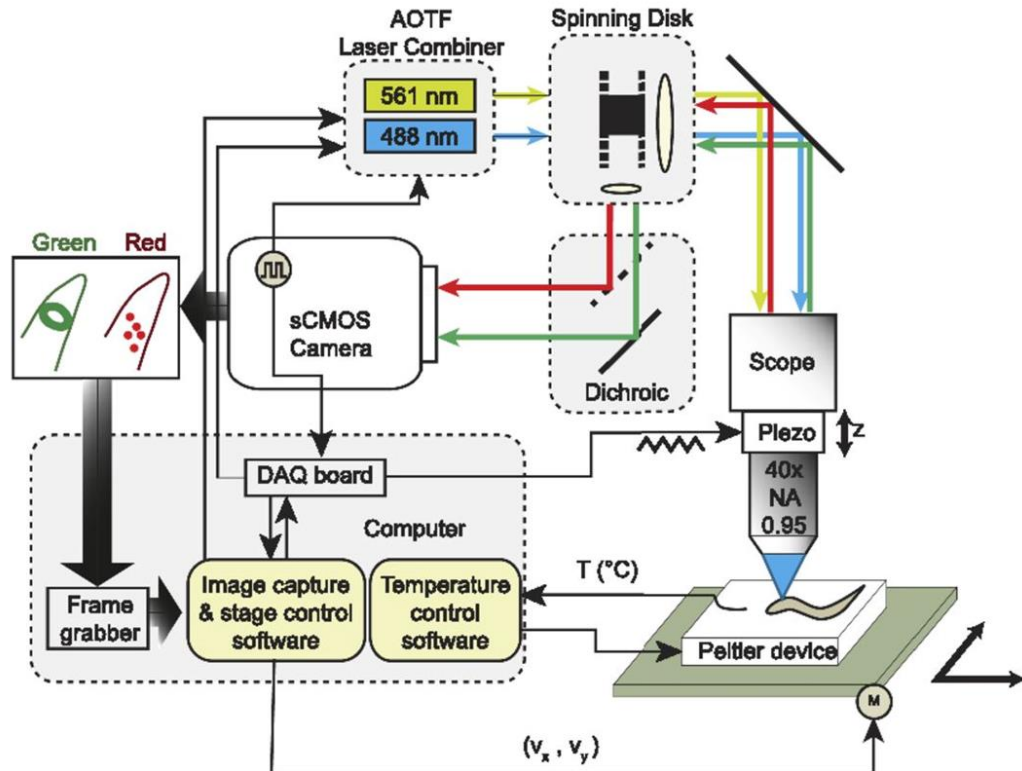


**Figure 1.6** Example of confocal microscopy setup for imaging multiple neurons in the brain of *C. elegans* (Adapted from Venkatachalam *et al.* 2016 )

### 1.2.8 Microfluidic device for the study of *C. elegans*

Microfluidic devices have been used for *C. elegans* study. Microfluidic technology offers an excellent set of tools for the manipulation of small animals and the measurement of their spontaneous and evoked responses under tightly controlled conditions.[20, 56, 146-155] .

PDMS is transparent, non-toxic to worm and gas permeable and is commonly used for worm devices, and it was proven that even long incubation is available.[149, 156] The versatility of the integration of various subunits such as valves, pumps etc, and even availability of automation means that *C. elegans* microfluidic system is widely used in a broad range of study, from routine procedure, such as sorting[157-159] and microinjection[160, 161] to specific, such as behavioural study [56, 151, 152, 162-164] and cellular/molecular investigation.[165, 166]

#### 1.2.8.1 Worm immobilisation.

The immobilisation of the worm is beneficial in the aspect of handling and observing the live process of the organism as it can avoid the need for

tracking. The conventional methods to immobilise the worm are using anaesthetic agent or glue.[167] However, these methods are less than satisfactory because of the potential toxicity and alteration of metabolism. Also, the use of glue makes multiple time monitoring unavailable. Alternatively, other approaches to immobilise the worm, such as CO<sub>2</sub> treatment[146], instant cooling[168], and thermosensitive hydrogel[149] have been introduced.

**Figure 1.7** shows a few examples of the microfluidic device for immobilisation of the worm. One approach for immobilisation is to build a narrow space and to push the worm into the place gently such that the movement of the worm would be majorly restrained. The first design as the trap is a straight and tapered channel. Hulme *et al.* used an array of 128 parallel tapered traps to immobilise multiple worms (**figure 1.7a**). [147] The worms were injected into the chamber of the device and moved to the traps by flow, and eventually, a single worm entered one of the traps and was immobilised. Then the worm stopped the flow passing through the occupied channel, and this was followed by another worm occupying one of the available traps. This strategy enables to trap only a single worm in each trap. They showed that the array is available to trap more than 100 worms in less than 15 minutes, and compatibility that the worms were not damaged in the trap.

Then, especially for study where the confinement of the head is critical, a trap was carefully designed to the shape of the head. Chronis *et al.* studied the response of the head sensory neurons using this device (**figure 1.7b**).[56] An integrated module for redirecting the flow enables on and off the stimulus to the amphid of the immobilised organism. They successfully imaged calcium activity of ASH neuron with this device.

Alternatively, the immobilisation of the worm was achieved by compression by an additional valve module. Chokshi *et al.* immobilised the nematode by using pressure-controlled PDMS film consisting of the wall of the channel (**figure 1.7c**).[146] A multi-layered microfluidic channel is built, and the thin wall between two channels was stretched to the worm and physically limited the space of the movement of the worm, applying the pressure into the channel. Additionally, they applied pressurised carbon dioxide gas to control the film. Air-permeable PDMS film allowed CO<sub>2</sub> gas to reach the worm and paralysed it.

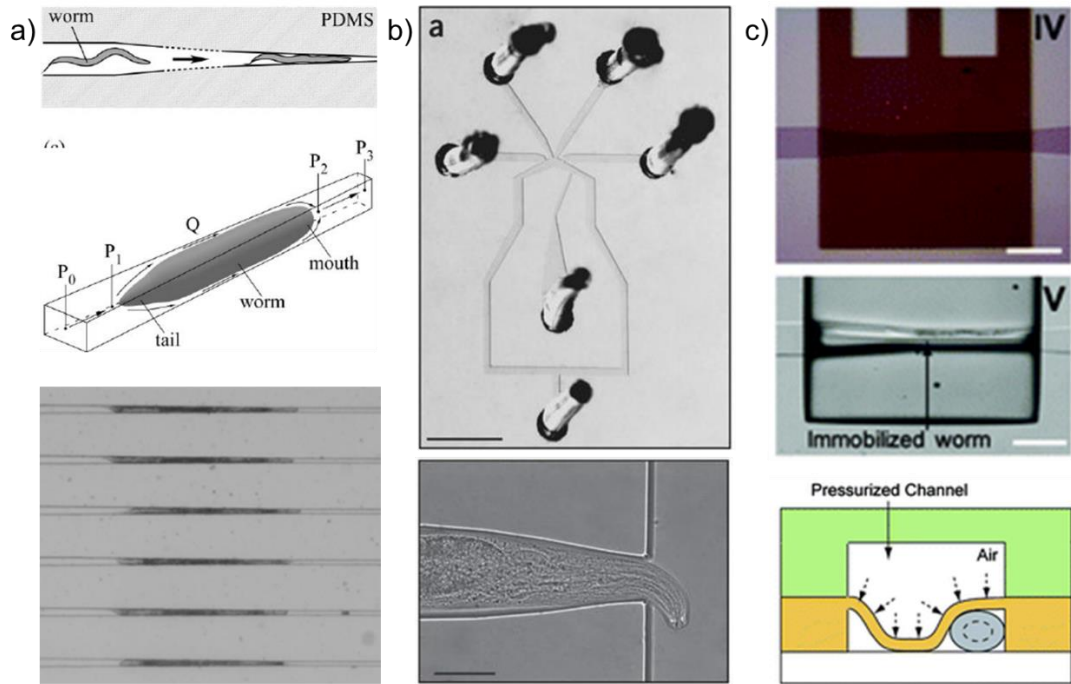


**Figure 1.7** Previous study of *C. elegans* immobilisation. a) Tapered channels b) olfactory channel c) CO<sub>2</sub> pressurising channel. Reconstructed from [56, 146, 147].

### 1.2.8.2 Worm immobilisation with controlled orientation

A free worm lies on its side and crawls by propagating a dorsal-ventral bend along a dorsal-ventral axis, using body muscles placed along its dorsal and ventral side.[169] However, the location of the organs in *C. elegans* is strongly stereotyped. The dorsal nerve cord runs along the length of the worm on its dorsal side. The distal arms of the gonad is located in the dorsal side, and it is required for a capillary to approach in lateral orientation to perform microinjection.[170] The orientation that vulva facing the imaging system is needed for the study of egg-laying behaviour. [171] On the other hand, in multiple neuron studying, a specific orientation that all the target neurons are in the focal plane is required.

With the exception of whole-brain imaging studies,[145, 172, 173] imaging one or more pairs of bilateral neurons simultaneously has largely been avoided since, in most experiments, the animal lies on its left or right side, such that the two sides are not located in the same focal plane of the microscope (**figure 1.8**). While neuronal and, to a lesser extent, subcircuit functions have been extensively studied,[86, 174, 175] these have almost exclusively been limited to either the left or right side of the body, limiting our understanding of symmetry and asymmetry in sensory responses and information flow.

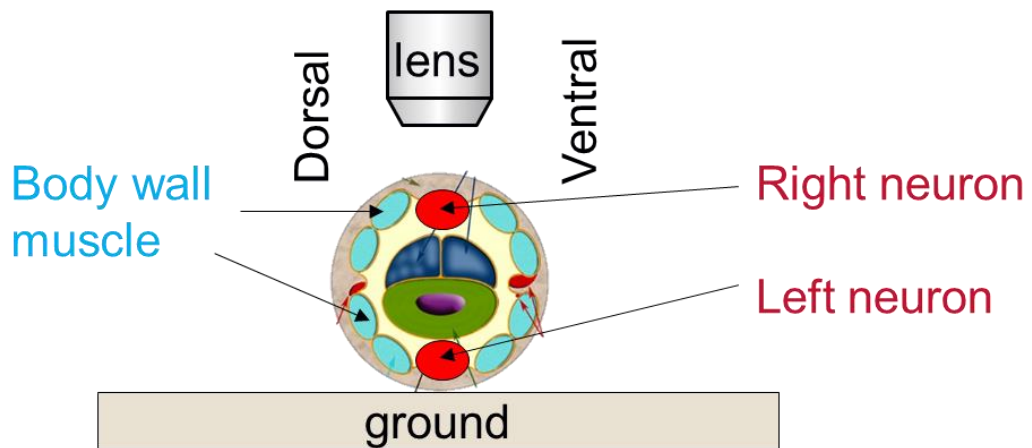


**Figure 1.8** Orientation of the body of *C. elegans*. The worm crawls laying on side, and pair of bilateral sensory neurons are located out of focal plane, which limits usage of typical epi-fluorescence microscope.

Two conventional methods have achieved the immobilisation of the worm with specific orientation, i) managing a single worm into a v-groove agar using a worm pick or ii) placing a glass slide on a population of the worms spread on flat agar plate to hold their random orientation.[176] The first method requires expertise to handle the worm; orienting the worm without damage and is time-consuming. The second methods require many worms to obtain a wanted orientation. Despite culturing a large population of the worm is relatively easy in the second method, the worm under the glass slide is nearly inaccessible for following procedures such as stimulus exposure or injection.[176]

A handful of microfluidic devices with a capability to rotate *C. elegans* and to simultaneously observe a pair of neurons have been reported.

Ardehshiri *et al.* used a glass capillary to grab and rotate a worm within a microchannel pneumatically (**figure1.9a**).[176] The device was composed of PDMS and a glass capillary where a single worm is immobilised and which is oriented on-demand at the desired lateral direction. The longitudinal orientation (coming with the head first) was achieved by using the nature of electrotaxis. Then, the worm was trapped by pneumatic capturing and manually rotated laterally using the integrated glass capillary. This freely rotating capillary device could be very powerful for multi-angle imaging. However, the device is the lack of a flow control module. So, additional development of integrating flow control module is required to study the response of sensory neurons.

Ahmed *et al.* reported acoustic field-driven microvortices (**figure1.9b**).[177] They described a method of so-called acoustofluidic rotational manipulation. An array of air microbubbles were trapped in a microfluidics device and

oscillated to generate microstreaming vortices. This method was applied for the rotation of *C. elegans* to image the structure of the ALA interneuron, of which two dendrites spread through the length of the body, and the morphology of the reproductive system. This approach is plausible. However, using physical force to rotate the organism could affect the response as the worm senses mechanical touch.[103]

Recently, Reilly *et al.* fabricated a microfluidic channel with curvature to rotate the worm before it reaches the trap (**figure1.9c**).[178] Using this modified 'olfactory chip' from Chronis *et al.*, they imaged male-specific cells. This device was also used to image a pair of ASH neuron simultaneously. However, while imaging bilateral neuron pairs, the worms were physically twisted in these devices during imaging.

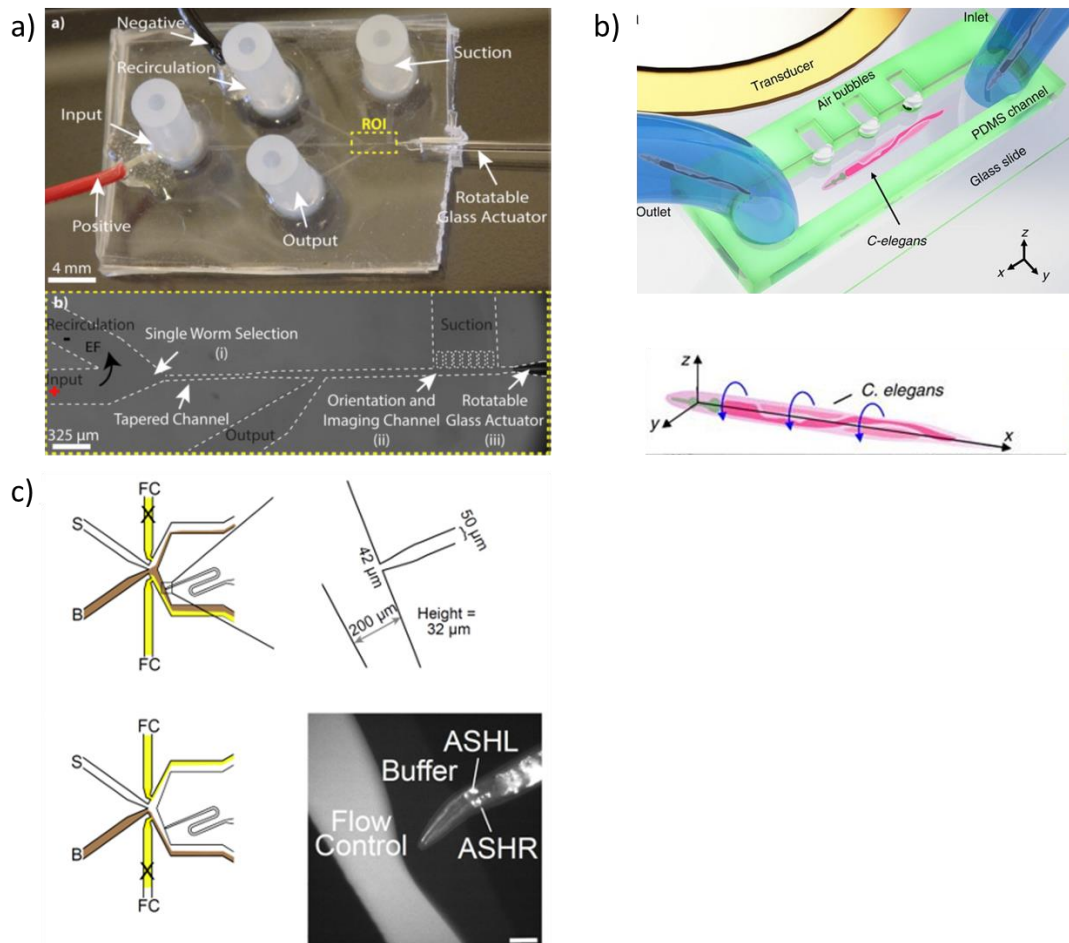


**Figure 1.9** Example of microfluidic system for multiangle imaging of *C. elegans*. a) Rotatable glass actuator; b) acoustofluidic rotational manipulation using acoustic field driven microvortices; c) channel with curvature. Adapted from Ardeshiri *et al.*[176], Ahmed *et al.*[177] and Reilly *et al.*[178]

Recently, Hochstetter *et al.* introduced a pre-segmentation procedure to build smooth-sided PDMS devices for multi-angle imaging (**figure 1.10**).[179] Simply curing the polymer with hydrophobized glass slides on each side, they created PDMS microfluidic device which has transparent walls. They studied compatibility of this technique for approaching with conventional light, confocal and 2-photon light-sheet microscopy for two-dimensional and three-dimensional reconstructions. They mentioned the economic advantage and the potential of using in the biological study, however, this system has not been applied for an animal study yet.

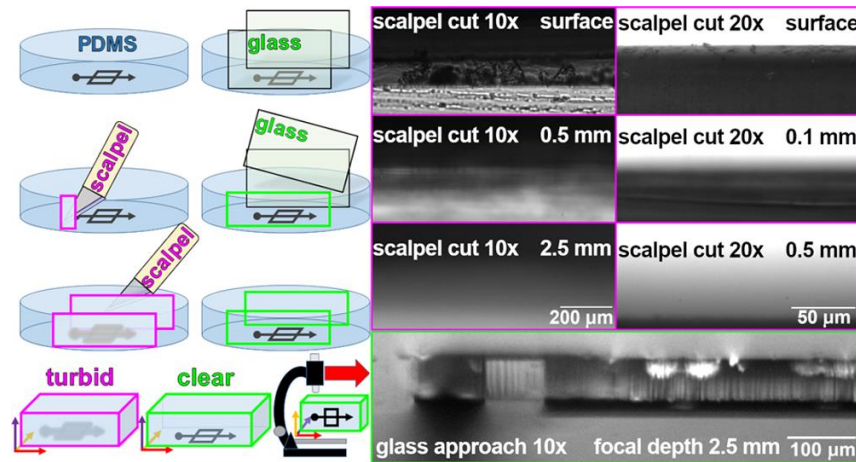


**Figure 1.10** smooth-sided PDMS devices for multi-angle imaging. Adapted from Hochstetter *et al.* [179].

### 1.2.8.3 The behaviour of the worm in microfluidic devices

The worm responds to environmental stimuli. Then, it interprets the information into behaviour. Behavioural assays provide essential information of the state of neuronal signalling because the behavioural responses are dependent on the functioning of the nervous system. Chemotaxis, thermotaxis, electrotaxis, and phototaxis are examples that are commonly studied.

Conventional behavioural assays in *C. elegans* are carried out on agar-plates with controlled stimuli in or on the agar. Multiple worms are placed on the plate, and the behaviour of the worm was studied and analysed. However, the observation of the neuron in an individual animal is not easy in such an assay.

Hu *et al.* introduced a microfluidic device that can form a linear gradient of the NaCl around the worm using stepwise mixing channels to study the chemotaxis.[180] The test was carried out in the range of 0 – 300 mM sodium chloride for attraction or repulsion of the worm.

Bargmann and Chronis reported a device that can investigate the movement of the worm.[56] The behavioural chip is a straight channel with a tapered end. The channel is wide enough for the worm to generate sinusoidal waves when attempting to move, but not to escape. The chip enables us to reveal that AVA neurons have a role in locomotion.

Albrecht and Bargmann developed a device structured as a wide area with a hexagonally arranged post to study odour induced movement.[162] They classified the movement of the worm into five states: forward, pause, reverse, pirouette reverse (retrieve before an omega turn) and pirouette forward (employ after an omega turn).

McCormick *et al.* reported two microfluidic devices termed chemosensory and thermosensory devices.[164] The devices immobilised the posterior half while the anterior half was free to move side-to-side. The repulsive and attractive responses in forms of head movement are monitored with delivering of stimuli, using this device, the researchers found that both a rise and a fall in osmolarity induces the repulsive movement of the worm. They anticipated that it might be possible to image the neuronal response and movement of the head at the same time with some modification of the system.

#### **1.2.8.4 Other applications of microfluidics in *C. elegans* study**

The microfluidic technique is used for other applications in the laboratory of *C. elegans* such as sorting, culture and microinjection.

Sorting methods are employed by installing obstacles in the microfluidic device and letting the worms be discriminated by the size or movement of the body.[157-159, 181-183] Rezai *et al.* successfully separated a group of worm by the body size of the worm.[157, 158] By setting up consecutively decreasing size of the gates between chambers and applying the voltage encouraging the worms to move onto one direction. The gates discriminate the worm by allowing only the worms smaller than the dimension of the gate to pass through it. They achieved fast and easy separation.

Many studies of *C. elegans* require an extended period of culturing. It is not rare to observe and examine the nematode for the life-long time or several generations. Many microfluidic devices were developed for streamline cultivation and monitoring.[149, 156, 184-191]

Hulme *et al.* fabricated a device which has consecutive chambers connected with passages with a small dimension which only young worms can freely pass through, but the grown cannot.[156] The worm was cultured in the PDMS

device with the condition that food (*E. coli*) is supplied as suspended in the buffer.

Microinjection is one of a routine procedure for *C. elegans* study. It is an injection of DNA, protein and chemicals for biological process. Conventionally, microinjection is carried out by putting the worm with wanted orientation on thin dried agarose or agar. Then the worm was stabbed with glass capillary needle filled with the desired solution. However, this requires the labour-intensive process. A handful of microinjection methods using microfluidic technique have been introduced.[160, 161, 192]

### **1.3 Femtolitre droplet and single-molecule assay**

#### **1.3.1 Single-molecule analysis using femtolitre chamber**

Microfluidics provides a platform to control small amounts of fluid and enables single-molecule analysis by isolating a molecule into a small-volume compartment. One of the most substantial advantages of single-molecule analysis is to make it possible to study the heterogeneity of each molecule, which is usually veiled by average properties and noise when analysed collectively. The fundamental error occurs in the process of protein expression through mismatches between DNA and mRNA in transcription and wrong bindings of mRNA and tRNA in ribosomes in translation; the rates of accumulated error are between several per  $10^4$  base pairs and one per  $10^5$  base pairs.[193] This error rate means that each molecule of protein with a mass on the kilo-Dalton scale cannot avoid being heterogeneous. However, differences among protein molecules are hard to detect in ensemble study as the differences are usually not significant enough to overwhelm the noise. Rissin *et al.* observed that each enzyme has a different turnover rate by isolating single molecules of  $\beta$ -galactosidase into a bundle of optical fibres.[194]

Another advantage of single-molecule analysis is to provide a resolution that ensemble experiments are not able to achieve.[195] One strategy used for single-molecule analysis is compartmentalisation: separating and isolating the space of interest.

Compartmentalisation increases the local concentration by limiting the reaction volume. It achieves higher local concentrations and reaches the threshold of detection faster, consequently ensuring sensitive and rapid detection(**figure 1.9**)[195]. When single enzymes occupy the uniform and

known volume of the compartment, the concentration of a solution can be calculated by simple counting of the signal.

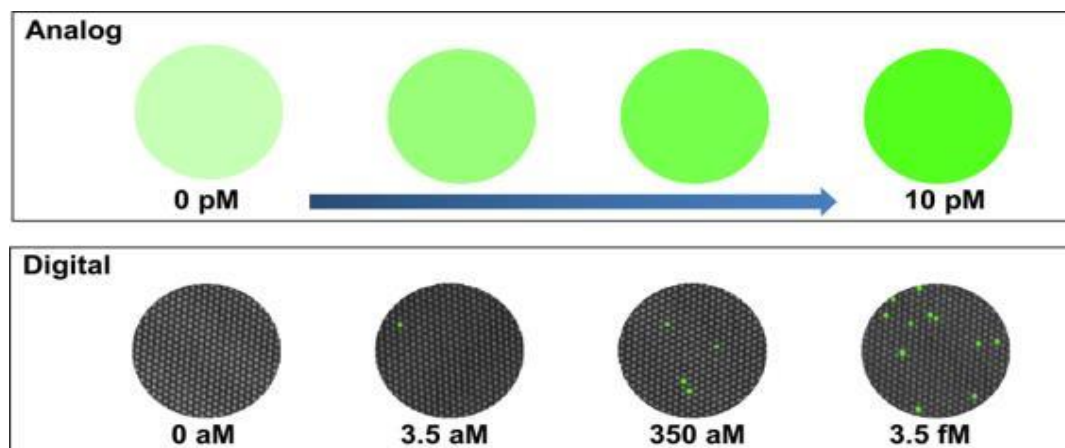


**Figure 1.11** Compartmentalisation for single-molecule analysis. Reconstructed from Walt *et al.* 2013.[195]

Several platforms for single-molecule analysis have been developed. For example, Rondelez *et al.* fabricated a PDMS device which presented an array of 14-100-fL-sized chambers and demonstrated a single-enzyme reaction of  $\beta$ -galactosidase and horseradish peroxidase by enclosing a liquid solution in the chambers.[15] Additionally, Rissin *et al.* developed femtolitre-sized reaction vessels using a bundle of optical fibres and quantised the concentration of streptavidin- $\beta$ -galactosidase at attomolar concentrations in 1 hour.[196] Sakakihara *et al.* developed hydrophilic-in-hydrophobic micro-patterned chambers using a hydrophobic carbon-fluorine polymer (CYTOP) and glass and isolated droplets of a hydrophilic solution in the chamber by covering it with hydrophobic oil. The kinetics of the single  $\beta$ -galactosidase molecule and the rotary motor protein  $F_1$ -ATPase in the droplet were thereby studied.[197] These studies show promise for application to immunoassays and could eventually improve the resolution of immunoassays to the single-molecule detection level.

### 1.3.2 Single-molecule immunoassays

A well-known technology, ELISA, introduced in the 1970s, can detect a biomarker present as low as picomolar concentrations.[198, 199] An immunoassay is a test to measure a molecule by using antibodies. Antibodies are proteins secreted from plasma cells to be employed in the humoral immune system. Antibodies are typically Y-shaped globular proteins which consist of two large heavy chains and two small, light chains, and have a size of ~150 kD. Their roles in organisms are to identify and neutralise antigens by binding to them. Naturally, antibodies are designed to bind to analytes with

high affinity and selectivity. This characteristic of antibodies makes them well-suited for use as sensing modules in assays.

Immunoassays employ labels for detection of the binding event between an antibody and an antigen. Since the 1960s, various labels have been introduced, such as enzymes, radioactive isotopes, fluorogenic reporters, and DNA reporters.[198, 200-202] Among them, enzyme labelling has been widely used as it amplifies the signal by converting the substrate and accumulating the product and the indicators. Enzyme-linked immunosorbent assay (ELISA), a standard immunoassay, is known to be able to detect biomarkers at the picomolar level.[15] However, this performance level remains unmet in clinical requests for detection of low-abundance biomarkers present in biological fluids at concentrations in the range  $10^{-12}$  -  $10^{-16}$  M.

The LOD of immunoassays has been decreased by adapting techniques of single-molecule analysis. Rissin *et al.* integrated optical fibre vessels to bead-based enzyme-linked immunosorbent assays (digital ELISA), and the LOD reached 0.4 fM when detecting a prostate-specific antigen (PSA) in serum.[203] Additionally, Kim *et al.* connected hydrophilic-in-hydrophobic micro-patterned chambers to digital ELISA, and the LOD of the system reached 2 aM.[204]

Among them, water-in-oil production by a microfluidic device has been emerging as a powerful tool for study requiring product accumulation, such as enzyme reaction related immunoassay [197, 205] because the size of the microfluidic droplets has been decreased to femtolitre scale and they can be produced at a frequency of a million hertz. In this size of the chamber, the fluorescent product conversion by a single enzyme molecule reaction could be detectable within minutes using a simple epifluorescence microscope. Droplet immunoassay has been applied to detect clinical biomarkers.[206-208]

### 1.3.3 Limit of detection

According to the guideline EP17 published by Clinical and Laboratory Standards Institute, LOD is defined as the lowest concentration of the analyte which is distinguishable from the limit of blank (LOB).[209, 210] LOB is defined as the highest analyte concentration expected to be found in the blank sample. LOB is determined by measuring blank samples and calculating as

$$\text{LOB} = \text{mean}_{\text{blank}} + 1.645(\text{SD}_{\text{blank}})$$

, where  $\text{mean}_{\text{blank}}$  is mean value of concentration of blank sample and  $\text{SD}_{\text{blank}}$  is standard deviation of concentration of blank sample.

LOD is estimated as

$$\text{LOD} = \text{LOB} + 1.645(\text{SD}_{\text{the lowest concentration sample}})$$

, where  $\text{SD}_{\text{the lowest concentration sample}}$  is standard deviation of the analyte of the lowest concentration sample.

### **1.3.4 Renal transplantation rejection**

Kidney transplantation is the last line of treatment for end-stage renal disease. Transplantation of an organ cannot avoid inducing many changes both in the host and in the graft. Among the changes, specific recognition of antigenic differences between donor and recipient prompts a caustic immune response and results in immune rejection. Since the first human renal transplants in 1906 by Jaboulay, recipient rejection has been addressed as a major challenge.[211]

Immuno-molecular mechanisms of graft rejection have been identified.[212] Immune rejection of graft is mediated by activation of T-cells of the host against donor cells. Host T-cells recognise the donor's major histocompatibility complex (MHC) class I encoded antigens. Infiltration of the transplanted organ by T-cells and other mononuclear leukocytes (such as B-cells and natural killer cells) activates the complement system and mononuclear cells, which are responsible for damaging the graft. Both CD4+ and CD8+ T-cells take part in acute cellular rejection. The production of anti-donor MHC class I and class II antibodies also participates in acute and chronic graft damage. In chronic graft rejection, the host's immune response activation is probably not the only cause of rejection; recurrence of the original disease, fibrosis, or viral infection could also play essential roles.

Rejection can occur anytime. Three types of organ rejection have been identified: hyperacute, acute, and chronic. Hyperacute rejection occurs within twenty-four hours of transplantation. Acute rejection happens within the first six months, whereas chronic rejection could appear between the first six months to several years after transplantation. Long-term treatment with immunosuppressive drugs helps to decrease morbidity and mortality of patients. However, these drugs cannot avoid limiting the quality of patients' lives and exposing the patients to side effects such as nephrotoxicity, cancer, and cardiovascular maladies.[213, 214].

At present, graft rejection is diagnosed by conventional clinical parameters and is confirmed by biopsy with histological examination.[215] Biopsies are one of the trusted methods for predicting organ failure. However, trained physicians are needed to perform this invasive examination. Moreover, they

usually detect rejection at a relatively late stage, after the graft has been already damaged.

Early detection of organ transplantation failure before tissue damage occurrence may help to establish a strategy of immunosuppressive drug treatment more efficiently and minimise their side effects, thereby improving the graft survival rate. Identification of biomarkers in sera, which indicate a high risk of subsequent acute or chronic graft rejection has been studied widely.[216, 217] Additionally, the technology for detecting biomarkers at low abundance in the sera of patients is required for successful early-stage detection of graft rejection.

## 1.4 Overview

This thesis aims to advance the currently available microfluidic technique for *C. elegans* neuroscience and detecting biomarkers indicating prostate cancer and renal graft failure using femtodroplet based single molecule counting immunoassay. The methodology used for the overall study was described in **Chapter 2**. Then, for the biological application, we focussed on the system neuroscience of the neuro-connection in *C. elegans*. Its stereotyped nervous system consists of 302 neurons and categorised in sensory, inter, and motor neurons. How the worm senses the environment and encodes the information into the movement are one of the major interests of researchers. The connectivity of the neurons in the longitudinal path has been widely studied; however, the investigation of bilateral connectivity was highly limited because of the nature of the worm laying on a side. The development of a rotatable microfluidic device enables us to image the left and the right head sensory neuron at the same time is described in **Chapter 3**. We selected two pairs of the amphid sensory neurons responding to sodium chloride; ASH, the nociceptive neurons and ASE, chemotaxis neurons, and imaged the neuronal activity of both neurons responding to the stimulus simultaneously to investigate the connectivity between the bilateral neurons.

Then, we aimed to develop a microfluidic device to find out the roles of ASE left and right in the movement of searching for favourable ions. An effort to develop a multi-layered rotatable device which enables simultaneous imaging of the head movement and response of the bilateral sensory neurons was described in **Chapter 4**. We aimed to treat a left-right gradient of the stimulus to the half-immobilised worm to investigate the dynamics of the head movement. So, we developed microfluidics modules to generate a vertical gradient of the stimulus concentration by transposing the horizontal gradient

using the 3-dimensional microfluidic device, and a worm trap enables to immobilisation of half of the body of the *C. elegans*.

Next, as the biochemical application, we aimed to validate the existing microfluidic platform for detecting a biomarker indicating prostate cancer developed by Shim *et al.*[205] and then port a new immunoassay onto it in **Chapter 5**. We generated 2.5-4 $\mu$ m diameter femtodroplets using a microfluidic platform. Then we performed a microbead-based single-molecule-counting immunoassay.

Then, we discuss and conclude the study in **Chapter 6**.

## Chapter 2 Methodology

This chapter describes the fabrication of the microfluidic platform for simultaneous imaging of the bilateral head sensory neuron of *C. elegans* and a biomarker detection system using microbead-based immunoassay in femtodroplets. The devices are operated using both syringe pumps and air-pressure. Also, image acquisition and analysis are described in detail. Besides, molecular biology to express the GCaMP at target neuron and how to culture and screen the worm are described. Then, enzyme experiment both as bulk and in the femtodroplet, is described. Finally, the methods for capture bead preparation and immunocomplex formation are described.

### 2.1 Microfabrication

#### 2.1.1 Overview of the PDMS device fabrication

The microfluidic device was fabricated using standard soft lithography techniques.[218] A master for moulding the PDMS device was built as a patterned negative photoresist attached on a silicon wafer. Then, liquid PDMS was cured on the master. Then, the moulded PDMS was irreversibly bound to the substrate (**figure 2.1**).

The device was designed with AutoCAD (Autodesk). The master was fabricated by spin-coating a negative photoresist (SU8-2005 or SU8-2025 or SU8-2075, depending on the target depth of the microfluidic channel, Micro Chem) on a silicon wafer. An adhesion enhancer (OmniCoat, Micro Chem) was spin-coated on the wafer (500 rpm for 5 seconds and 3,000 rpm for 60 seconds) and baked in a dry oven at 200°C for 1 minute before deposition of the photoresist to enhance adhesion between the photoresist and the wafer. Then, approximately 3 g of the photoresist was carefully placed on the silicon wafer avoiding bubble formation and spun by a spinner (model 6000, Electronic Microsystem). The silicon wafer was initially spun at 800 rpm for 5 seconds and ramping up to 1,300-3000 rpm for desiring thickness at an acceleration rate of 300 rpm/second and maintained for 60 seconds. The spinning speed and the viscosity of the photoresist have a substantial effect on the thickness of the photoresist. For example, the thickness of SU8-2005 spun at 2800 rpm was 3.9  $\mu\text{m}$ , SU8-2025 at 1600 rpm 40  $\mu\text{m}$ , SU8-2075 at 1300 rpm 178  $\mu\text{m}$ . We referred the material information from MicroChem to achieve the desired thickness of the photoresist. Then, the photoresist spread was soft baked at 65°C for 1-5 minutes and 95°C for 1-25 minutes, depending on the thickness of the photoresist. Then, UV was irradiated to the photoresist

as the designed pattern using a direct laser writing system (MicroWriter MLTM, Durham Magneto Optics). A post-exposure bake further progressed the polymerisation of the photoresist at 65°C for 1-7 minutes and 95°C for 5-35 minutes, depending on the thickness of the spun photoresist. The unexposed photoresist was washed off by developing using 2-Methoxy-1-methyl ethyl acetate (Rohm and Haas Electronic Materials) with gentle agitation. The wafer was hard-baked in the oven at 220°C for 10 minutes. Alternatively, for soft baking and post-exposure baking, ramping up the temperature from room temperature (RT) to 60°C at the increasing rate of 6°C min<sup>-1</sup>, maintaining for 0.5-3 hours at the plateau and ramping down to RT at the decreasing rate of 0.67°C min<sup>-1</sup> were carried out.

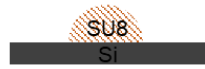
Then, the wafer was baked on a hot plate (Model 1000-1, Electronic Microsystem) at 65°C for 1-5 minutes and 95°C for 3-30 minutes, direct laser writing system was used to illuminate a laser (375 nm, 200-3000 mJ/cm<sup>2</sup>) on the photoresist to initiate photo polymerisation.

For silanisation on the surface of the master, the master was treated with oxygen plasma (Zepto, Diener electronic, 50 W, 30 seconds), and put in the vacuum chamber with 1H,1H,2H,2H-perfluorooctyltriethoxysilane (200 µL, Sigma Aldrich) for 17 hours of overnight incubation.

For PDMS moulding, a conventional PDMS kit (Sylgard184, Dow Corning) was used. The liquid PDMS mixture (base: cross-linker = 10:1 in weight) was then poured on the master and cured at 75°C for 50 min. The PDMS slab was peeled off the master, and inlet holes were punched using a biopsy punch of which the diameter is 0.8 mm or syringe needle 0.6 mm.

The PDMS slab was covalently bound to substrate, glass or a fully cured thin PDMS slab (2 mm thickness), with an oxygen plasma (50 W, 30 seconds) treatment.

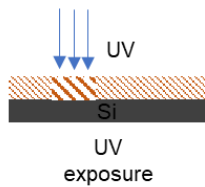
- Master fabrication



spinning



Soft baking



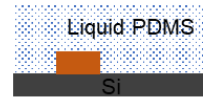
Post exposure baking



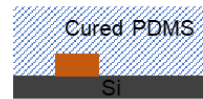
Developing



- PDMS moulding



Curing



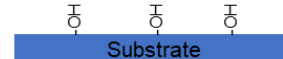
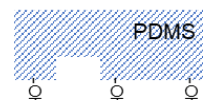
Peeling off



- Irreversible bonding of PDMS onto substrate



O<sub>2</sub> plasma



Bound



Figure 2.1 Scheme of PDMS device fabrication.

## **2.1.2 Multilayer master and PDMS device**

### **2.1.2.1 Multilayer master**

A Multilayer master was designed to fabricate a microfluidic device which contains more than two different height channels. The protocol for building multilayer master was adapted from Shim *et al.*[205] It was fabricated by spinning the photoresist, soft-baking and exposure of the pattern for one pattern followed by a spinning of the second layer of the photoresist, baking and exposure of another pattern. Then, the wafer was post-exposure baked. The photoresist which was not polymerised was washed out in the development step. (Scheme in **figure 2.2**). Multilayer master fabrication was applied to build the second layer of the wormhead device in chapter 4 and droplet flow layer in chapter 5.

### **2.1.2.2 Multilayer PDMS device fabrication**

Multilayer PDMS devices were fabricated to achieve multiple depths of the channel or to integrate functional modules such as air-pressure driven valves or traps. The protocol for multilayer PDMS devices was adapted from Shim *et al.*[205] Two PDMS slaps were moulded using their own master. Two layers are bound together by either an additional baking step after the alignment or oxygen plasma treatment (Scheme in **figure 2.3**).

An additional baking method was employed for the construction of the femtodroplet immunoassay device in chapter 5. In detail, master 1 for droplet flow channel as the top channel and master 2 for the embedded valves and trap as the bottom channel were built. PDMS 1 was fabricated by pouring the PDMS mixture (Base: cross-linker = 5:1) and curing at 70°C. PDMS 2 was fabricated by spinning the PDMS mixture (Base: cross-linker = 20:1) to achieve approximately 15 µm of the PDMS film between the top and bottom channel, for example, 25 µm high master and 40 µm thick PDMS layer. The thin PDMS 2 on the master 2 was partially cured by baking the master 2-PDMS 2 on the thermoplate (95°C, 6 minutes). After the partial curing, the PDMS 1 slap for the top channel was aligned and attached to the PDMS 2. Then, the PDMS 2 - PDMS 1 on master 2 was completely cured on the thermoplate (95°C, 30 minutes). The boundary of the PDMS 2-PDMS 1 was cut using a scalpel. Then, the conjugated device was peeled off the master 2. After detaching, the PDMS 2-PDMS 1 slap was covalently bound to substrate by exposing to oxygen plasma for 30 seconds and locating the reactive surfaces meet together.

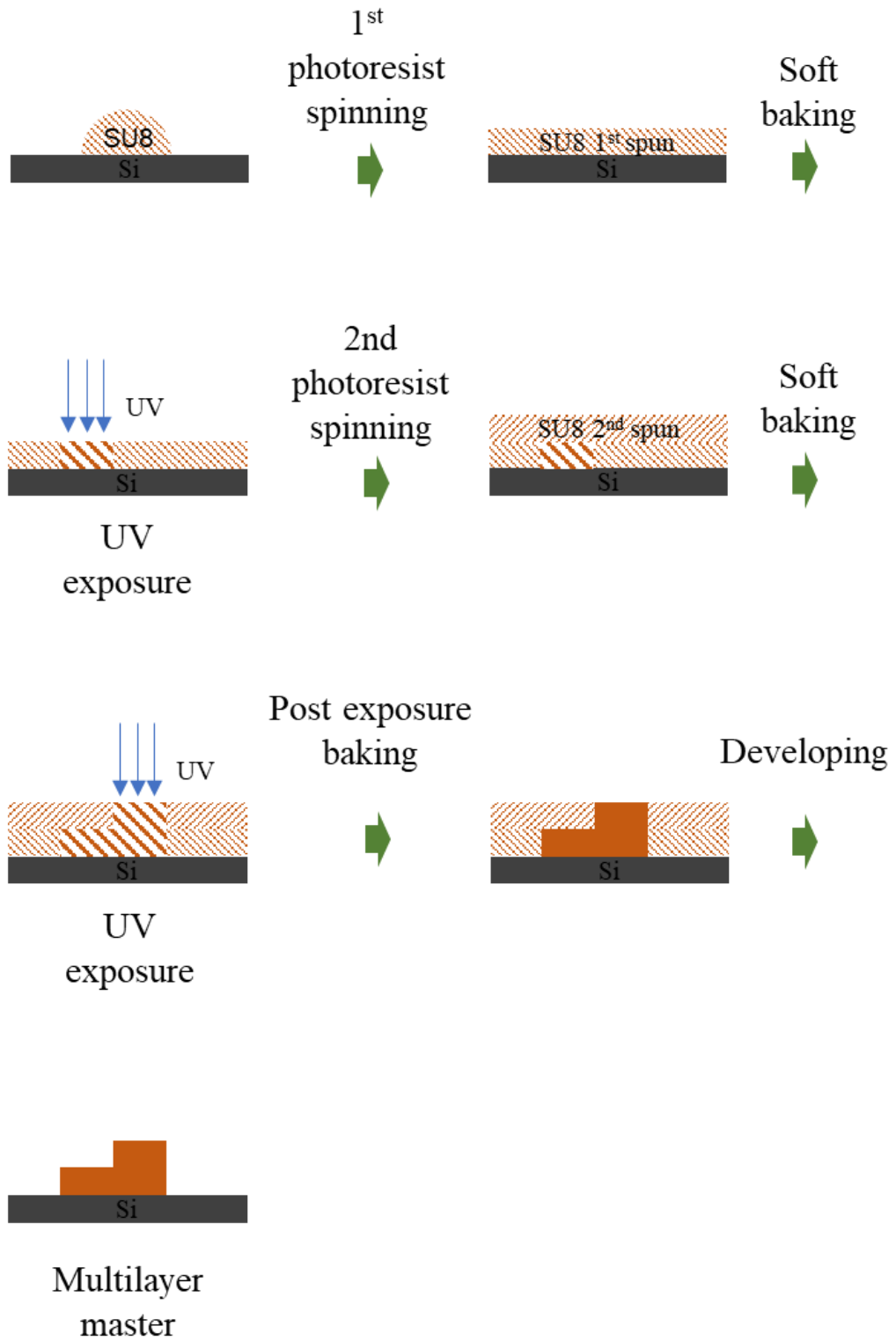


**Figure 2.2** Scheme of the process to fabricate multilayer master.

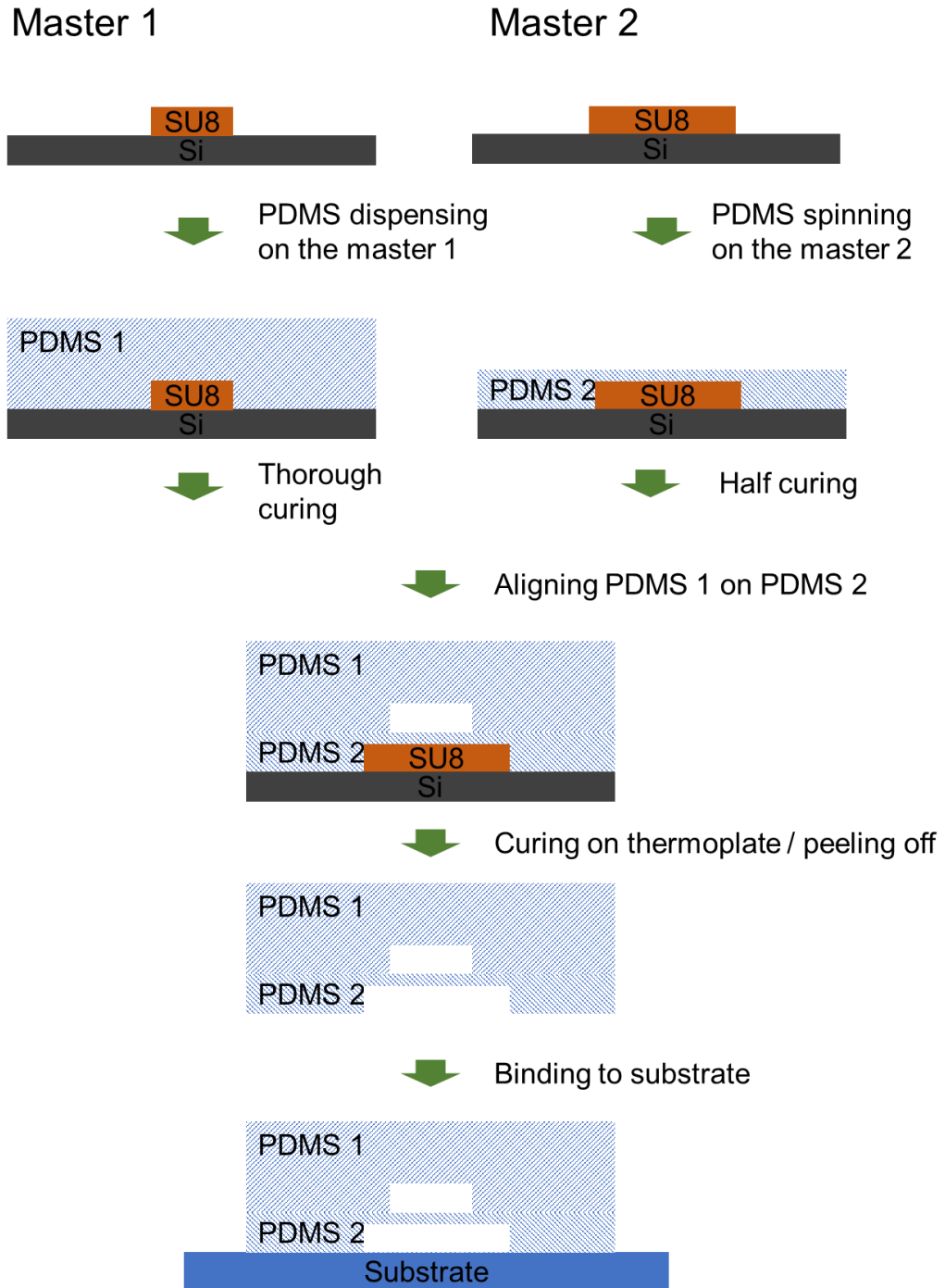


**Figure 2.3** Scheme of the process to fabricate a Multilayer PDMS device.

## 2.2 Fluid control

### 2.2.1 Air-pressure driven fluid control

The pressure applied to the solutions from compressed air, are controlled by a manifold and a regulator. The experiments are carried out under 5-10 psi of pressure. A vacuum pump (50 mbar, Dymax 14, Charles Austen Pump) was connected to an outlet reservoir, which applied negative pressure to the

microfluidic channel. A 3-way solenoid valve (LFAA0380000C, Lee Company) was used to control an application of the control buffer. The solenoid valve was operated by a controller (Genuino 101, Arduino) and custom micromanager plugin [219] (**figure 2.4**).

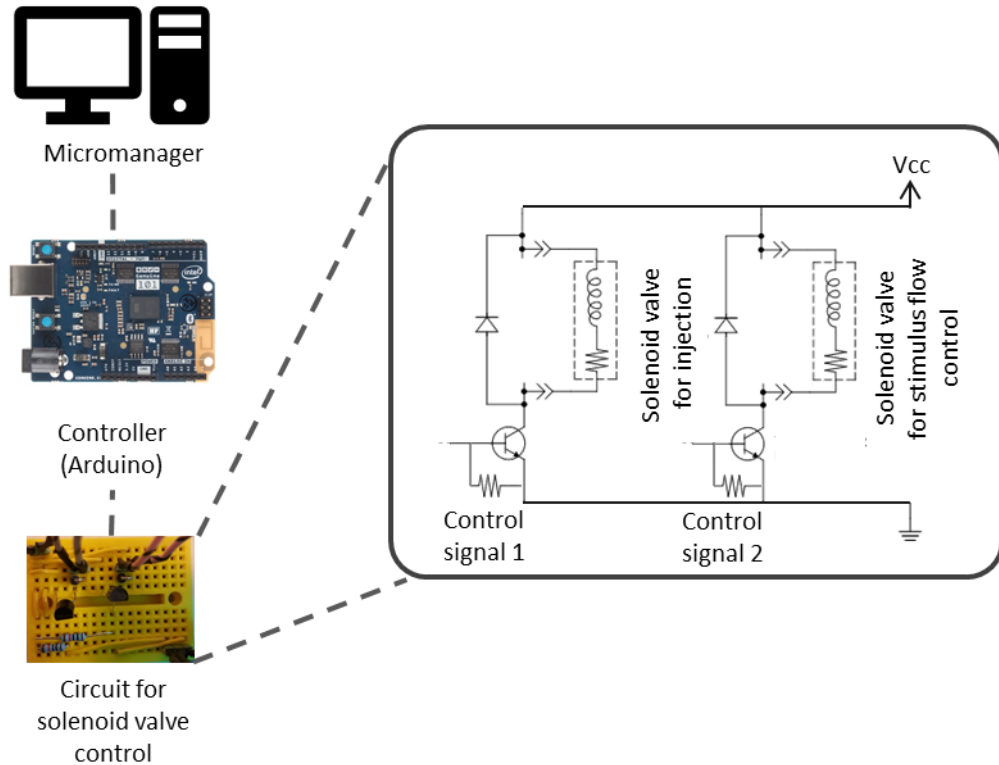


**Figure 2.4** solenoid valve controller.

### 2.2.2 Worm loading and treating stimulus flow to the amphid of the immobilised *C. elegans*

Worms were loaded into the microfluidic device using methods as follows. An individual worm was picked from a media plate and released into a droplet of syringe filtered (0.2  $\mu\text{m}$  polytetrafluoroethylene (PTFE), VWR) CTX buffer (25 ml 1 M  $\text{KPO}_4$  buffer (pH6.0), 1 ml 1 M  $\text{CaCl}_2$  and 1 ml 1 M  $\text{MgSO}_4$  were mixed and filled up to 1,000 mL with deionised water).

The worm, encapsulated in the droplet, was loaded into a syringe that transported the worm to the device. The worm was gently injected into the inlet hole of the device by a hand-pressing plunger. When measurement was completed, the worm was flushed out of the device by pressing the injection syringe. The stimulus was prepared by dissolving NaCl in CTX buffer.

After immobilisation of the worm, it was incubated for 5 minutes to settle down. Blue light (480 nm) was illuminated before the application of NaCl to habituate the worm to the blue light, as ASH is known to respond to blue light. [107]

For ASE, a pulse of NaCl upshift and downshift between 50 mM to 100 mM with a duration of 60 seconds was introduced. The start of the upshift was set as 0 seconds. The fluorescence image was recorded between -2 to 120 seconds.

And for ASH, 3 seconds pulse of the NaCl (0 mM to 0, 100, 200, 300, and 500 mM) were applied. The fluorescence image was recorded between -2 to 10 seconds.

## **2.3 Image acquisition and analysis**

### **2.3.1 Fluorescence image acquisition**

Optical images are taken using an epi-fluorescence inverted microscope (BIM800F, Bioimager) equipped with a 40x long working distance lens (BIM5-40xF, NA = 0.6, working distance = 2.2 mm, Bioimager) and a mercury lamp (Bum-HBOB, 100W, Bioimager). The excitation light was passed through a 10% neutral density filter (NE10Bm Thorlabs). And spectrally filtered and separated using cube filters (excitation  $480 \pm 15$  nm/ emission  $535 \pm 20$  nm and  $559 \pm 17$  nm/ emission  $630 \pm 35$  nm, Chroma Technology Corporation). Images were captured with an EMCCD camera (IXON3-897, Andor Technology) (range between 0.031 and 1 second). A custom-made MicroManager plugin [219] was used to coordinate the stimulus delivery and image capture.

### **2.3.2 Tracking and calcium image analysis of the bilateral sensory neurons of *C. elegans***

The software for tracking and calcium image analysis was built by Christopher Brittin. We used an adaptive correlation filter to track and measure neuron fluorescence. To control for motion artefacts, we tracked neurons using an adaptive correlation filter. A rectangle ROI1 was manually set around the left and right cell bodies. The ROI1 was used as the tracking window for the Minimum Output Sum of Squared Error (MOSSE) correlation filter.[220] Within the ROI1, the motion of the cells was significantly reduced. To measure the fluorescence, we set a rectangle ROI2s around each neuron. We defined the fluorescence within the ROI2 as the signal fluorescence  $F(\text{sig})$  and fluorescence outside the ROI2s but still within the rectangular ROI1 as the background fluorescence  $F(\text{bgr})$ . The effective fluorescence of the cell was

defined as  $F = F(\text{sig}) - F(\text{bgr})$ . The intensity change of the cell was defined as  $\Delta F = F/F_0$ , where  $F_0$  is the mean fluorescence intensity that is averaged during 2 seconds right before the delivery of stimulus. The neurons were determined to be responsive when their peak intensities exhibit higher than 1.35, and to be hyperpolarized when the intensities lower than 0.65. This threshold was set after browsing all the numerical data and its corresponding image files.

## 2.4 Molecular biology and culture of *C. elegans*

### 2.4.1 Molecular biology

The ASH::GCaMP3 strain was a kind gift from the Bargmann lab (CX10979). The ASE::GCaMNP was from Cohen lab (CB41.1) and microinjection for expressing GCaMP was carried out by Christopher Brittin. We expressed GCaMP under the *flp-6* promoter, which is expressed in both ASEL and ASER. A 3kb genomic fragment immediately upstream of the *flp-6* gene was PCR amplified from wormbank fosmid WRM068aB09 using primers 5'–ACAGGCCGCGCCGAAGACTAAGGTGTTTCGATCG and 3'–AAACCCGGGCCACGAGAGTTCATATTCTGG. The amplicon was inserted into a pSM:GCaMP3 vector (also a kind gift of the Bargmann lab) using restriction sites *FseI* and *SmaI*. Germline transformation was carried out by standard microinjection techniques (Mello *et al.*, 1991). *flp-6::GCaMP* was co-injected with a *unc-122::RFP* coelomocyte marker at concentrations of 60 ng/ $\mu$ L and 20 ng/ $\mu$ L, respectively, into a wild-type (N2 Bristol) worm obtained from the Caenorhabditis Genetics Center (Minneapolis, MN, USA).

### 2.4.2 Worm culture and screening

*C. elegans* was cultured on the nematode growth medium (NGM) plate. The NGM plate was produced as follows. 1.7% (w/v) of Agar, 50 mM NaCl and 0.25% (w/v) peptone were suspended in 975 mL of deionised H<sub>2</sub>O and autoclaved for 50 minutes to sterilise. Then, 1 ml 1 M CaCl<sub>2</sub>, 1 ml 5 mg/ml cholesterol in ethanol, 1 ml 1 M MgSO<sub>4</sub> and 25 ml 1 M KPO<sub>4</sub> buffer (pH6.0) was added and swirled before the gelation. The medium was moved onto Petri-dishes and cooled down to room temperature (RT). The NGM plates were stored at 4°C for further use.

For seeding, liquid cultured *E. coli* OP50 was applied (0.1 mL) on the NGM plates to feed the worm. The *E. coli* was inoculated to 5 mL LB broth and incubated in 38°C incubator overnight.

The screening of the genetically modified worm was screened on the fluorescence microscope (BIM800F, Bioimager). The worms only expressing fluorescence marker in coelomocyte and GCaMP fluorescence in the target neurons were picked and moved to a new seeded NGM plate using a sterilised platinum wire.

## 2.5 Femtodroplet immunoassay

### 2.5.1 Enzyme reaction kinetics

B-galactosidase hydrolyses fluorescein-di- $\beta$ -D-galactopyranoside (FDG) sequentially into fluorescein monogalactoside (FMG) and then to fluorescein, highlight fluorescent. Enzyme reaction kinetics study was carried out using a spectrophotometer.

The final concentration of  $3.6 \times 10^{-3}$  unit /mL (5 pM)  $\beta$ -galactosidase and  $2.4 \times 10^{-3}$  unit /mL (1 unit is the amount of enzyme which can convert 1.0  $\mu$ mol of substrate into product) streptavidin- $\beta$ -galactosidase (estimated as 200 pM, based on the molecular weight of the protein being 116 kD) were prepared and mixed with FDG (final concentration between 1  $\mu$ M and 220  $\mu$ M for  $\beta$ -galactosidase and 2  $\mu$ M and 500  $\mu$ M for streptavidin- $\beta$ -galactosidase) in the quartz cuvette. The rate of fluorescence generation (excitation/emission =  $492 \pm 10$  nm/  $535 \pm 10$  nm) was converted to fluorescein equivalent units by comparison with a fluorescein standard curve. The initial velocity was calculated by measuring the slope of the increased intensity by time in 1-2 minute interval. All the concentrations prepared were excessive enough to regard that the enzyme reaction rate is an initial velocity.  $K_m$  and  $V_{max}$  was estimated by Michaelis-Menten equation.

$$v = \frac{V_{max}[S]}{K_m + [S]} \quad (\text{Equation 2.1}) [221]$$

, where  $v$  is the rate of formation of the product,  $V_{max}$  is the maximum velocity of the reaction,  $K_m$ , the Michaelis constant, represents the substrate concentration at which the reaction rate is half of  $V_{max}$ , and  $[S]$  is the concentration of the substrate

### 2.5.2 Fluidic setup and valve operation for femtodroplet immunoassay device

The fluids were loaded into individual gastight syringes (Hamilton) and injected into the microfluidic device, driven by syringe pumps (Harvard Apparatus). Protein solutions or bead suspensions were co-injected with a solution of substrate (500  $\mu$ M FDG) in PBS containing 0.1% v/v Tween-20

(aqueous phase) into the device and mixed before droplet formation at the flow-focusing nozzle. Water droplets were formed in fluorinated oil (HEF-7500, Novec, 3M) with a perfluorinated polyethers-poly(ethylene) glycol (5% w/w (oil phase)).[205] Each phase was injected as the volumetric flow rate of 7~300  $\mu\text{l h}^{-1}$ .

The valve and trap which were set up underneath the liquid flow channel were driven by air pressure. When the pressure was applied, the valve and/or trap were expanded and the PDMS film forming the wall of the liquid channel was stretched. Consequently, the operating valve was able to block and release flow, and the trap located underneath the reservoir enabled immobilisation and release of the droplets.

### **2.5.3 Measurement enzyme reaction in the femtolitre droplet**

$\beta$ -galactosidase was suspended in PBS with 0.5% (v/v) of Tween-20 and loaded into a glass syringe, and fluorescein di( $\beta$ -D-galactopyranoside) (FDG) (250  $\mu\text{M}$ ) was prepared in PBS with 0.5% (v/v) of Tween-20 and loaded into an identical glass syringe. Additionally, fluorinated oil (HFE-7500) mixed with 5% (w/w) of surfactant (perfluorinated polyethers-poly(ethylene) glycol) was loaded into two identical syringes.[222] Both aqueous and oil phases were injected into the microfluidic device, and each corresponding phase flowed in a 1:1 ratio. The aqueous suspensions were mixed prior to passing through the flow-focusing nozzle. The femtodroplets, which contained FDG and  $\beta$ -galactosidase, were generated in the fluorinated oil (HFE-7500, Novec, 3M). Then,  $\beta$ -galactosidase catalysed the hydrolysis of FDG and converted the substrate into two galactoses and fluorescein, which is fluorescent.

The droplets were trapped in the device and incubated for 10 min. Then, blue light was shone over the PDMS device at specific time points (0, 1, 2, 5, and 10 minutes) and the emitted green fluorescence was imaged using a mercury lamp supply unit (ebq 100, LEJ) and a motorised filter cube (K3 for ex/em: 480 nm/ 515 nm; TX2 for 560 nm/ 645 nm, Chroma's 49011 for ex/em:480nm/ 535nm). Images were acquired by an EMCCD camera (iXon3, Andor) connected to a fluorescence microscope (DMLM, Leica, BIM800F Bioimager) with an exposure time of 10 seconds.

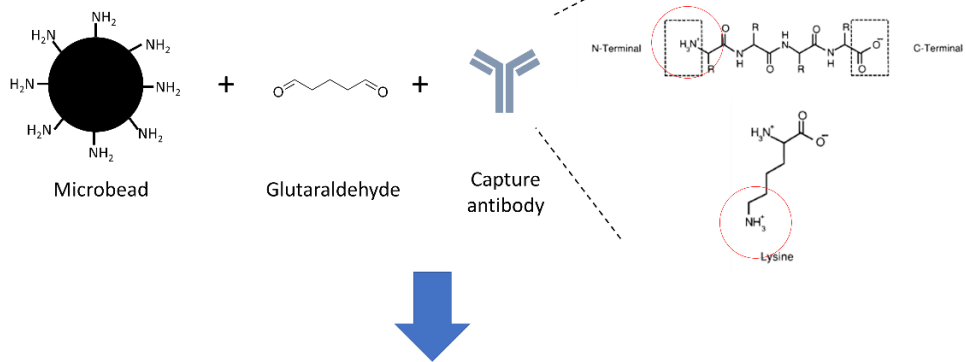
### **2.5.4 Capture bead preparation and immunocomplex formation**

Capture beads were prepared by conjugating anti-PSA antibody (R&D system) onto amino-functionalised polystyrene microbead (1 $\mu\text{m}$  diameter, Polysciences) via glutaraldehyde, an amine group cross-linker, using a commercial conjugation kit (Polysciences). We followed the procedure in the

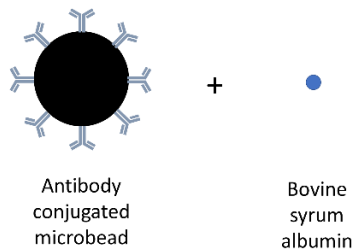
kit for the conjugation. In brief, 129  $\mu\text{L}$  (equivalent to 10 pM beads in 200  $\mu\text{L}$ ) of the microbead was diluted to 71  $\mu\text{L}$  of PBS. The bead was washed twice by centrifugation (13,000 rpm for 6 minutes), discarding the supernatant and resuspension to 200  $\mu\text{L}$  of PBS by sonication for 3 minutes. The bead was resuspended in 200  $\mu\text{L}$  of PBS. After that, 400  $\mu\text{L}$  8% glutaraldehyde in PBS was added and shaking incubated for 4 hours at RT. Then, the bead was washed twice by centrifugation (13,000 rpm for 6 minutes), discarding the supernatant and resuspension to 200  $\mu\text{L}$  of PBS by sonication for 3 minutes. After resuspending the pellet into 150  $\mu\text{L}$  of PBS, 50  $\mu\text{L}$  of 3.3 $\mu\text{M}$  capture antibody was added to be coupled and incubated overnight. Then, the microbead was separated by centrifugation (13,000 rpm for 6 minutes) and the supernatant was discarded. The pellet was resuspended in the 200  $\mu\text{L}$  of ethanolamine and shaking incubated for 30 minutes to block unreacted sites on the microbead. Then 500  $\mu\text{L}$  of 1 % w/v bovine serum albumin (BSA) solution was mixed and shaking incubated for 30 minutes to block any non-specific protein binding site, after centrifugation and discarding the supernatant. The bead was separated by centrifugation (13,000 rpm for 6 minutes) and the supernatant was discarded. At last, the pellet was resuspended in storage buffer.

The immunocomplex formed only when biomarker was bound to the capture antibody (**figure 2.5**). Antibody-conjugated capture bead (10 pM) were mixed with PSA (30 kDa, R&D systems) in a final volume of 200  $\mu\text{L}$  of PBS containing 0.1% v/v Tween-20 and incubated on a shaking incubator for 2 hours at RT. The beads were washed twice as separating by centrifugation (13,000 rpm for 6 minutes), discarding the supernatant and resuspension to 200  $\mu\text{L}$  of PBS containing 0.1% v/v Tween-20 by sonication for 3 minutes. Then, the beads were resuspended in a solution of biotinylated polyclonal anti-PSA (R&D Systems, 0.9 nM) in 200  $\mu\text{L}$  of PBS containing 0.1% v/v Tween-20 and shaking incubated for 1 hour at RT. The beads were washed twice with PBS containing 0.1% v/v Tween-20 by separating by centrifugation (13,000 rpm for 6 minutes), discarding the supernatant and resuspension. The beads were resuspended in a solution of streptavidin- $\beta$ -galactosidase (Invitrogen, 25 pM) in PBS containing 0.1% v/v Tween-20 (200  $\mu\text{L}$ ) and shaking incubated for 1 hour. The beads were then washed 6 times with PBS containing 0.1% v/v Tween-20 by separating by centrifugation (13,000rpm for 6 minutes), discarding the supernatant and resuspension to 200  $\mu\text{L}$  of PBS containing 0.1% v/v Tween 20.

### Antibody conjugation on the amino functionalised microbead



### BSA coating for quenching the residual aldehyde and preventing non-specific binding



### Capture antibody

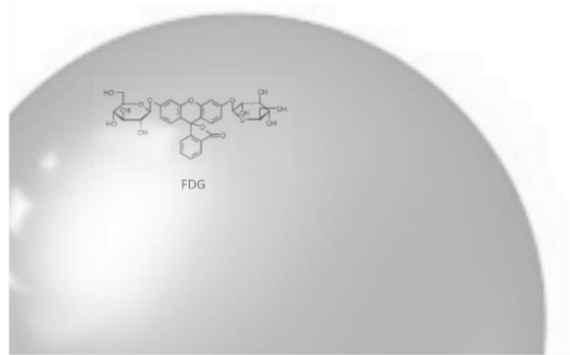


**Figure 2.5** The scheme of bioconjugation for capture bead construction. The primary amine group of the amino-functionalised polystyrene microbead and capture antibody was cross-linked by glutaraldehyde. Then bovine serum albumin (BSA) was coated to the bead in order to quench the remaining aldehyde group and cover non-specific binding sites.

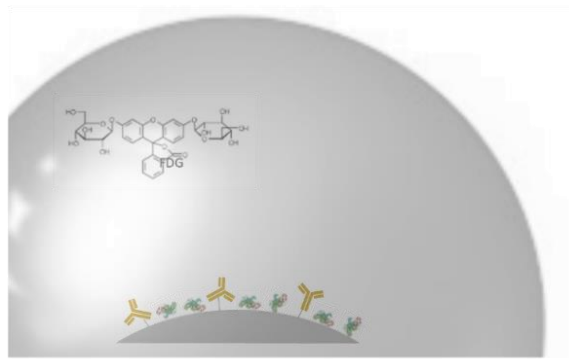
### 2.5.5 Immunoassay in the femtolitre droplet

The immunocomplex was confined in the femtodroplet and incubated in the trap for 10 min (**figure 2.6**). Then, blue light illuminated the PDMS device and the emitted green fluorescence was collected using a motorised filter cube. Images were acquired by an EMCCD camera with exposure times of 10 seconds.

No Capture bead



No biomarker



Biomarker bound on the Capture bead

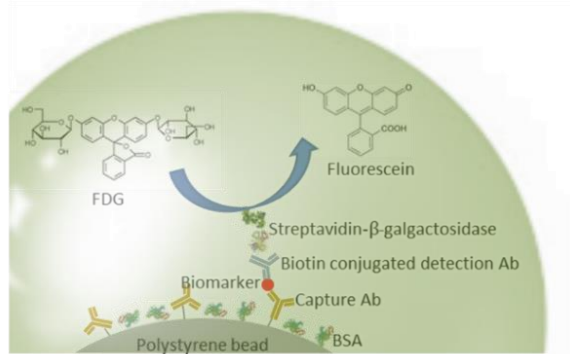


**Figure 2.6** Scheme of the immunocomplex formed on a capture bead. The immunocomplex forms only when a biomarker was bound to the capture antibody. The enzyme of the immunocomplex transduced the signal by producing the fluorescent molecule, and the fluorescein accumulated in the droplet.

### **Chapter 3**

## **Development of rotatable microfluidic device and simultaneous study of bilateral sensory neurons in *C. elegans***

The nematode *Caenorhabditis elegans* is a leading model system in genetics, development and neurobiology. Simultaneously recording activity in bilaterally symmetric cells has proved difficult in *C. elegans* because the worm enters the chip and is then immobilised when it is lying on one side of the body. This chapter deals with the development of a side-view rotatable microfluidic device that allows us to image a pair of bilateral neurons in a single focal plane of an epi-fluorescence microscope. We demonstrate the device by recording the responses of immobilised worms to controlled stimuli, focusing on the responses of two classes of head sensory neurons to changes in NaCl concentration. The results indicate that responses of ASE left and right and ASH left and right sensory neurons are stochastic. Simultaneous recordings of ASH left and right neurons tend to synchronise, pointing to a role of gap junctional connectivity. The anatomy of the *C. elegans* nerve ring makes this microfluidic approach ideally suited for the study of spatially extended pairs of neurons or larger neuronal circuits that lie within a limited depth of field.

### **3.1 Introduction**

We report a novel microfluidic device, named a side-view device, for simultaneously observing the neural activity of bilateral pairs of neurons. The microfluidic device itself is physically rotated while a worm is immobilised inside the device to place a left-right plane parallel to a focal plane. Moreover, a stimulus delivery channel is integrated into the device. Using this side-view device, we simultaneously observed the activities of left and right ASE and left and right ASH neurons in response to step changes in NaCl concentration. Whereas ASE neurons are known to be functionally asymmetric,[85, 86, 223] ASH neurons are bilaterally symmetric and are widely thought to show strong on/off, deterministic responses to noxious and other aversive stimuli.[224] Simultaneous recordings of left and right ASH neurons enabled us to quantitatively test the synchrony of responses of left and right cells as a function of NaCl concentration.

## 3.2 Device fabrication

### 3.2.1 *C. elegans* was injected into a straight PDMS device

As a preliminary experiment, a device with a straight channel with the dimension of 350  $\mu\text{m}$  wide, 220  $\mu\text{m}$  high and 12 mm long was built with PDMS and worm suspended in CTX buffer was injected into the device in order to observe the orientation and movement of the worm. A strain with RFP expressed in the body muscle was used to image clear muscle movement of the worm. Young adults (4-day-old worms from the eggs) were selected and injected into the device. We found that the worm crawled vigorously in the channel (**figure 3.1**). We also found the worm did not cross (part of the body placed above or beneath the rest part of the body) nor twist (rotate the body clockwise or anti-clockwise along the longitudinal axis) its body in the channel with this dimension.

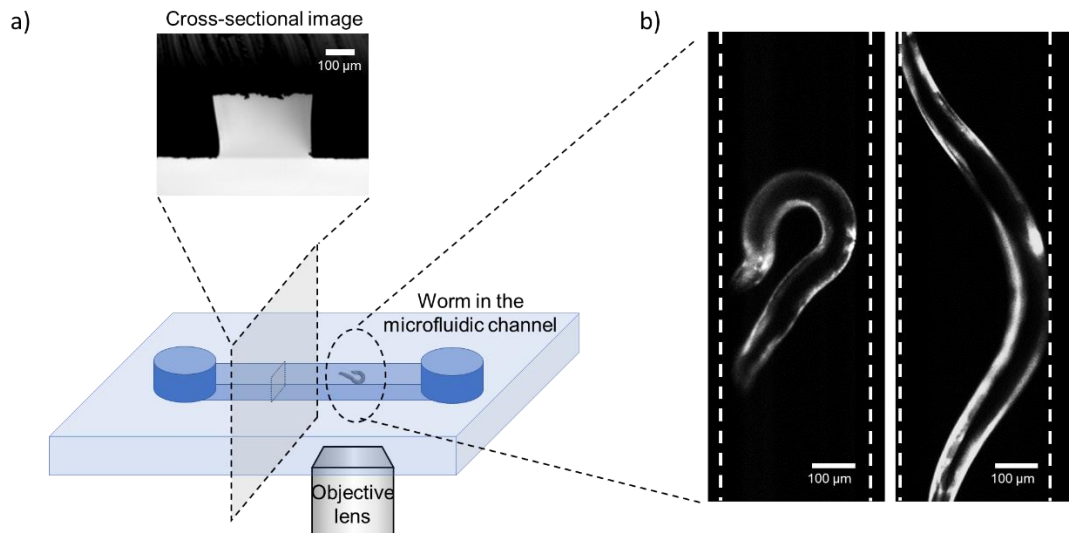


**Figure 3.1** Movement of the worm in a straight PDMS channel. a) straight channel (350  $\mu\text{m}$  wide X 220  $\mu\text{m}$  high X 12 mm long) was built and single worm was injected b) fluorescence image of the worm in the device. The fluorescence indicating body muscles are seen along the dorsal and ventral side of the body. The worm crawls in the channel actively. However, crossing or twisting are not found during the imaging.

CX10979 strain (GCaMP::ASH) was injected in the device, and its head was imaged to check how the pair of sensory neurons are seen in the device. As a result, we found fluorescent cells in the head of the worm. However, movement of the head disturbed the focusing of the neurons (**figure 3.2**),

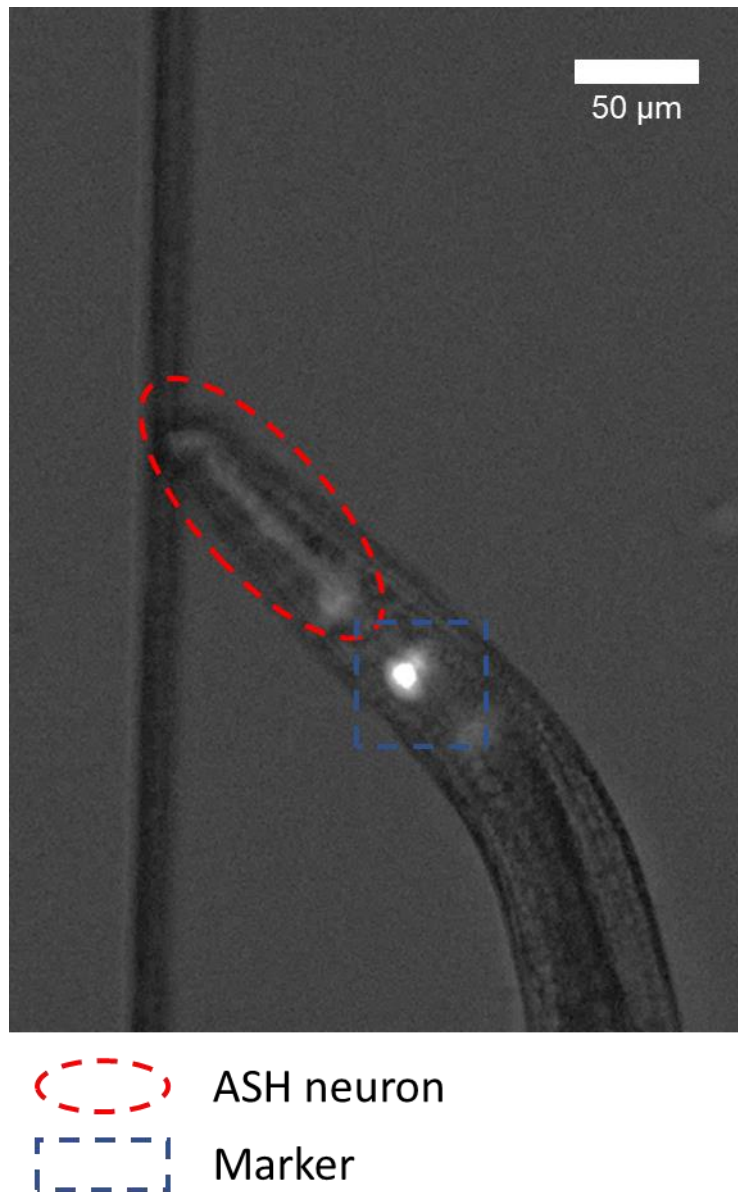


**Figure 3.2** GCaMP fluorescence in ASH neuron of CX10979 strain in the microfluidic channel. The continuous moving organism is hard to image without tracking or immobilisation.

### 3.2.2 The 1<sup>st</sup> design of the device

Two concepts of devices were designed to immobilise the body of the worm. One is a modified straight device with worm traps in the middle of the channel (modified straight device), and the other is T shaped device (T device).

#### 3.2.2.1 A modified straight device with diverted inlet and traps

The modified straight device was designed as a 400  $\mu\text{m}$  wide and 6,600  $\mu\text{m}$  long straight channel with a worm trap in the middle and an additional inlet for stimulus. (**figure 3.3**). The height of the channel was determined by adjusting the spinning a spin coating of the photoresist aiming 60  $\mu\text{m}$  high. The trap

aimed to hold the head of the worm. We hypothesised that the movement of the worm would be restrained by immobilising the head and neck as the body movement of the worm initiates from the neck. We designed a 400  $\mu\text{m}$  long zig-zag structure connected to 200  $\mu\text{m}$  long straight structures as the worm has approximately 200  $\mu\text{m}$  long head. Additionally, we added narrow orifices where the head of the worm would be immobilised, and the amphid would protrude outside of the structure. We adapted the 24  $\mu\text{m}$  wide orifices from Chronis' study[56]

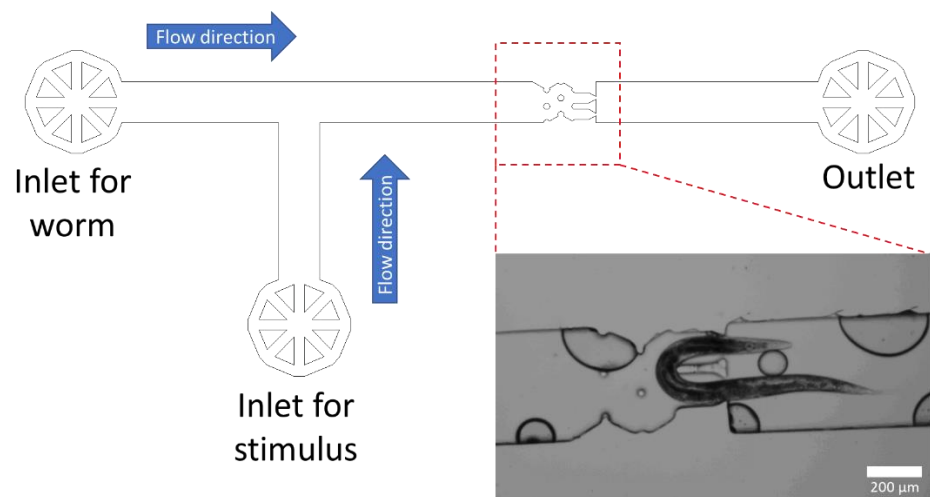


**Figure 3.3** Scheme of modified straight device and image of the worm in the channel. The worm entered the trap but was not completely immobilised. It eventually escaped the trap. (Air bubbles were in the channel).

However, we found that the head trap was not appropriate to restrain the worm. The worms escaped through the trap with their undulating movement. We needed that a trap which restrains the whole body of the worm so that escaping movement should be more limited.

### 3.2.2.2 T device

T device was designed as a wedge-shaped channel that the worm can enter and then is trapped in the end (trap), and a perpendicular straight channel connected to the end of the trap (stimulus channel), so that the head of the worm protruded to the stimulus channel, and the stimulus can be supplied to the amphid of the worm.

The trap was designed as 50  $\mu\text{m}$  wide and 1,500  $\mu\text{m}$  long straight channel with 24  $\mu\text{m}$  orifice and 50  $\mu\text{m}$  long trapezoidal head trap. The length of the whole straight channel was 5,000  $\mu\text{m}$ . The entrance of the channel was set 200  $\mu\text{m}$ , wider than the trap, for relatively easier loading. The width of the channel was gradually decreased to minimize the steep change of the flow velocity. The height of the channel was aimed to be 60  $\mu\text{m}$  high.

When the worm was injected, the worm was employed to the end of the trap by both being pushed by flow and crawling by itself. The worm was immobilised in the trap, but the trap was not able to hold the worm more than 2 minutes. The worm in the trap kept undulating and eventually escaped the trap (figure 3.4).

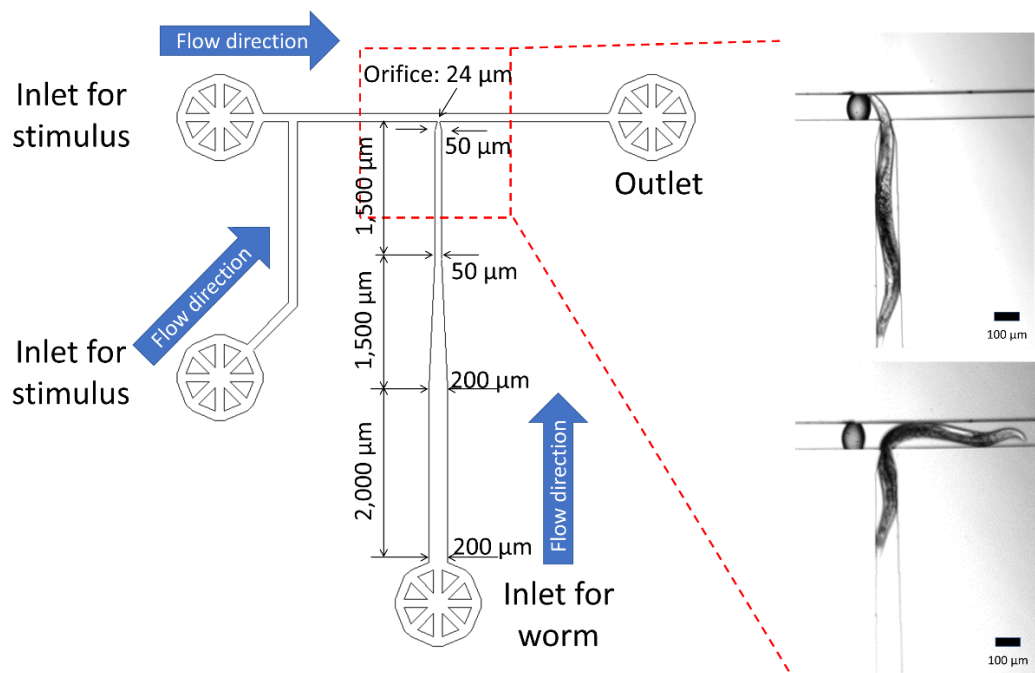


**Figure 3.4** Scheme of T device and images of the worm in the channel. The worm was injected to inlet and immobilised in the trap located at the end of the channel. The worm escaped the trap by its undulating motion.

We found that a precise whole body trap is necessary to immobilise and image the worm. Also, we found that the precise measurement of the size of the worm is needed to modify the trap design to improve the efficiency of the immobilisation.

### 3.2.3 Trap design

The trap needed to be constructed small enough to restrain the undulation of the body of the worm and wide enough for the amphid to be protruded based

on the failure of head confinement in the straight device and loose trap space in the T device. So, a straight device with long tapered PDMS device was designed to determine the width of the orifice (**figure 3.5a**). The idea comes from the wedge-shaped device array designed by Hulme *et al.* [147] and the fact that the locations of the immobilised worms in the array were slightly different among individual organism.

The length of the channel from the inlet to the tip was 9,000  $\mu\text{m}$ , and the height of the channel was aimed to be 60  $\mu\text{m}$  high. The width of the channel gradually decreases from 100 to 10  $\mu\text{m}$  (**figure 3.5a**). A 4-day- old worm was injected into the channel, and it was moved toward the end of the trap and eventually totally immobilised at a particular location in the channel (**figure 3.5b and c**). We measured the width of the channel where the amphid was placed, and it was  $22 \pm 1 \mu\text{m}$ . Then, we determined the width of the tip was determined as 24  $\mu\text{m}$  so that the amphid, the sensory organ, can be protruded to the stimulus flow. The worm was not able to crawl as the wall confined the entire body, but we observed that the distal head was continuously stretching and contracting.

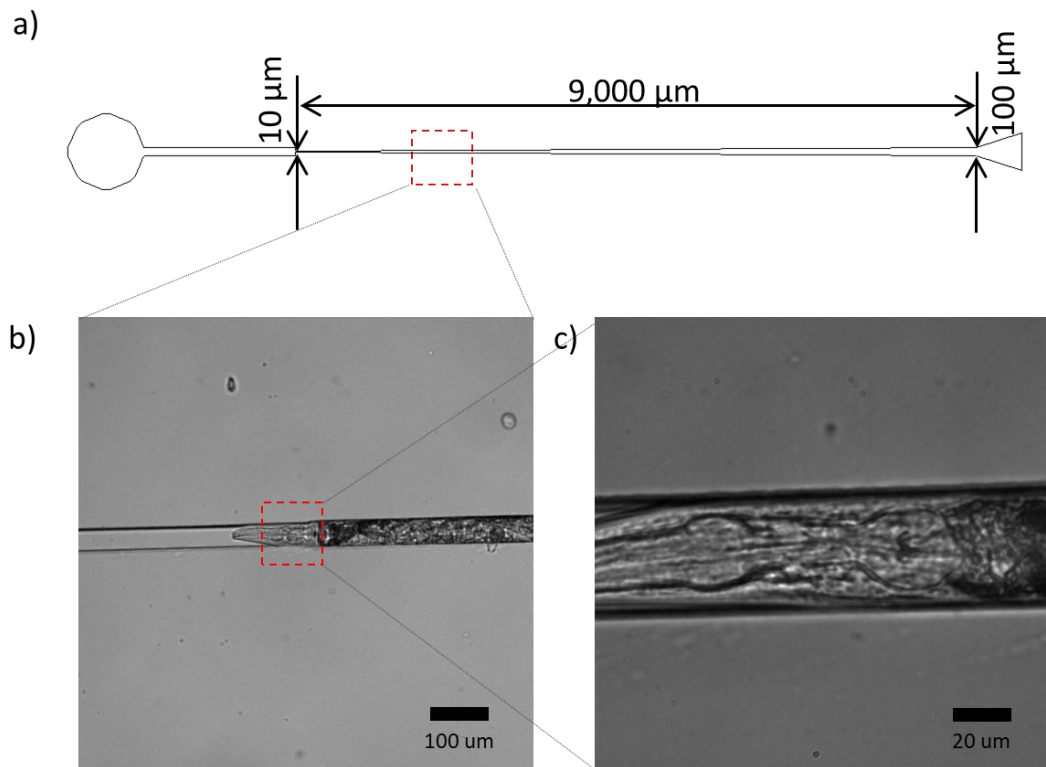


**Figure 3.5** Measurement of the size of the worm for the trap modification a) The design of the channel. b) and c) The *C. elegans* entered the channel through inlet(right) was trapped in the middle of the channel.

We used this tapered channel as a trap because it immobilises the worm completely. However, there was an issue that it takes too long to immobilise

properly; being restrained at the end of the channel with its amphid to be protruded to the stimulus channel. It took approximately 30 minutes for the worm to be immobilised in the straight channel. So, we modified the design of the channel (**figure 3.6a**). Instead of the tapered design, the shape of the channel was carefully curved as the shape of the head of the worm. The diameter of young adult *C. elegans* is about 40  $\mu\text{m}$ , so we fabricated the height of the channel aiming for 40  $\mu\text{m}$ . We found the worm immobilized in this trap within 2 minutes (**figure 3.6b**).

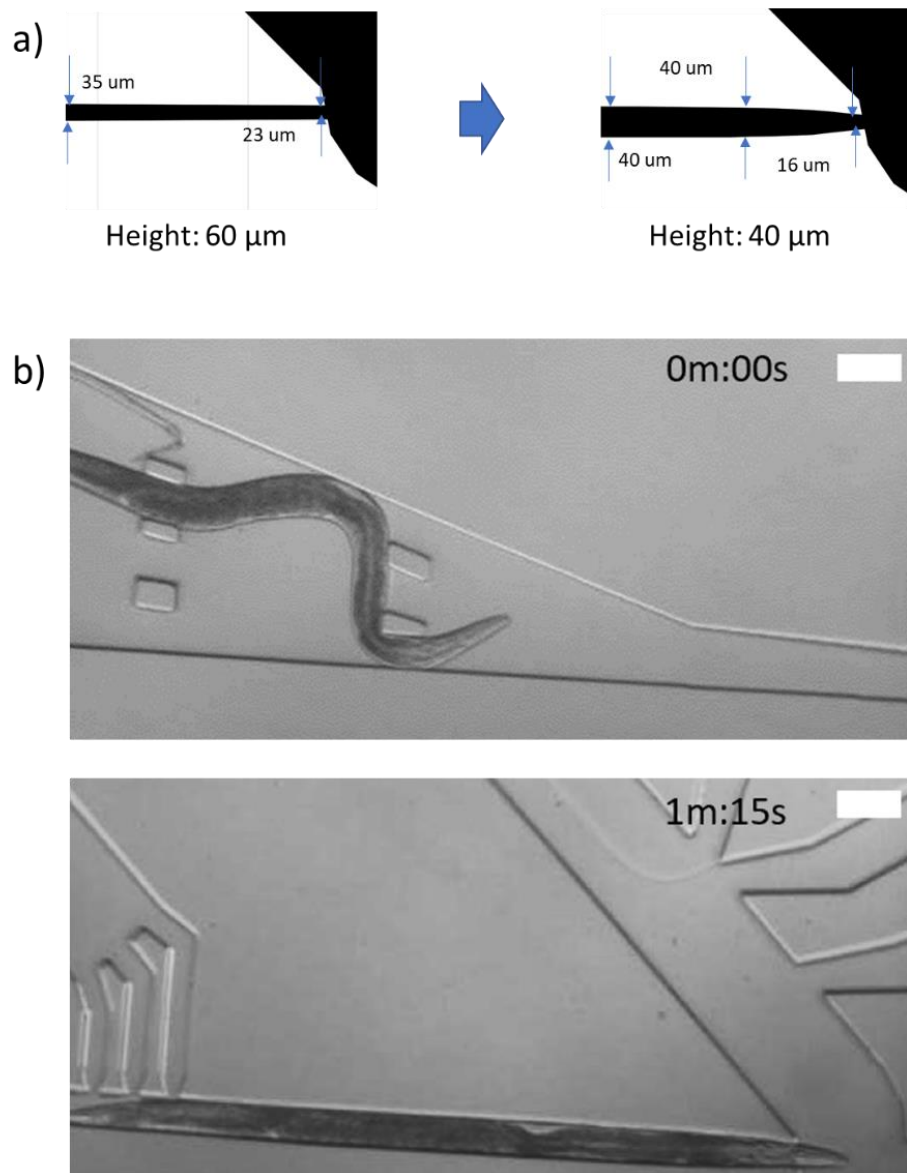


**Figure 3.6** Revision of the trap design. a) The tapered straight channel was revised to a curved shaped channel. b) The worm was delivered to the trap and completely immobilised within 2 minutes. Bar indicated 50  $\mu\text{m}$ .

### 3.2.4 Rotatable device

#### 3.2.4.1 Device fabrication

The orientation of the immobilised worms was not appropriate to image the bilateral neurons at the same time because the neurons were not in the same focal plane. The worm's body muscles are located along its ventral and dorsal sides; the worm naturally oriented itself so that it lay on either its left or right side. A 90° rotation about the anterior-posterior axis roughly places the coronal plane parallel to the focal plane, making simultaneous viewing possible. Therefore, a simple solution to the left/right imaging problem is to load the worm into the microfluidic device, let the worm naturally orient itself and then rotate the device by 90°. Additionally, a process for smoothing the surface of the side was done in order to obtain a more precise image by increasing transparency.

The design of the worm device was revised as adding stimuli supplying channel at the end of the long narrowing channel so that trapped *C. elegans* can sense the change of the environment by its amphid exposed to the supplying channel (figure 3.7). Moreover, the stimulus channel was curved to one side so that the trap can be located within the working distance of the lens when the device was rotated.

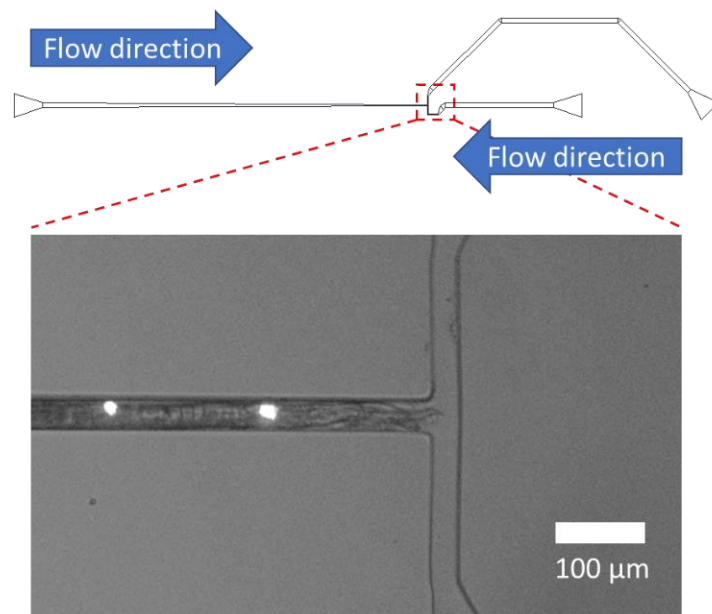


**Figure 3.7** Scheme of Side-view T device and images of the worm in the channel. The stimulus channel was designed being bent to place the trap close to the wall.

This device was fabricated with PDMS bound to a thin PDMS. These whole-PDMS devices were cut as cuboids. Then, in order to obtain smooth faces of the cut-sides, the rough surfaces were filled with additional PDMS mixture and baked on the wafer with the treated surfaces faced down. The thickness of the PDMS from the surface of the side to the channel was approximately 2 mm to secure the working distance of the objective lens of the microscope.

### **3.2.5 Surface treatment of side view device to enhance the transparency**

A side view device was fabricated to image the object through the side. However, conventional methods to produce the PDMS device merely focus on the transparency in the top view and the side faces remain untreated. It is needed to smoothen the side to achieve a clear image for observation through the side.

The PDMS slab was covalently bound to a fully cured thin PDMS slab (1 mm thickness) with an oxygen plasma (50 W, 30 seconds) treatment. The PDMS device was trimmed as a cuboid by a scalpel so that the worm trap was located at 1 mm away from the device edge. In order to obtain a flat surface on the side of the device, the rough surface was smoothened with liquid PDMS and baked on a wafer at 75°C for 30 minutes. The additionally cured device was detached from the wafer and trimmed (**figure 3.8**)

The smoothing process improved the image. The image of the channel through the turbid surface before the smoothing was distorted so that the channel was not visible clearly. The clear boundary of the channel was seen after the smoothing process. (**figure 3.9**)

We imaged the immobilised worm both on the top and through the side. The resulting image after smoothing showed both the left and right of the sensory neurons in the side view (**figure 3.10**). One of the bilateral neurons might be out of the focal plane, but we can reduce this issue by imaging both sides of the device, either top view or side view, depending on the orientation of the immobilise worm.

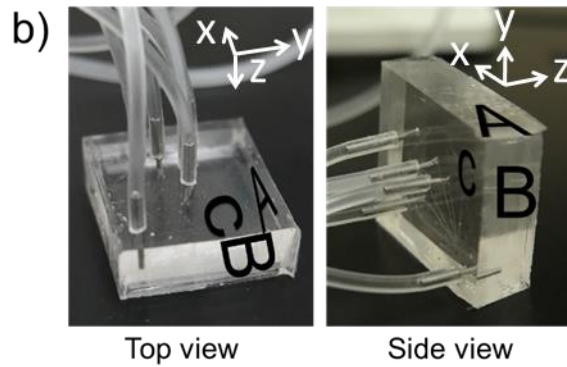
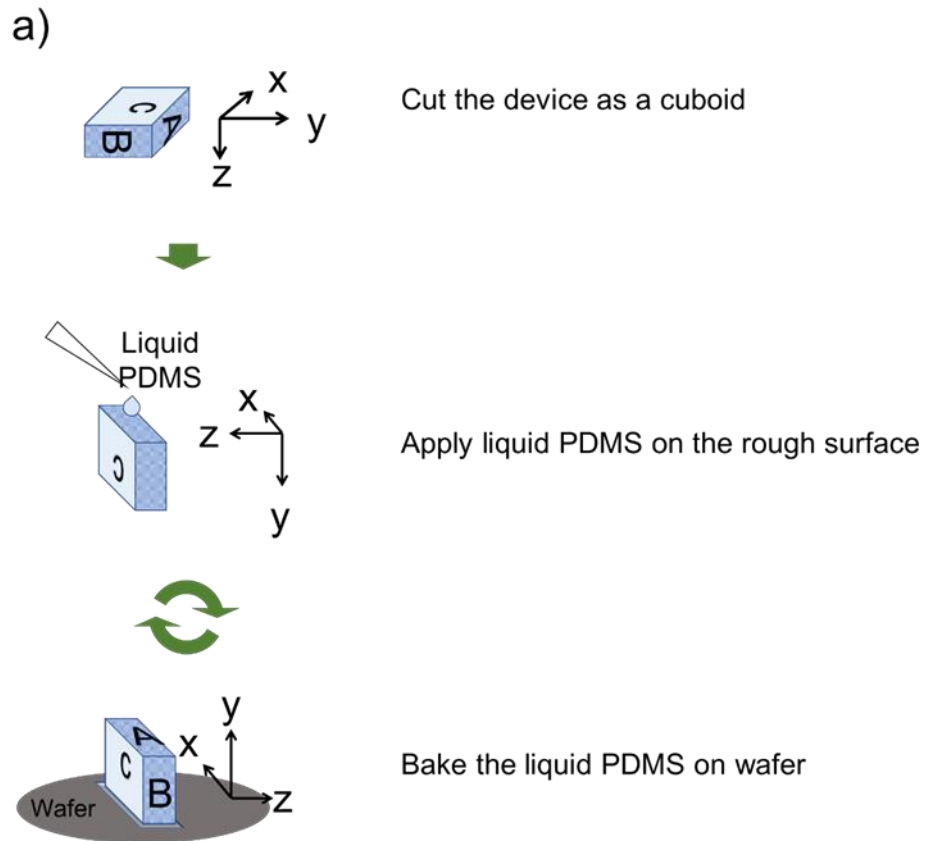


**Figure 3.8** a) Scheme of side view device fabrication. Rough surfaces of the device were smoothed (Surface A and the opposite side); b) Top view and side view setup of the side-view device on a microscope. Fluid control and imaging can be carried out with the orientation of either conventional top view (left) or side view (right) with an inverted microscope. Arrows indicate 5 mm.

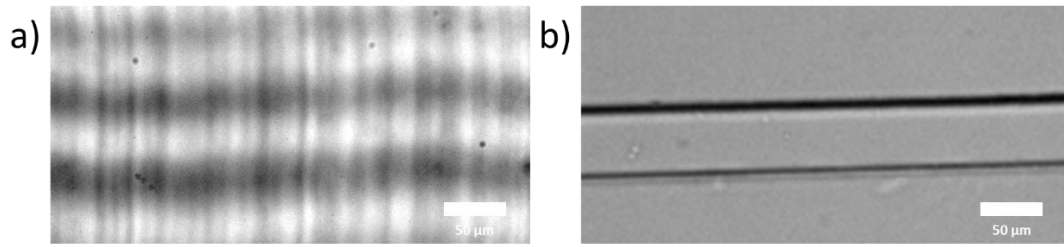


**Figure 3.9** Side view images of the channel a) before and b) after smoothing. The image was distorted by the turbid surface. Clear image of the channel is obtained after the smoothing process.

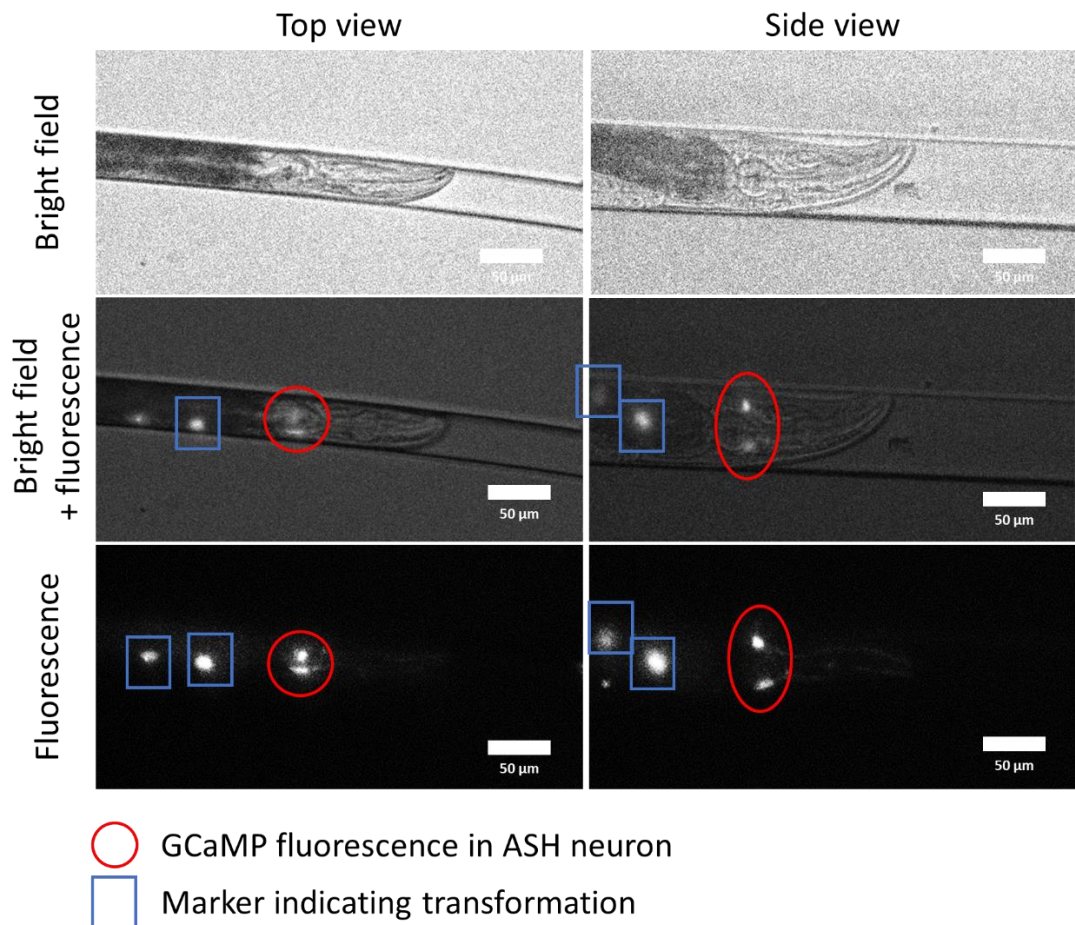


**Figure 3.10** Multiangle image of the worm immobilised in the side view chip. A CX10979 strain worm was immobilised in the channel, and fluorescent neurons are seen both in the top view (x-y plane) and side view (x-z plane) using conventional inverted fluorescence microscope. Both ASH left, and right neurons are visible in one image through side view observation.

### 3.2.5.1 Time course imaging of ASH neuron response

An ASH worm was injected to the device and stimulus (500 mM NaCl) was treated to the amphid of the worm to verify the feasibility of the side-view device. The worm was moved to the trap and then pushed until the amphid

touched the stimulus flow, which was formed at the orifice of the trap. Time-course images were taken for 100 seconds with an interval of 0.1 seconds. As a result, the fluorescence intensity of the ASH neuron, both in the cell bodies and dendrites, was increased after the amphid touched the stimulus flow (**figure 3.11**). The fluorescence intensity reached a peak in  $4.1 \pm 0.1$  seconds after the contact, then decreased but not down to the initial intensity.

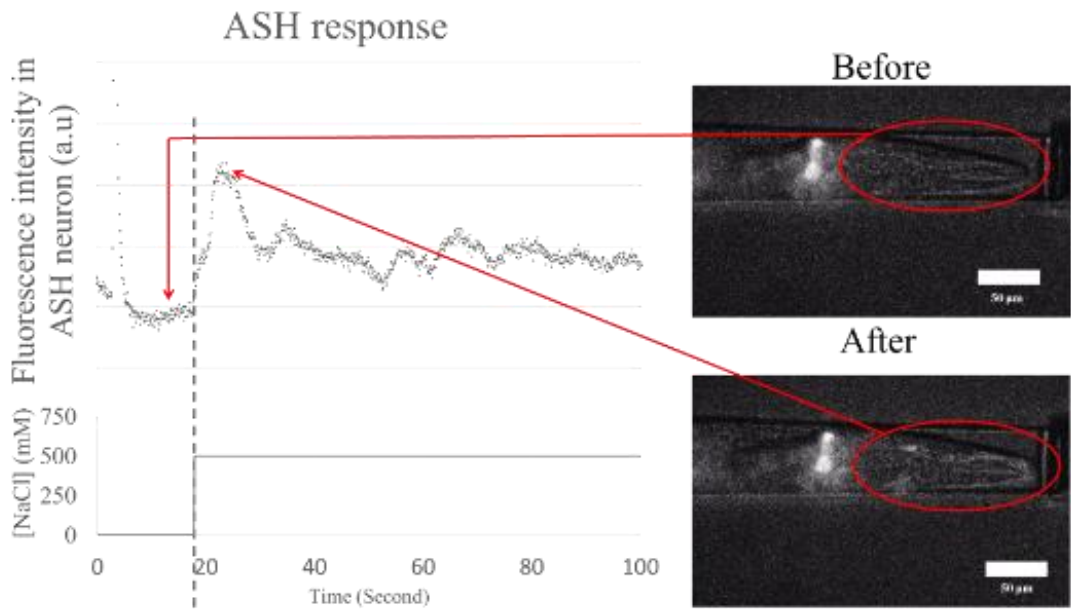


**Figure 3.11** Time course imaging of the ASH neuron. The calcium transient activity of ASH neuron was taken by stimulating the worm. We pushed the worm to the pre-set NaCl flow.

The critical issue in the current side-view device is that supplying the stimulus stream was not controllable because the stimulus stream formed too close to *C. elegans*. The amphid of the worm exposed to the stimulus flow once the worm was positioned at the trap (**figure 3.12**). So, the worm was located behind the trap and pushed to the stimulus stream in order to supply the stimulus. This 'pushing action' generates problems. This creates a risk to produce a false signal for the ASH neuron. The ASH neuron responds not only to osmotic stress but also to mechanical stress. [55, 225] So, the worm needed to be immobilised in the trap and settled down before the treating stimulus to minimise the risk of unexpected response to mechanical stress.

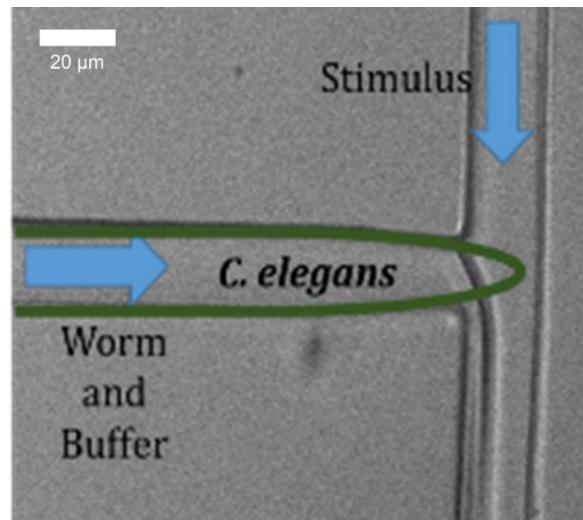


**Figure 3.12** Interface formed between stimulus and buffer flow. Stimulus flow located too close to the *C. elegans* to be immobilised.

### 3.2.6 A new design of side-view device

A revised channel was designed by adding a stimulus supply module next to the side-view trap (**figure 3.13**). We developed an all PDMS cuboid microfluidic device in which a single worm can be immobilised and exposed to soluble stimuli. The side-view device allows us to observe neuronal activities of multiple neurons in a single dorso-ventral plane (top view) or left-right plane (side view) of the worm, as shown in **figure 3.14**. The microfluidic device consists of a worm channel for trapping and immobilising a worm and a solution delivery channel for introducing a stimulus to the tip of the immobilised animal (**figure. 3.18**). The worm trap and stimulus delivery channels were adapted from an existing 'olfactory chip' described in Chronis *et al.* [56]

We optimised trap dimensions to minimise stress caused to the trapped worms due to immobilisation while minimising the worm's escape from the trap. Our design consists of an entry channel with a fixed cross-sectional area of 40 μm by 40 μm which then leads into a gradually narrowing 1,200 μm long channel with a 40 μm x 16 μm cross-section opening onto the stimulus delivery channel at the tip of the trap as explained in **Chapter 3.2.3**. The specific dimensions were optimised for young adult *C. elegans*. Using this device, 81% (129 out of 159) of immobilised worms with correct orientation (with the head facing forward) were successfully imaged.

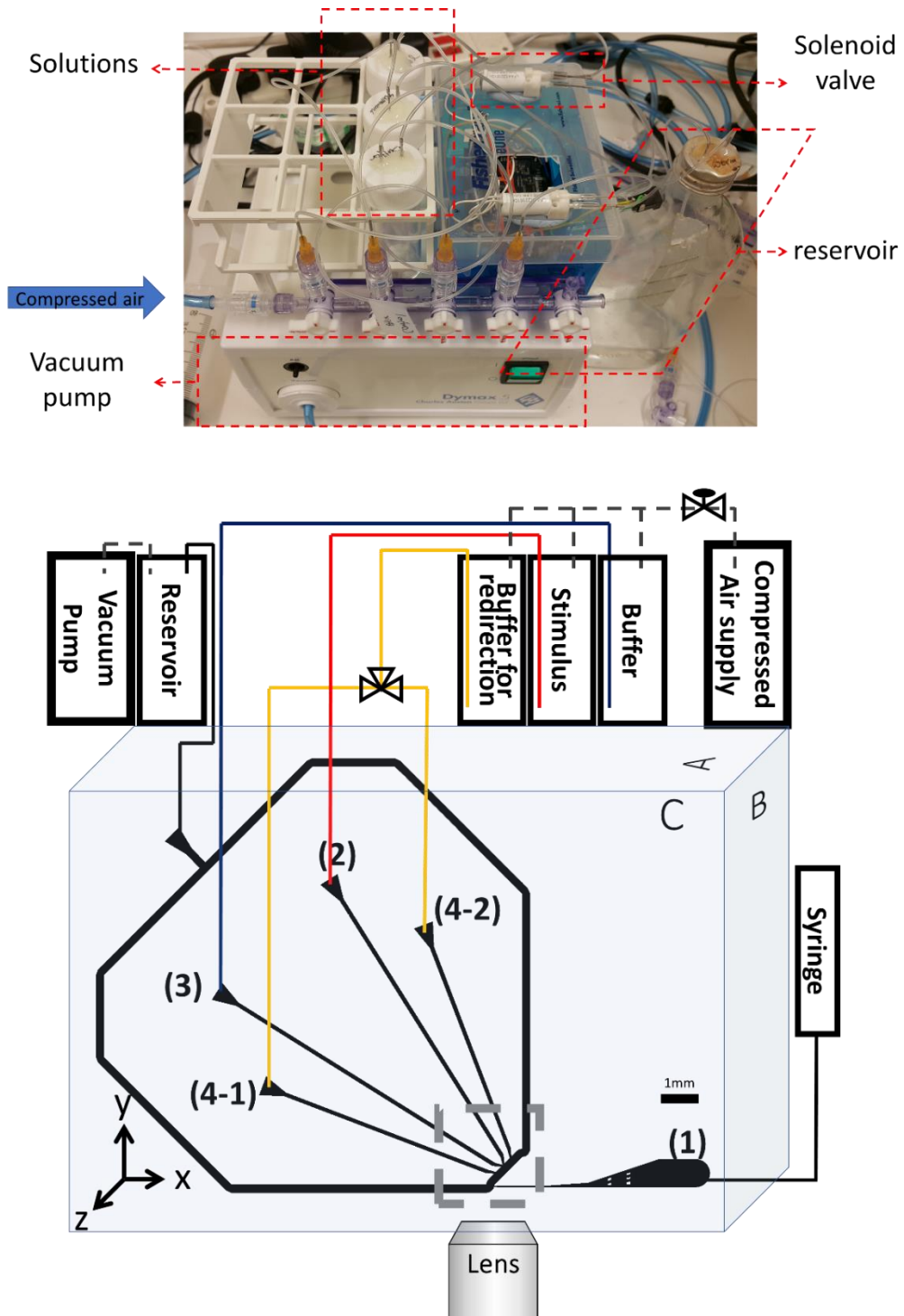


**Figure 3.13** Scheme of the microfluidic system for side view device a) pressure driven flow supply b) The scheme of the revised side view channel. Two control flows are connected to a 3-way valve to supply the pressure either of each channel. b) The principle of the device. Two control streams will be used for altering the direction of the stimulus stream. A detailed description of the flow control in the grey dashed box is followed in **figure 3.18**.

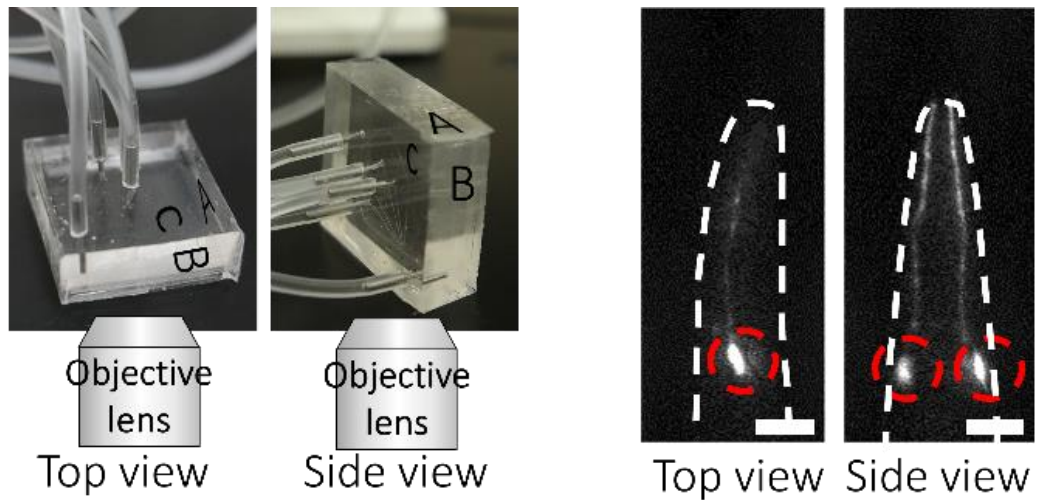


**Figure 3.14** Side view device (left) and the fluorescence images of the immobilised worm in the device (right). Scale bar indicates 20  $\mu\text{m}$ .

Worms can be manually loaded into the microfluidic device with a manually syringe-controlled delivery,[56] or a semi-automatically delivered (**figure 3.15**) or fully automatic delivery, in which worms are loaded into the device from a worm reservoir that is connected at constant pressure. [152]

Immobilised worms in the trap can be easily removed from the device by applying additional pressure to the worm trap, which enabled the reuse of the device. We imaged more than 90 worms in a single day with a single device and typically used a single device for up to two weeks.

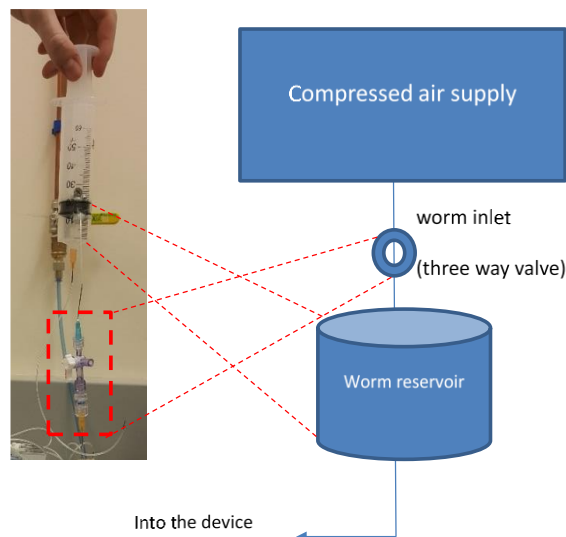


**Figure 3.15** Semi-automatic delivery device. The worms are injected into the worm reservoir through the worm inlet by syringe. The worms are loaded into the device by air pressure. The immobilised worm blocked the channel and prevented another worm from entering the trap.[152]

The stimulus delivery system was integrated with the worm trap in the microfluidic device (**figure 3.18**). Worms entered the trap by forward movement (head first) and were immobilised at the tip of the head, which protruded into the stimulus delivery channel. Flow through the channel is controlled by a four-channel module which allows either the stimulus (channel 2 in **figure 3.18**) or a buffer solution (channel 3 in **figure 3.18**) to flow onto the nose of the worm. An external three-way valve controls the relative pressures (of buffer solution) in channels 4-1 and 4-2 and is then used to switch the direction of the stimulus flow toward or away from the immobilised worm.

When worms were loaded into the device, they were initially randomly oriented with either the head or tail pointing forward. To ensure that the worms reach the trap with their heads first, an array of pillars was fabricated at the entrance of the worm trap, which significantly enhanced a probability for a worm to enter the trap with its head first (**figure 3.16**). [152] We found that 71% (65/91) of the worms entered with their head first when they were semi-automatically delivered. This is a similar result with that previously reported by Chokshi *et al.* (60 out of 85 worms).[152] When manually delivered by a syringe, the plunger can be precisely controlled to orient the head toward the trap such that more than 90% (258/272) of the worms were immobilised in the trap with their head first. This efficiency was good enough to carry out the experiment.

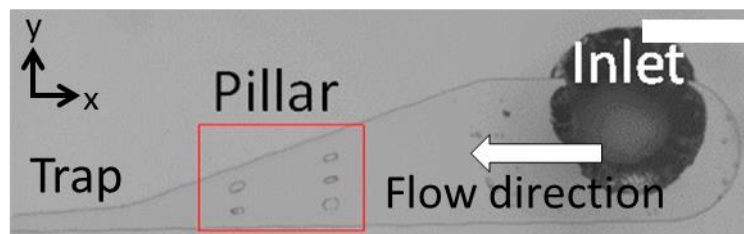


**Figure 3.16** The broad entrance region of the worm trap. The pillar structure forces a worm to enter the trap with their head first. The wide and shallow channel located at the entrance of the trap lets a worm crawl on an x-y plane, which aligns the dorso-ventral plane of a worm parallel to an x-y plane by itself. The widths between pillars were 50  $\mu\text{m}$ . Scale bar indicates 500  $\mu\text{m}$ .

In order to verify the utility of the side-view device the orientations of immobilised worms were manually assessed, with the aid of a focus knob of the microscope.

We estimated the valid value of the maximum rotation. Being both neurons in the same focal plane means that the closest z-axis distance between two neurons is less than the depth of field of the objective lens.

Depth of field (d) is defined as

$$d = \frac{\lambda \sqrt{n^2 - (A)^2}}{(A)^2} \quad [226]$$

, where  $\lambda$  is the wavelength of light wavelength ( $535 \pm 20$  nm),  $n$  is the refractive index of the PDMS (1.43) and  $A$  is the numerical aperture of the objective lens (0.6). The depth of field of the 40X lens which we used was 2  $\mu$ m.

Distance between two cells (l) was measured at the image obtained from the worm with no rotation, and it was  $25 \pm 1$   $\mu$ m. The diameter of the cell body of the neuron is known as 2  $\mu$ m.[227]

The valid value of the maximum rotation (R) is calculated as

$$R = \sin^{-1}((d + 2 \times 0.5c)/l)$$

So, both neurons are visible in one image when the trapped worm is rotated within ( $10 \pm 2$ )°

We found 76% of worms (80/105 worms) were immobilised at an angle of less than 10° relative to the desired lateral orientation (**figure 3.17**). This level of angular variation did not significantly affect the imaging quality at the desired magnification. The bilateral neuron pairs were clearly visible under fluorescence illumination, allowing for high-quality imaging of calcium signals, using epifluorescence microscopy. Worms with higher angular displacements were discarded. We note that the rapid manual or semi-automatic loading of worms into the device resulted in a wide distribution of angles compared to the finely controlled manual injection that was used to conduct the experiments.

The success of the side-view device hinges on the orientation of the worm such that its left-right plane is precisely aligned with a focal plane of the microscope. Any twist of the worm within the trap would shift at least one of the cells out of the focal plane. We exploited the fact that worms crawl by undulating in the dorso-ventral plane while lying on the left or right side of the body. A wide (700  $\mu$ m) and shallow (40  $\mu$ m) entrance channel, located before the worm trap (figure 3.13 and figure 3.16) forced the worm to undulate in the broad plane of the entrance channel. The device is first oriented on the microscope stage to view the trapping from the top view perspective and is then rotated by 90° (with the entrance channel facing down) to allow for neuronal imaging from the side-view perspective.

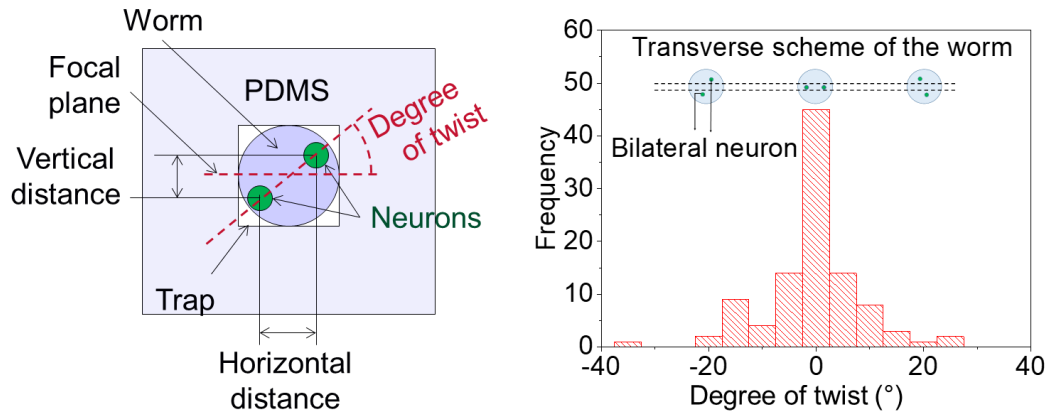


**Figure 3.17** Distribution of the twisted angle of immobilised worms was measured 76% of immobilised worms (80 / 105 worms) are twisted within 10 degrees from a focal plane. This method has a minor level of errors due to the eye-observation. The left and right sides of the worm were distinguished by observing the orientation of the immobilised worm through the top view and finding dorsal and ventral sides before the imaging through the side view.

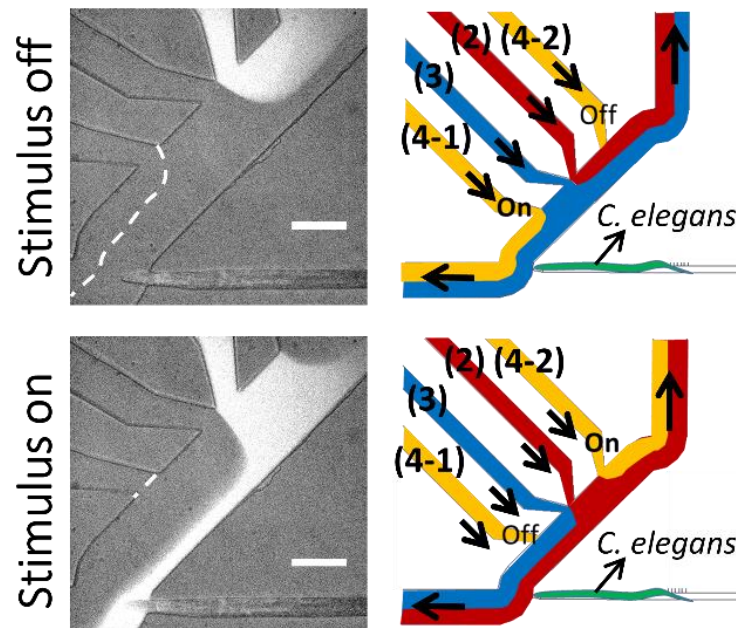
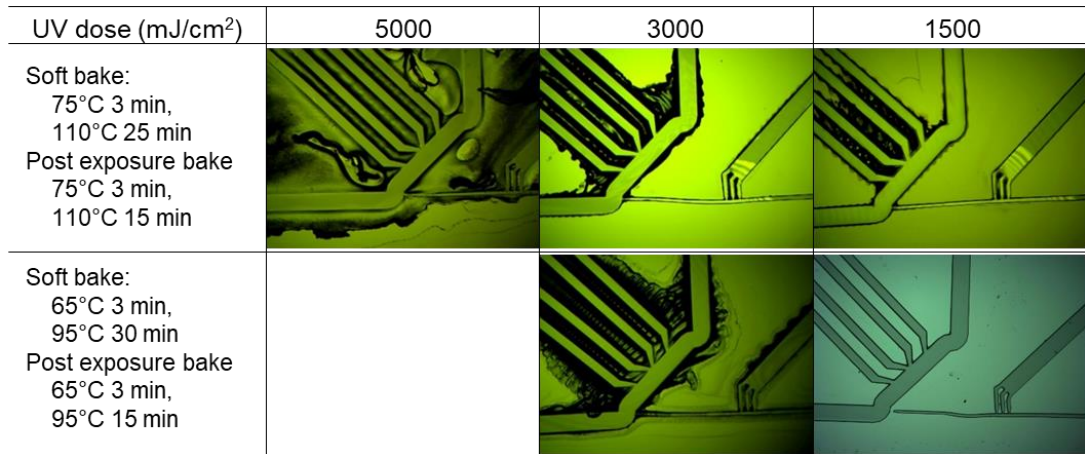


**Figure 3.18** Stimulus redirection. The direction of the stimulus (fluorescein) can be altered toward or against the amphid of the trapped worm.

### 3.2.7 Master fabrication for side view device

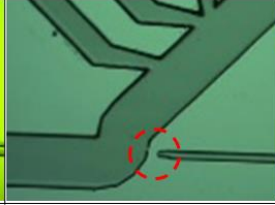
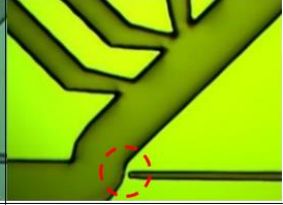
We attempted to find out a condition of master fabrication. The master was fabricated with patterned photoresist on a silicon wafer by rapid prototyping. SU-8 photoresist is an epoxy-based negative photoresist whereby the

exposed pattern to UV became cross-linked during post expose bake. The unexposed part remained soluble and washed away at the development step. The conditions of the soft bake, UV-exposure, and post-exposure bake were investigated in order to obtain the precise and firmly attached pattern. The UV-exposure was tested in the range between 1,500 and 5,000 mJ/cm<sup>2</sup>. Then, two sets of the baking temperature (75°C/110°C and 65°C/95°C) was examined. As a result, a higher dose of UV light and high temperature of the baking contributed to the strong bind of the pattern, but it formed a large residue around the pattern (**figure 3.19**). A clear pattern remained at UV dose 1,500 mJ/cm<sup>2</sup> and the baking temperature was 65°C/95°C. However, it was found that a narrow orifice (24 μm wide) was washed out while developing in this condition. It might be because the cross-linking at the UV-exposed pattern was not enough.



**Figure 3.19** Master image dependent on UV dose and baking time.

Then, we changed the length of the post-exposure bake to see how the post-exposure bake affected the pattern. We found post-exposure bake affects the solubility of the pattern and residue in the condition of exposure of 1500 mJ/cm<sup>2</sup> (**figure 3.20**). Long PEB (30 min) retained the residue, which was washable on 6 min of developing. However, in 2 out of 6 devices, the tips of the traps were disconnected when developing. In the case of short baking (15 minutes and 8 minutes), the residue was removed within 3 min, but the traps were disconnected quickly.

Post exposure bake	65°C 3 min, 95°C 30 min	65°C 3 min, 95°C 15 min	65°C 3 min, 95°C 8 min
Soft bake: 65°C 3 min, 95°C 30 min UV exposure: 1500 mJ/cm <sup>2</sup>			

**Figure 3.20** Master image dependent on the length of post-exposure bake. The tip of the trap was disconnected when developing (red dotted circle).

There is an issue that the produced patterns were easily lifted off when moulding the PDMS device. The adsorption between the photoresist pattern and the silicon wafer was not strong enough. The detachment of the pattern occurred mainly when the master was hard-baked and cooled down (**figure 3.21**)

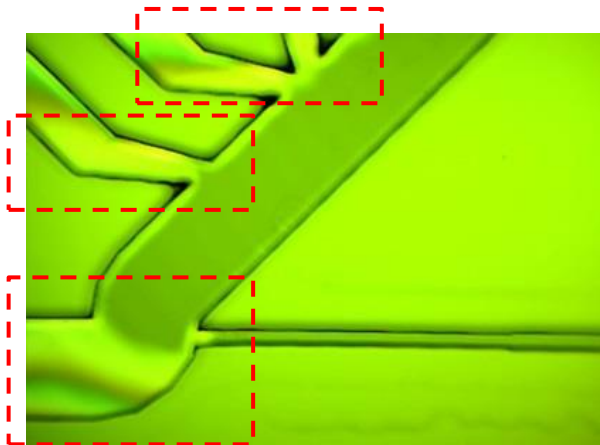


**Figure 3.21** SU-8 photoresist pattern partially detached from the silicon wafer (bright area in red dotted boxes).

The purpose of the hard-bake step is to remove cracks on the pattern after the developing. So, we examined all the photoresist patterns of the master by a microscope, whether there were visible cracks or not. Then, we removed the baking step when the cracks were negligible.

Then, OmniCoat™, an adhesion enhancer, was tested. It was spun on the silicon wafer and baked before the spin coating of the photoresist. However, there was no or little improvement in the stability of the pattern. The resulted su-8 patterns still lifted off when moulding PDMS (**Figure 3.22**).

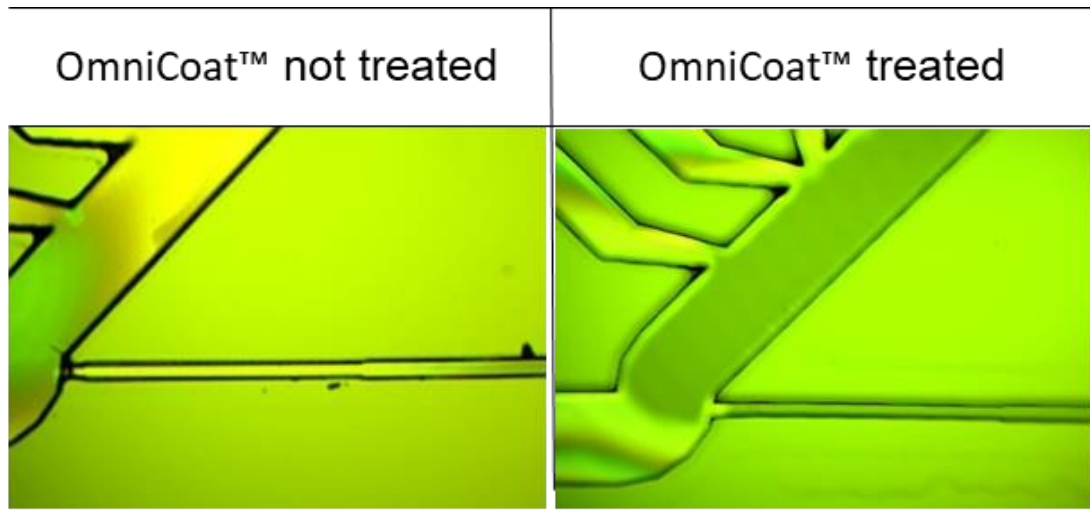


**Figure 3.22** OmniCoat™ treatment. The partial detachment of the pattern was improved but not completely solved.

The issue of the pattern lifting off was not completely solved. We assumed the rapid temperature change induces uncontrolled twisting of the pattern, and eventually, the pattern becomes vulnerable. So, we changed the current baking step into a ramping bake, which gradually increased the temperature to 55°C and decreased to room temperature. As a result, the fabricated patterns were strongly attached to the wafer enough to be used for more than five times of PDMS moulding (**Figure 3.23**).

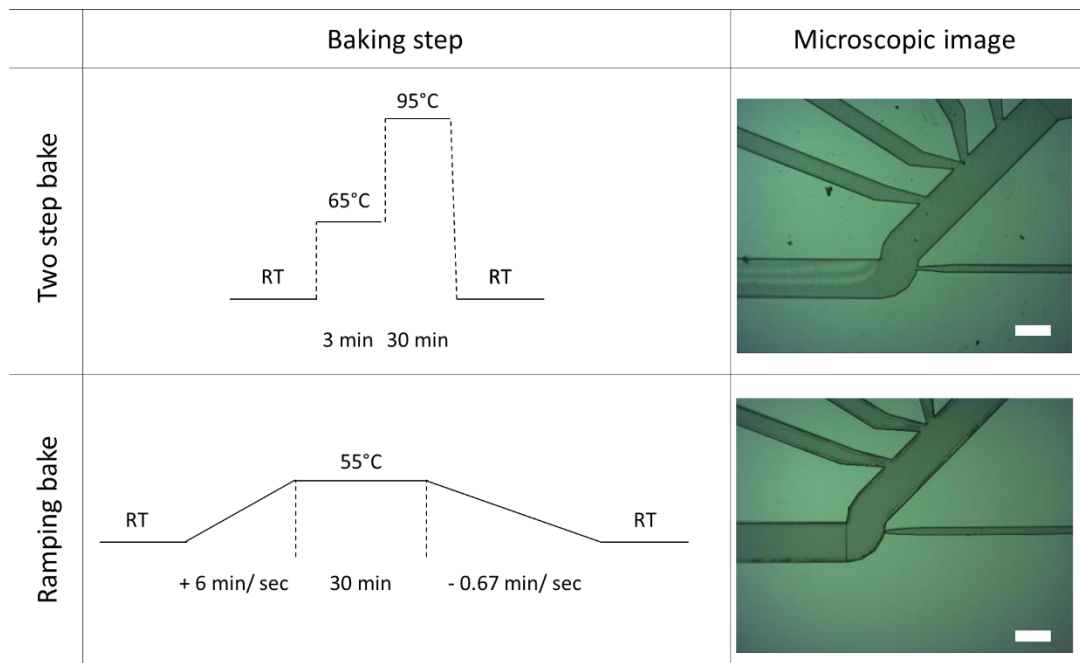


**Figure 3.23** Comparison of Two-step bake and Ramping bake. The gradual change of the temperature prevented the pattern from lifting off.

### 3.2.8 Fluorescence acquisition

The fluorescence of the neuron was obtained by customised software developed by Christopher Brittin. Even though the worm was immobilised, the neurons moved forward and backwards by the motion of stretching and shrinking. We tracked the neurons using an adaptive correlation filter to minimise the motion artefacts. At first, we set a rectangular ROI1 manually around the neurons for the correlation filter. We found that the motion of the neurons was greatly reduced.

The fluorescence was measured using the ROI1. To discriminate the region of the left neuron and right neuron, the summation of the vertical pixel array in the ROI1 was plotted and fitted as double Gaussian. Then, the vertical line penetrating in the middle between two peaks divided the ROI1 into left and right region. Then, each rectangle was divided into the regions of inside and outside of the trap. The fluorescence of the rectangles inside of the trap was defined as the signal fluorescence ( $F(\text{sig})$ ) and outside the background fluorescence ( $F(\text{bgr})$ ). (**figure 3.24**).

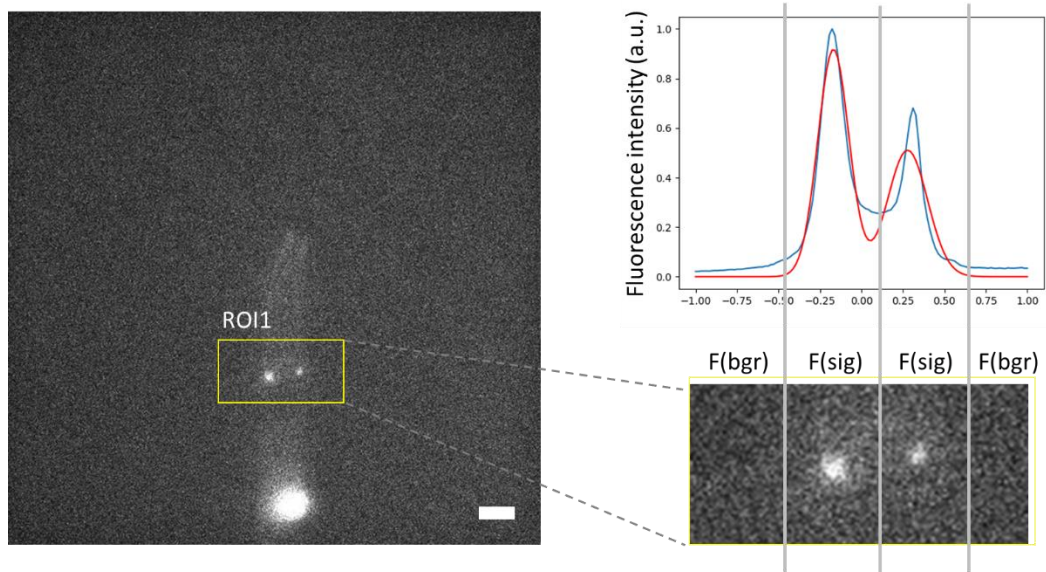


**Figure 3.24** The 1st method of ROI setting.

However, this method cannot discriminate the left and right neuron due to the anatomical feature of the neurons. The pair of the sensory neuron has axons which outspread to each other. The extended axons of the left neuron reach to the right half of the body and vice versa. When the neuron was responsive, the fluorescence in the axon extended from the soma was also increased (**figure 3.25**). The vertical separation was not able to discriminate the fluorescence between soma of one neuron and axon of the other.

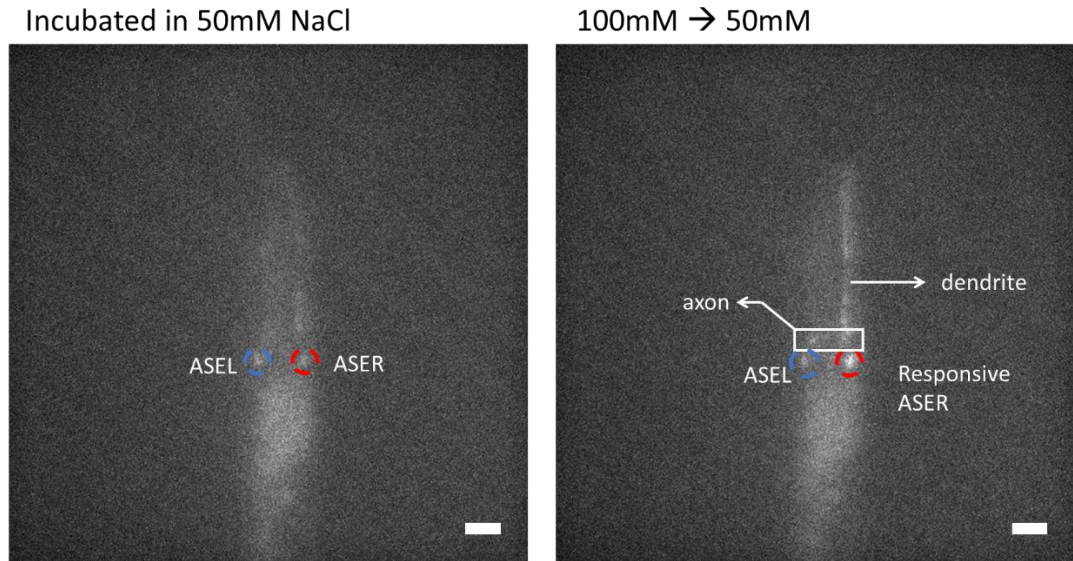


**Figure 3.25** Fluorescence of the axon extends to the other side. Bar indicates 20  $\mu\text{m}$ .

We set additional ROIs in the ROI1 to address the issue. We manually set rectangle ROI2L and ROI2R around the soma of the target neurons. Additionally, ROI3 was set around where the axons of the neuron were located. We defined the fluorescence in the ROI2L and ROI2R as the signal fluorescence  $S(\text{sig})$  and fluorescence outside the ROI2s and ROI3 but within ROI1 as the background fluorescence ( $F(\text{bgr})$ ) (**Figure 3.26**).

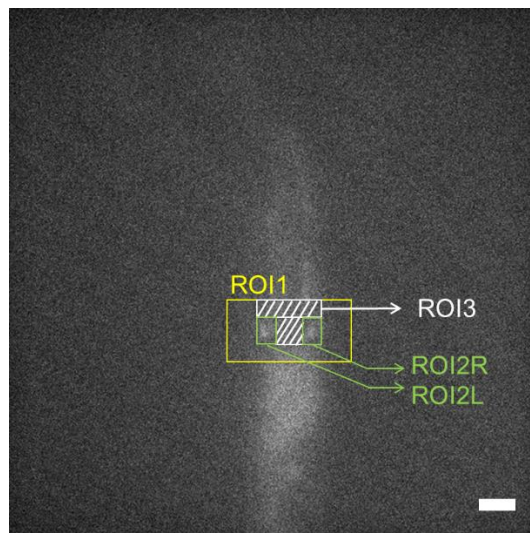


**Figure 3.26** The 2<sup>nd</sup> method of ROI setting. ROI3 removes the area where axons are located.

Correlation filter is known to be simple, fast and effective for tracking.[228] The MOSSE algorithm provides reliable performance for tracking neurons in our data. The fluorescence intensity of the neurons varies when the worm responds to the stimulus. The tracker can track neurons of varying intensity in the target cells. Additionally, this algorithm can be used to track multiple neurons in the same image.

### **3.3 Simultaneous measurement for the response of ASE neurons to the stimulus**

Despite their morphological similarity, ASE Left (ASEL) and ASE Right (ASER) neurons express different genes, follow different developmental programs and exhibit different physiological properties.[86, 113, 229] It is well known that both neurons mediate NaCl attraction.[83] However, whereas ASEL responds to increases in NaCl concentration, ASER responds to NaCl concentration decreases.[86] We tested the usability of the device by imaging GCaMP reporter activity of these well-studied neurons in response to step changes in NaCl concentrations.

To test the responses of animals to NaCl increases, worms were pre-exposed to 50 mM NaCl for 5 minutes, followed by 60 seconds 100 mM NaCl pulse. We observed that ASEL responded to the NaCl upstep while ASER responded to NaCl downstep at the end of the pulse (**figure 3.27a and b**) similarly to Suzuki *et al.*[86] The mean peak ASEL depolarising response was observed 9.8 seconds after the upstep, whereas ASER peak depolarising responses were observed 3.8 seconds after the downstep. We note that both ASEL and ASER responded to the stimulus only with a probability of about 80%, possibly indicating a stochastic response. All ASE neuron responses of individual worms are presented in **figure 3.27e** (upstep) **and 3.27f** (downstep). As shown in the raster plots, ASER was either hyperpolarised or non-responsive to the upstep of NaCl concentration, and ASEL exhibited no significant responses to the downstep.

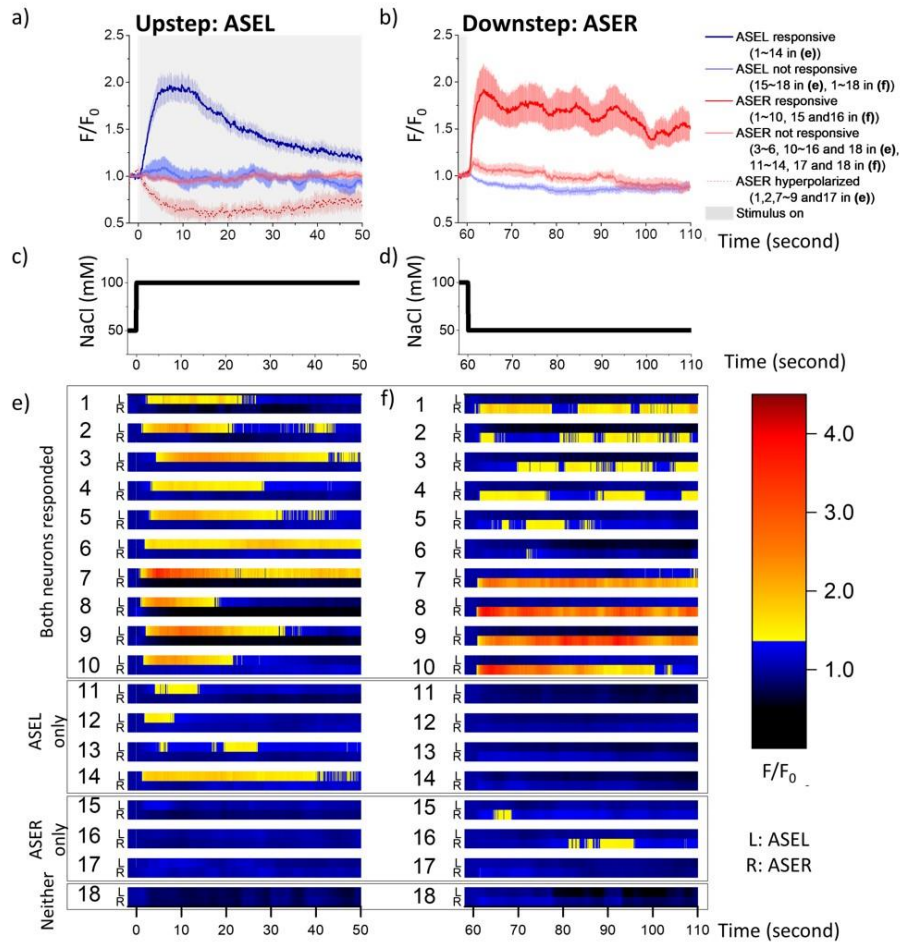


**Figure 3.27** Neuronal activity of ASEL and ASER in response to upstep and downstep of the NaCl concentration, between 50 mM and 100 mM for 120-second duration (a), (c) and (e) for the upstep, (b), (d) and (f) for the downstep. (a) (b) Ratiometric ASEL responds to upstep of the stimulus and ASER to downstep. 14 out of 18 ASEL were responsive to the upstep, and 13 out of 18 ASER did to the downstep. Also, 5 out of 18 ASER were hyperpolarised in the upstep. Both ASEL and ASER neurons were simultaneously imaged. Mean peak ASEL response was observed 9.8 seconds after the upstep ( $1.96 \pm 0.14$ ), whereas ASER 3.8 seconds after the downstep ( $1.97 \pm 0.29$ ). Mean peak ASER hyperpolarisation was observed 16.8 seconds after the upstep ( $0.60 \pm 0.06$ ). Error bars were calculated with  $\pm\sigma/\sqrt{n}$ , where  $\sigma$  is standard deviation and  $n$  is the number of the worms. (c), (d) A concentration profile of NaCl which was introduced to the amphid of an immobilised in the side-view device. The concentration of NaCl is changed from 50 mM to 100 mM and remains for 60 seconds. Then, subsequently, it is changed to 50 mM and remains for 60 seconds. (e), (f) Raster plots showed the simultaneously measured transient of ASEL and ASER from individual worms. ASEL and ASER respond to the stimulus stochastically.

### 3.4 Simultaneous measurement of the response of ASH neurons to the stimulus

The ASHL and ASHR neuron are considered as principal nociceptive sensory neurons in *C. elegans* and respond to osmotic, mechanical and chemical stimuli.[68] The neuronal activity of ASH responding to stimuli has been measured using the fluorescence of GCaMP, a calcium indicator).[56, 152, 174] Both ASHL and ASHR neurons depolarise in response to sodium chloride increases and these responses are typically assumed to be highly synchronised, supported by the direct gap junctional coupling between the two neurons. However, the synchronising effect of the gap junctions between ASH neurons has not been directly assessed.

To determine whether ASH neurons are functionally synchronised or not, we used our side view device to image the calcium transients of ASH neurons in response to different NaCl concentrations (100, 200, 300 and 500 mM). We measured the propensity and amplitude of responses as a function of the concentrations of the NaCl stimulus. As expected, all worms showed a robust and synchronous response to 500 mM NaCl, and none responded to 0 mM (control) or 100 mM NaCl steps (**figure 3.28c and e**). Worms responded stochastically to steps of intermediate concentrations with 62% and 75% of worms responding to 200 and 300 mM, respectively (**figure 3.28c and e**). The average peak intensity of responding neurons also increased as a function of the applied NaCl concentration (**figure 3.28a and d**). There were no significant differences in the profiles of calcium transients between ASHL and ASHR (**figure 3.28a**).

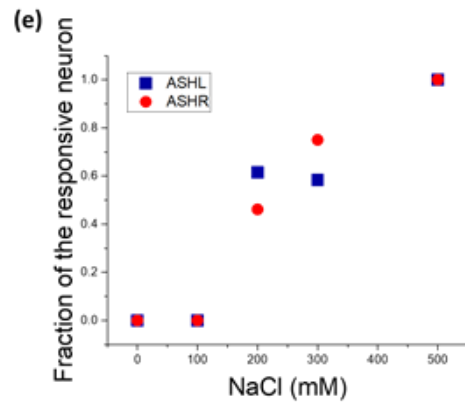
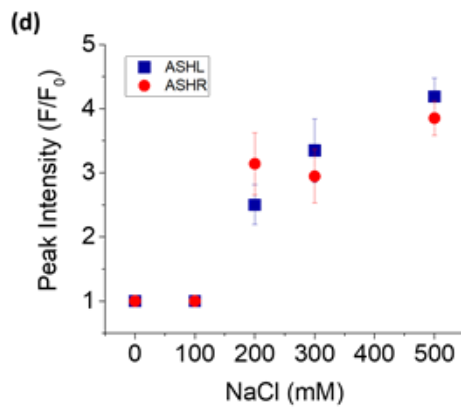
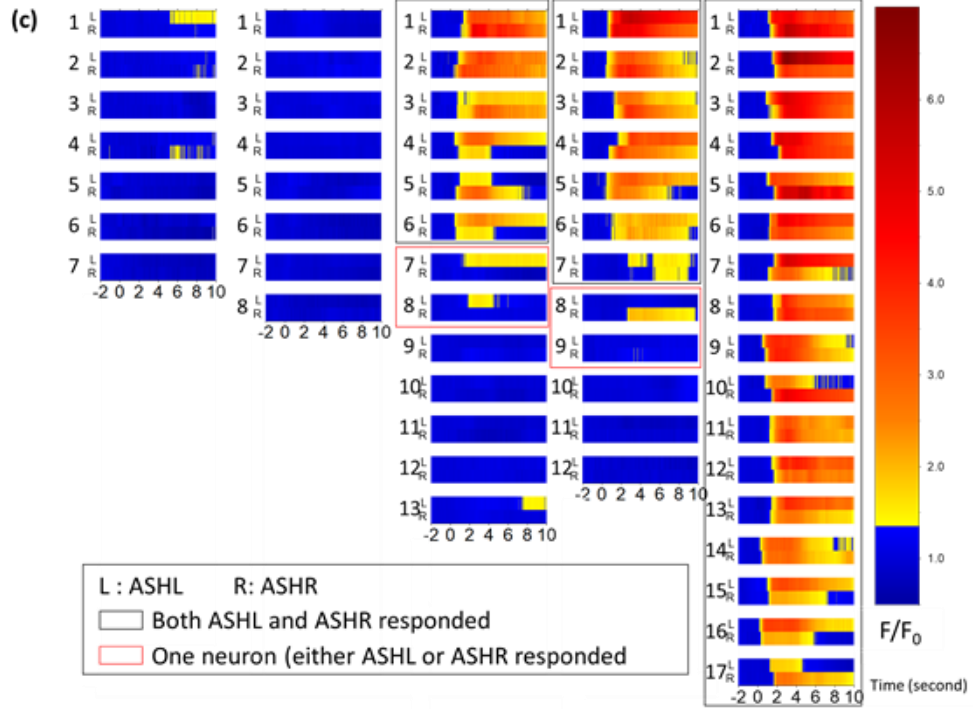
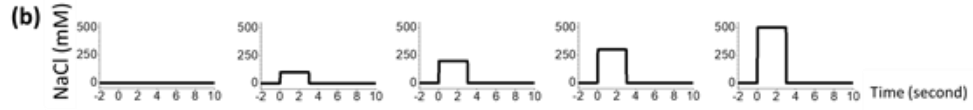
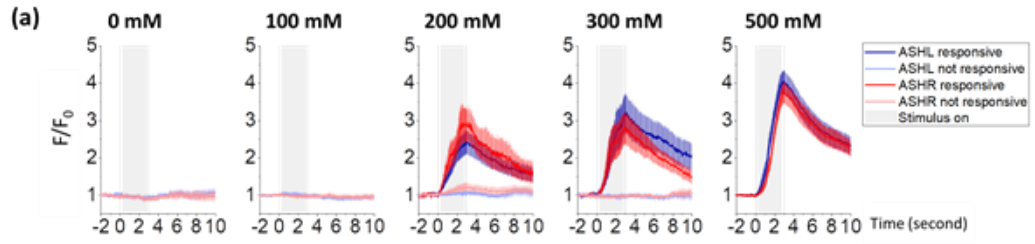


**Figure 3.28** Neuronal activity of ASHL and ASHR within *C. elegans* in response to a 3-second pulse of NaCl. Various concentrations of NaCl was exposed to the immobilised worms to find out the concentration range in which the worm shows a stochastic response. (a). The averaged traces of ASH response to a range of NaCl concentrations (0, 100, 200, 300 and 500 mM). The grey area and profiles in (b) represent the pulses of stimuli applied to the worms. The fluorescence signals in the neuron instantly increase when the stimulus pulse starts, and instantly decrease when the pulse stops. There was no significant difference between the average intensity of ASHL and ASHR. (Error bar  $\pm \sigma/\sqrt{n}$ , where  $\sigma$  is standard deviation and  $n$  is the number of the worm). (c). Fluorescence intensities observed from individual worms. ASH responds stochastically to 200 and 300 mM of NaCl concentrations; 62 % for 200 mM and 67 % for 300 mM. As shown in (d) and (e), the peak intensity and the fraction of the responsive neuron increased as a function of NaCl concentrations.

### 3.4.1 Cross-Correlation between ASHL and ASHR

We computed cross-correlation between the series of ASHL and ASHR. If both neurons responded to the stimulus which reached the amphid at the same time, but depolarisation of one neuron occurs behind the other's, it might be because the information from one neuron transmitted to the other and the transmission takes longer than direct response by the sensing. So, we computed cross-correlation between responsive ASHL and ASHR in the same worm. Though cross-correlation is a good practice for comparing the time series data with a repeating pattern and our data is a single transient, the analysis can provide us the lag time between the responses of bilateral neurons. Cross-correlation was computed as

$$r_{xy}(k) = g_{xy}(k) / \sqrt{[g_{xx}(0)g_{yy}(0)]} \quad \text{Equation (3.1)[230]}$$

, where

$$x=\text{ASHL}, y=\text{ASHR}$$

$$g_{xx}(0) = n^{-1} \sum_{t=1}^n (x_t - \bar{x})^2, \quad g_{yy}(0) = n^{-1} \sum_{t=1}^n (y_t - \bar{y})^2$$

, and

$$g_{xy}(k) = \begin{cases} n^{-1} \sum_{t=k+1}^n (x_t - \bar{x})(y_{t-k} - \bar{y}), & k \geq 0 \\ n^{-1} \sum_{t=1}^{n+k} (x_t - \bar{x})(y_{t-k} - \bar{y}), & k < 0 \end{cases}$$

.We found there was no significant difference in the lag time (**figure 3.29**). In all concentration of 200, 300 and 500 mM, the lag time was near 0 seconds. We found that our data are not sufficient to compute the correlation analysis. The lag time in 500 mM, where we assume that all the neurons are straightforwardly responsive, distributed with a standard deviation of 0.28 second. The distribution of the lag time in 300 mM was broader than the others. There was one worm in 300 mM that absolute value of the lag time is more than 1 second.

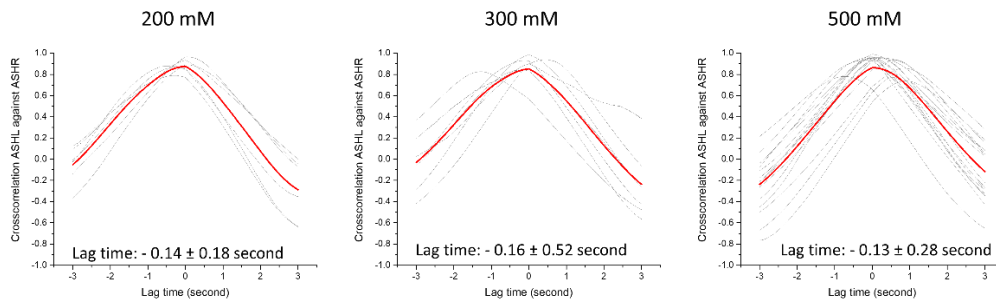


**Figure 3.29** Cross-correlation of the responsive ASHL and ASHR. There is no significant differences among the concentrations.

### 3.4.2 Independence test between ASH left and right neurons

Then we computed statistical analysis for independence between ASH left and right. When the neuron responses to the stimulus stochastically, each left and right neuron responses in some possibility following binomial distribution. The pair of the response of the worm would follow the probability simply calculatable from single neurons if both neurons are independent. We could compute Chi-squared test[231, 232], but the number of the sample was too small to obtain enough significance (13 worms for 200 mM and 12 for 300 mM NaCl). Instead, we can compute Fisher's Exact test. We evaluate all possible combinations of the 2 X 2 binary data (ASHL responsive/ not responsive versus ASHR responsive/ not responsive). We set the null hypothesis that there is no association between ASHL and ASHR excitation, and the probabilities of the ASHL and ASHR being responsive and not responsive are not influenced by each other. The probability of each case (P) was computed as

$$P = \frac{{}_{(a+c)}C_a \times {}_{(b+d)}C_b}{{}_{(a+b+c+d)}C_{(a+c)}} \quad (\text{Equation 3.2})[233]$$

, where a is defined as the frequency of both responsive, b ASHR only responsive, c ASHL only responsive, and d none of the responsive. In order

to show the dependency, we selected intermediate concentration where the neurons respond stochastically, the fraction of each neuron responsive is not 0 or 1. We found that the left and right neurons associated with each other. ( $p = 0.016$  for 200 mM and  $p$  value= 0.045 for 300 mM) (**figure 3.30**).

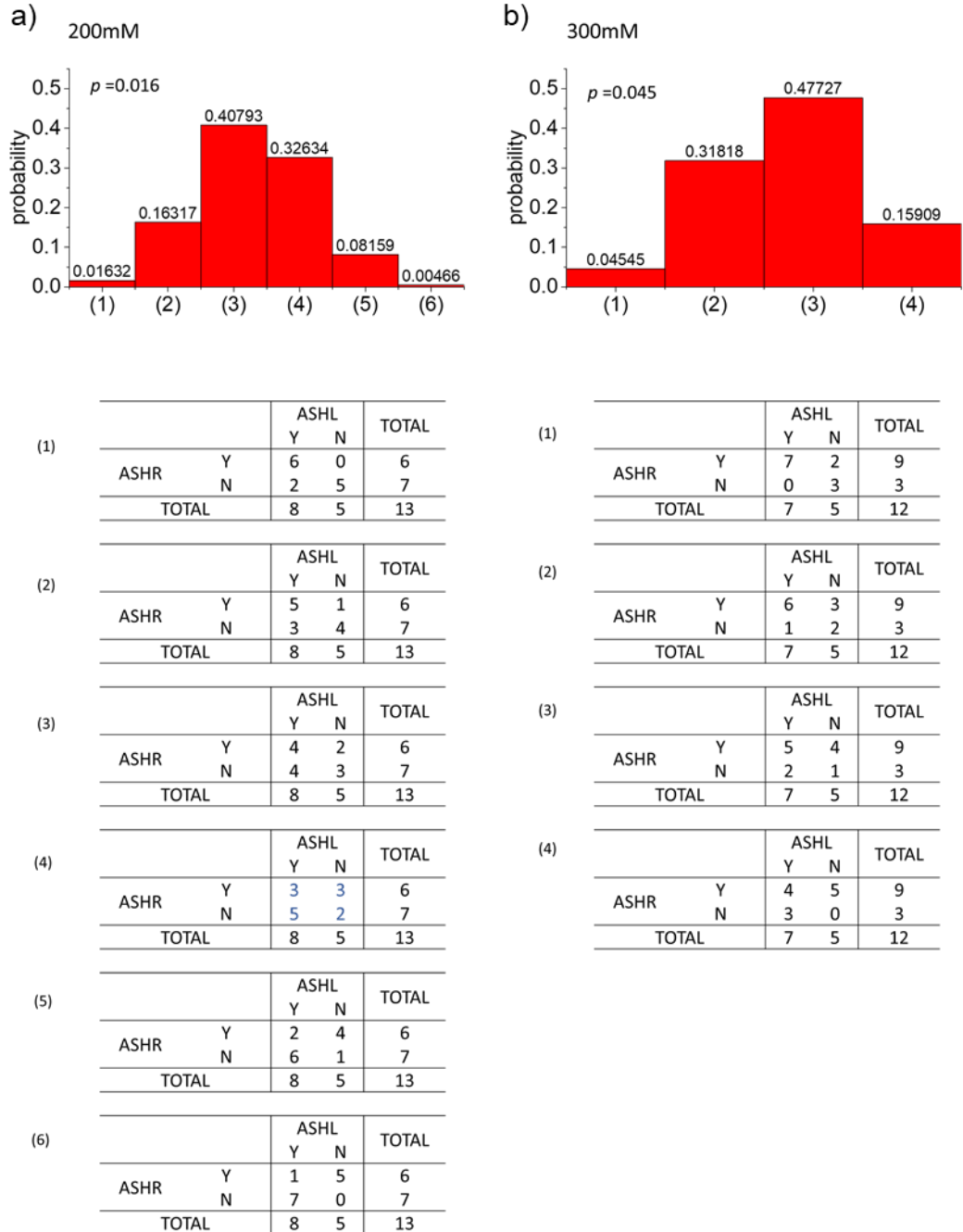


**Figure 3.30** Fisher's exact test. ASHL and ASHR excitation is associated with each other in both a) 200 mM ( $p = 0.016$ ) and b) 300 mM ( $p = 0.045$ ).

Additionally, to test for synchrony between left and right ASH neurons, we looked at the propensity of the two neurons to synchronise their responses. We set the null hypothesis that the left and right neurons respond to the

stimulus independently. Under the hypothesis, the joint probability of left and right neuron was calculated by multiplying the measured fraction of left and right neuron. Then, the probability of synchrony was computed as the summation of the probability of both or neither neurons were responsive

$$P = p_L p_R + (1 - p_L)(1 - p_R) \quad (\text{Equation 3.3})$$

, where  $p_L$  is the fraction of responsive left neuron and  $p_R$  right neuron). The standard deviation of  $P$  was calculated as

$$\sigma = \sqrt{nP(1 - P)} \quad (\text{Equation 3.4})$$

, where  $n$  is the number of the worm. Then, the measured fraction of the synchronous neuron pairs (both or neither left and/ nor right neuron were responsive) was compared with the probability of synchrony.

We found that the likelihood of both ASH neurons responding and both ASH neuron not responding was significantly higher than would be expected by chance (for independently responding neurons) in 200 and 300 mM of ASH (**figure 3.31**). The concentration of 0,100 and 500 mM, which all neurons are synchronous (both responsive or neither responsive), is supposed to have the value of 1 in the probability of synchrony and the fraction of the synchronous neuron pairs, and cannot determine the independence.

It was shown that the response of ASH left and right neuron are dependent in binary manner. Therefore, the pair of ASH neurons are functionally connected. Based on the result that the lag time between the left and right neurons are close to zero (**figure 3.30**). On the other hand, there was no significant evidence that ASEL and ASER neurons are interconnected with each other.

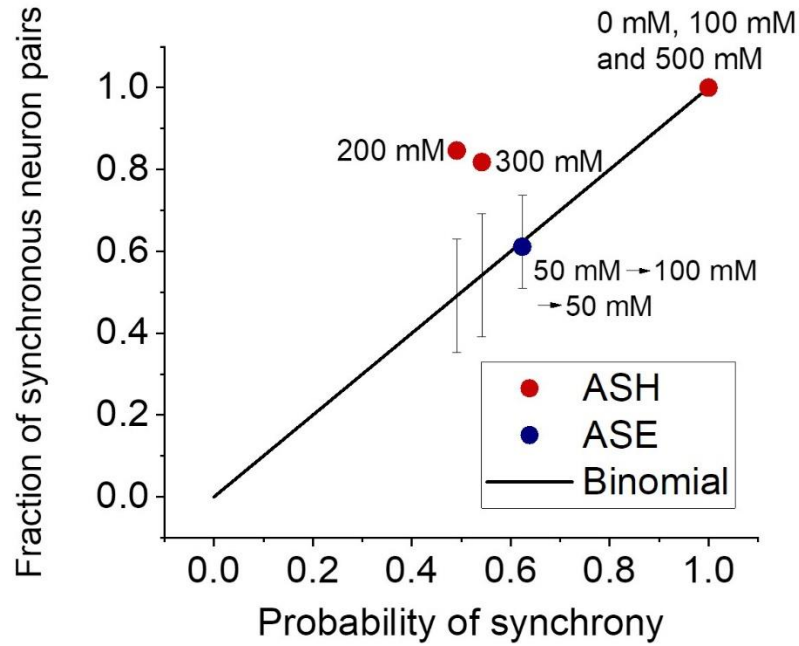


**Figure 3.31** The measured fraction of the synchronous neuron pairs compared with the calculated probability of synchrony. The fraction of synchronous neuron pairs was obtained by dividing the number of worms that are either both-neuron responsive or no-neuron responsive by the total number of assessed worms. Error bar is one standard deviation of the possibility of synchrony.

### 3.5 The role of the gap junction between ASHL and ASHR

It is known that gap junction, intercellular channel, allows direct transfer of small molecules and ions between coupled cells.[78] ASHL and ASHR are interconnected by gap junctions. There are 22 discovered innexins in *C. elegans*, but only INX-19 (also known as NSY-5) is expressed in ASH.[84] The *nsy-5* was also found in a screen for mutants deficient in *str-2* expression in AWC.

We assumed that this structure is responsible for the higher synchrony between ASH neurons. So we examined the ASH neuronal activity of a strain which is deficient in *str-2* expression and GCaMP in ASH neurons. The extrachromosomal array injection to CX6161 strain for expression of GCaMP in ASH was carried out by Christopher A. Brittin. The *inx-19* knocked-out worm was screened by GFP marker expressed in the coelomocytes. Also, the

GCaMP in the ASH neuron was selected by the base fluorescence of GCaMP in the neurons located near the pharynx.

As a result, a pair of fluorescence was seen in the side view, but it is behind the terminal bulb, where is approximately 20  $\mu\text{m}$  behind ASH neurons (**figure 3.32**). Normally, the pair of ASH sets in front of the terminal bulb. Furthermore, the success rate of the double mutant of *str-2* knock-out and GCaMP insertion was too low to continue the experiment; only one or two worms per generation were found in the screening.

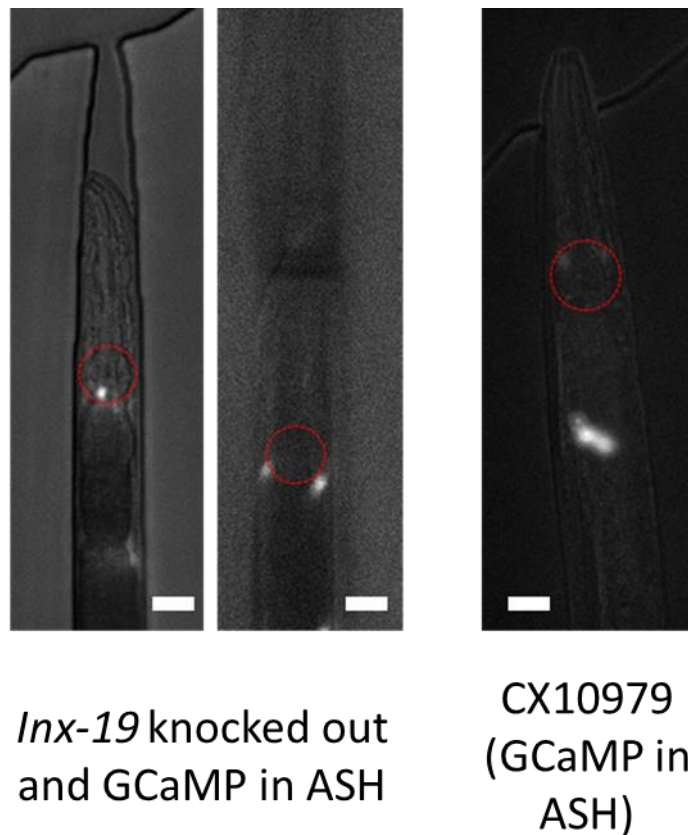


**Figure 3.32** *inx-19* knock-out strain. A pair of fluorescence was seen in the side view (middle), but it is behind the terminal bulb (red dotted circle) (left), where is approximately 20  $\mu\text{m}$  behind ASH neurons. ASH neurons were misplaced and not responsive to NaCl. The scale bars indicate 20  $\mu\text{m}$ .

### 3.6 Conclusion

This chapter describes a microfluidic approach that enables us to observe bilateral chemosensory neurons in *C. elegans* simultaneously. The rotatable side-view device allows for individual worms to be immobilised and imaged through the side of the device, thus simultaneously observing those cells

located in the lateral plane. We demonstrated the utility of the device by recording the responses of ASE and ASH neuron pairs in response to stepwise changes of NaCl concentration. We also present experimental evidence in support of the long-standing hypothesis that coupling between ASHL and ASHR synchronises their responses to noxious stimuli. Our approach does not require any potentially invasive ways such as applications of ultrasound or glues to manipulate or immobilise worms, which enables one to study relatively natural behaviours of worms in response to the application of stimuli. The prospective value of this approach lies in the capability of a microfluidic platform to immobilise a worm, control microenvironments, and observe their neural activity. This approach can be further developed to study the functional correlations of activities of sensory neurons, interneurons and motor neurons in conjunction with simultaneous observation of the animal's behaviour. Such experiments have the potential to reveal the detailed dynamics of entire neural circuits and relate them to behaviours in *C. elegans* at the cellular level.

## **Chapter 4**

### **Development of a microfluidic device for imaging head movement and neuronal activity of bilateral sensory neuron**

This chapter deals with the development of a microfluidic device to study how the pair of ASE neurons encode the head movement to establish chemotaxis behaviour to NaCl. The device aims to trap the worm with its head allowed to freely move around and treat the left to right gradation of the stimulus around the head of the worm. A reinforced trap for partial immobilisation of the nematode and a module for transposing the flow were developed. However, integration of the modules needs further consideration.

#### **4.1 Introduction**

The neuronal response of ASE neurons and the role of them in chemotaxis has been experimentally studied and its model has been established.[83, 86, 115] However, there is no known report of how both ASE neurons contribute when the nematode navigates. In **Chapter 4**, we attempted to develop a microfluidic device enabling characterisation of the chemosensory response of ASEL and ASER in half immobilised worms, while their head movement is allowed. Simultaneous imaging of the head movement and the activity of the bilateral neurons would provide us with insight into the process of neurocircuit to establish behaviour.

#### **4.2 Development of the wormhead device to image bilateral sensory neuron and the head movement**

##### **4.2.1 Multidepth channel fabrication using two PDMS blocks**

Oxygen plasma treatment for multilayer PDMS was used to construct a multi-depth channel or 3d directional channel in **Chapter 4**. Two masters were prepared for each layer of PDMS slab, and the bottom part was designed as a mirror image. The surfaces of the channel printed side were functionalised by oxygen plasma treatment and were irreversibly bound to each other. The alignment was carried out under the stereoscope (**figure 4.1**).

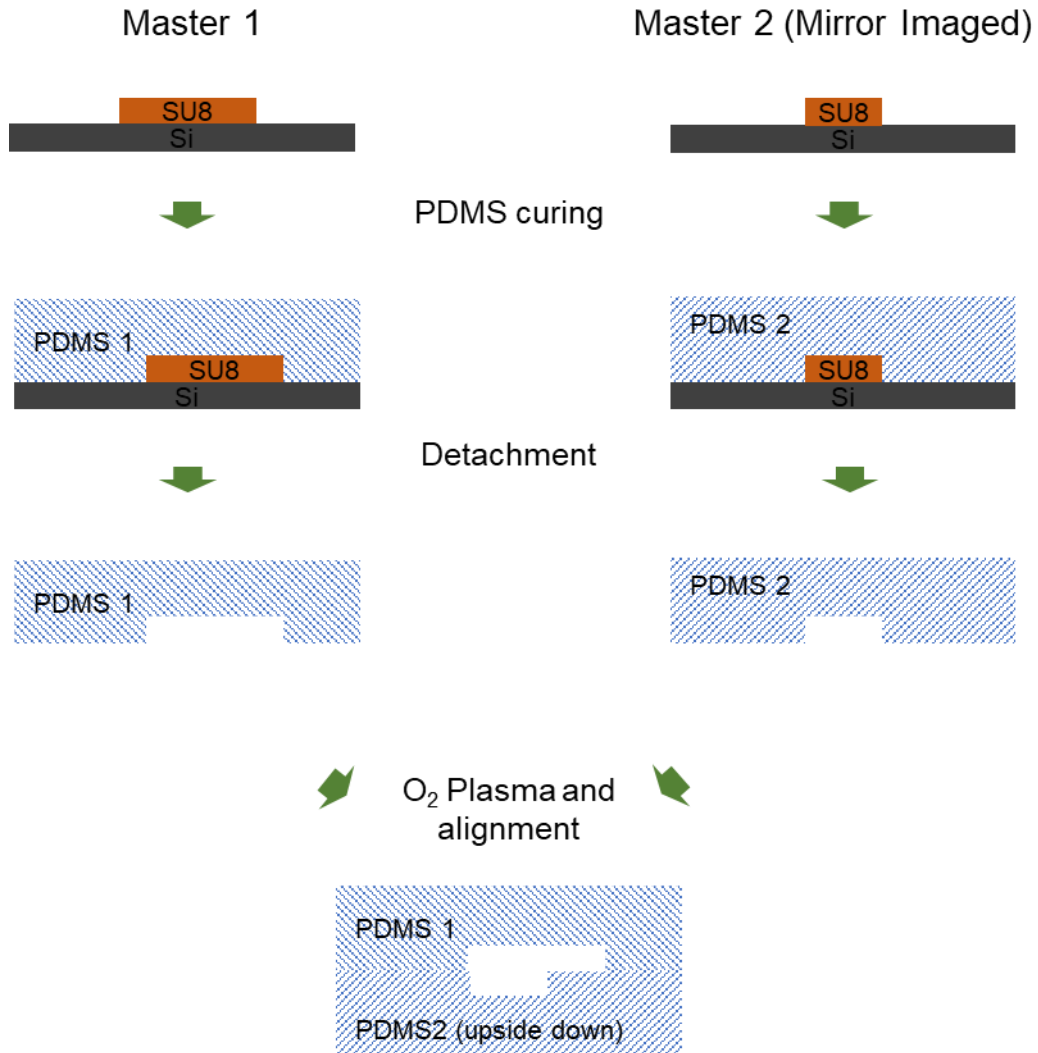


**Figure 4.1** Multilayer PDMS device fabrication for multiple depths of the channel. The bottom PDMS (PDMS2) is designed as a mirror image and bound to the top PDMS (PDMS1).

#### 4.2.2 Development of flow transposition module

We attempted to develop a device that enables imaging of the head movement and calcium response of ASE left and ASE right at the same time as supplying a graduating concentration of NaCl. We adapted and modified the side-view device in **Chapter 3**. We planned to supply a gradient of salt between left and right flow in the channel. The gradation formation along the x-y plane is widely generated using two laminar flows with different concentration of a molecule and letting it diffuse from high to low concentration flow, and adding a mixing unit if needed. However, the gradation of the concentration needs to be formed vertically in the side view device to provide a horizontal gradient to the worm, because the bilateral neurons are located

in the x-z plane in side view. To address this issue, we designed a device to transpose the flow.

We hypothesised that the flow would transpose to 90 degrees when the flow along x-axis turns twice, to z-axis and y-axis because fluid flows through the shortest way when it is laminar flow at a turn of the flow. To examine this, we fabricated PDMS devices, which has two 90° turns.

The master design of the flow transposing channel is shown in **figure 4.2**. The device was fabricated with two or three layers of PDMS slabs. So, the design of the top and the bottom layer was patterned on 340 µm thick SU8 photoresist. The top layer has a T shaped channel that has two inlets and one straight channel (350 µm wide and 340 µm high). Two different solutions were injected into each inlet so that the orientation of the flow was easily screened. The bottom slab was fabricated with a different master designed as a mirror image. Then, the channel-moulded side of the produced slabs was carefully aligned (the bottom slab was oriented upside down) and covalently bound by oxygen plasma treatment. The end of the channel in the top and bottom slab were aligned perpendicular. The thickness of the bottom trap was 1 mm, within the working distance of the microscope, and the cut side was smoothed to enhance the transparency as described in **Chapter 3**. The down channel in Layer 2 was made by punching the layer with a 0.4 mm diameter blunt needle. The length of the channel was set as 0 to 2 mm, by altering the thickness of the layer.

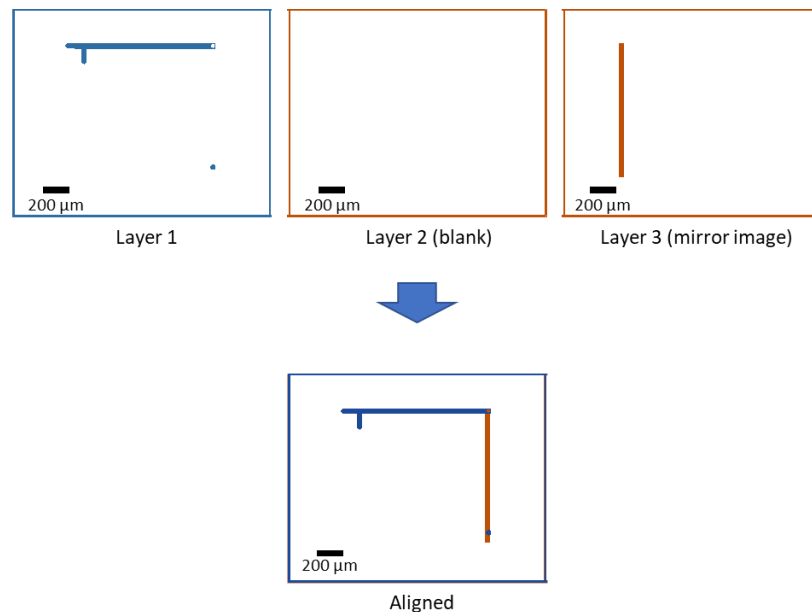


**Figure 4.2** Master design of the flow transposing channel.

Fluorescein (10  $\mu\text{M}$ ) and water flows were injected to the device through each inlet with the rate of  $2,000 \mu\text{m h}^{-1}$ . Then, the interface of the flow was imaged through the top and the side. As a result, we confirmed the interface forms between fluorescein flow and water flow on the x-y plane after two turns of the flow (**figure 4.3a, b and c**). The flow interface formed on the x-z plane in the top channel (1) flew down and turned left (2, 3). This interface turned 90 degrees and the interface formed on the x-y plane when the y-z plane was imaged as the side view (4 and 5).

Additionally, we tested the feasibility of the punch hole as the z-axis flow channel between the top and bottom channel. An additional PDMS device was added between two layers to control the length of the z-axis channel. We found the x-y interface still formed after 2 mm of the z-axis channel (**figure 4.4**).

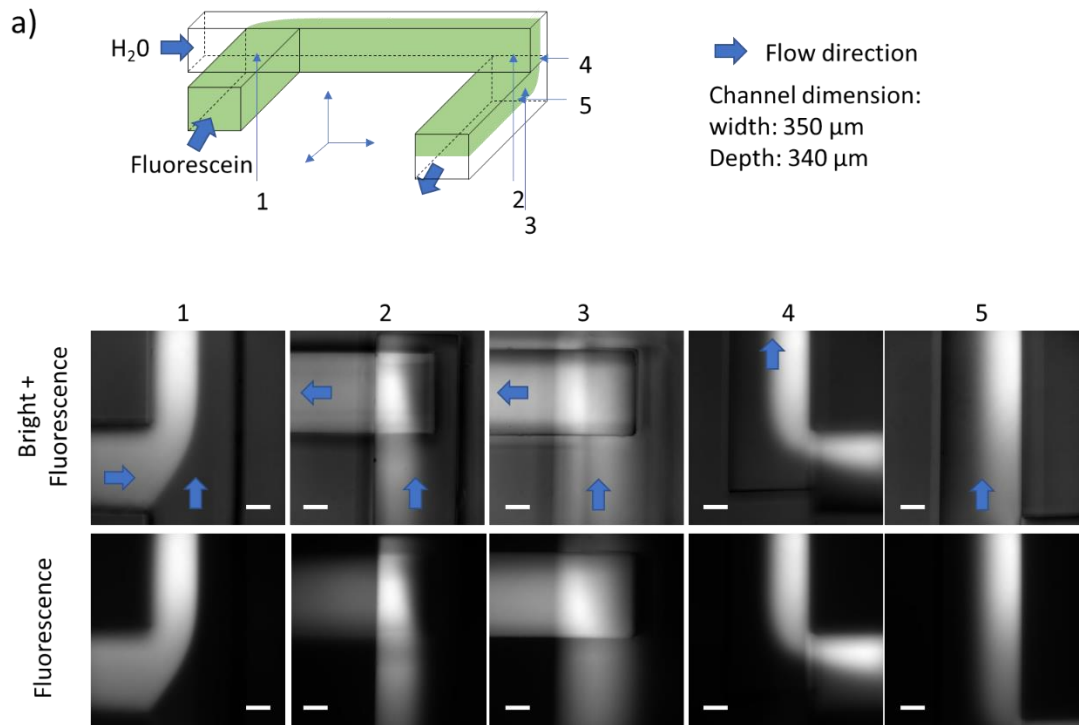


**Figure 4.3** Continued

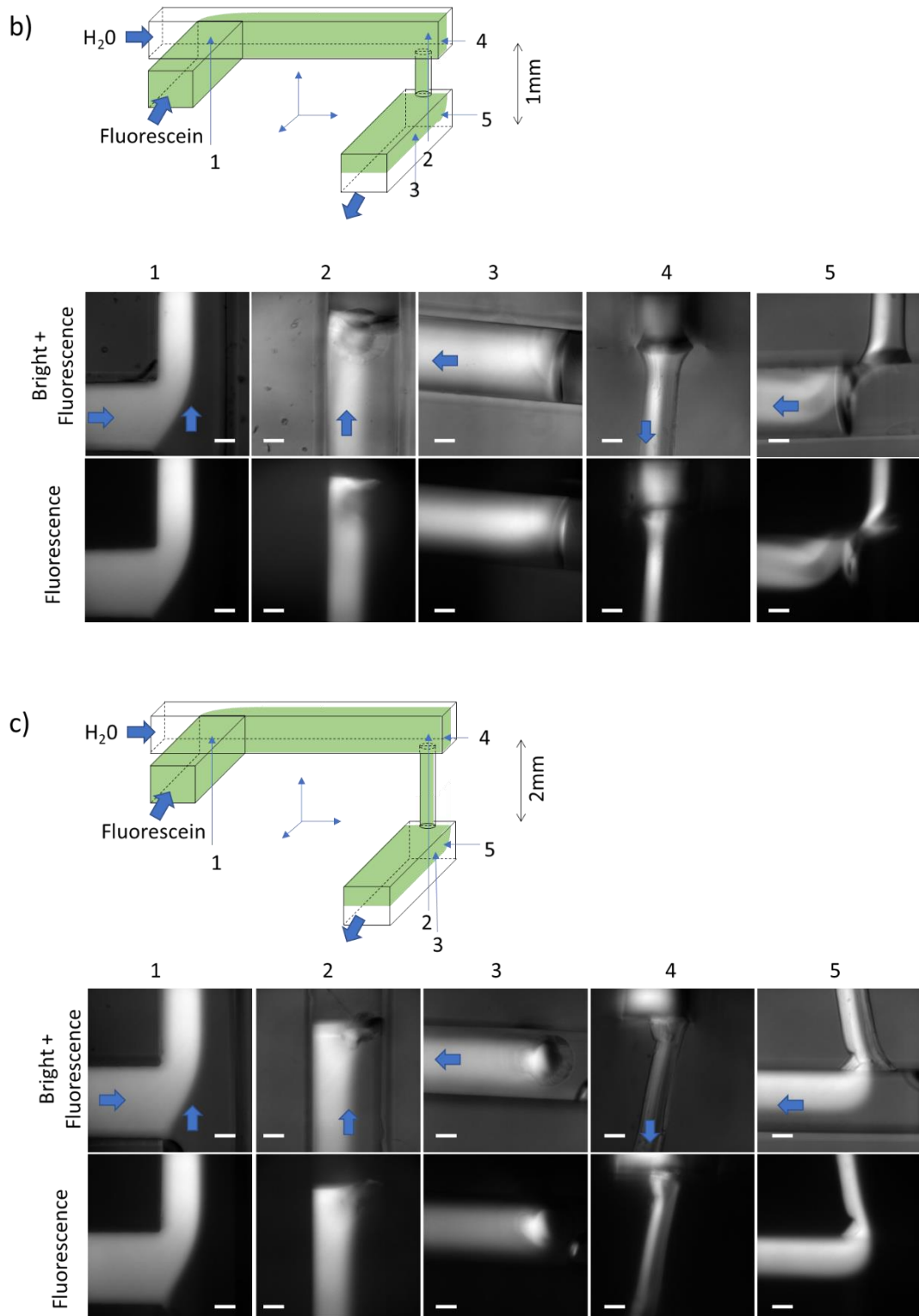


**Figure 4.3** Transposition of the flow. Two turns of the channel transposed the flow. The vertical interface formed in upper channel was transposed as horizontal interface in lower channel. Clear interface forms upto 2 mm of z-axis channel. The length of the z-axis channel: a) 0 mm; b) 1 mm c) 2 mm.

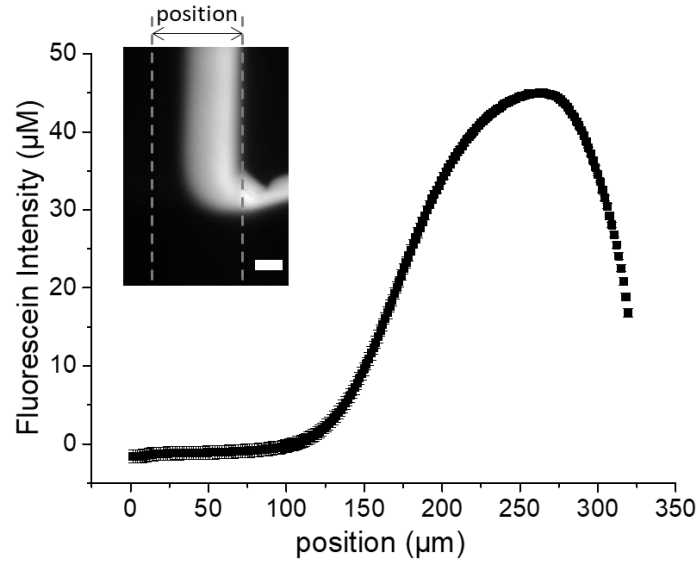


**Figure 4.4** Fluorescence intensity through z-axis of the channel after transposition. The vertical gradient is shown between the top and bottom of the channel. The interface between fluorescein and water flow was not clear due to the diffusion. This can be controlled by adjusting the length of the channels or adding a mixing unit.

#### 4.2.3 Design of the wormhead device

We designed a new device so-called a wormhead device. This device immobilises the worm with its head freely moving, enabling imaging of the response of the neuron and the head movement at the same time. It is developed to elucidate the correlation between the response of bilateral sensory neurons and dynamics of the worm movement, and eventually unveil the role of the bilateral neurons in the navigation of the body to favourable environment,

As both ASEL and ASER are known to be responsive to sodium chloride and known to respond in the opposite direction (ASEL responds to increase of the concentration and ASER to decrease) and contributes to the navigation, it is necessary to image both neurons simultaneously. So, we integrated additional modules to the side-view device, which enables imaging of bilateral neurons simultaneously, described in **Chapter 3**.

**Figure 4.5** illustrates the schematic design of the device. We attempted to develop a microfluidic device that partially immobilised the worm so that the forward-backwards movement was restrained, but the head movement remained free. The worm was delivered to the 35 µm wide X 35 µm high straight channel with its head protruding to the stimulus channel. However, once the head protrudes from the trap, the immobilised nematode escapes the trap easily. So, an additional air-pressure driven worm holding fork built

next to the trap helped to hold the body of the worm, stopping escape by undulating movement.

Then, the stimulus redirection module and additionally integrated transposing module supplies a vertical gradient (transposing module). As the worm is immobilised as its body lying on the side and the device operates as rotated to 90°, the gradient of the stimulus is needed to form vertically in order that the graduation of the concentration forms laterally (left to right of the worm head). (**figure 4.5a**).

Additionally, a space for the head of the worm to move was installed by widening the height of the channel around the head of the worm. We assumed that the bilateral sensory neurons of the half-immobilised worm responded to the stimulus and induced the movement of the head. Then, the location of the amphid was changed, and the worm senses the concentration where the amphid was located. The continuous loop of the sensing, transducing the information of the environment into the behaviour of movement eventually identifies the optimally favourable concentration.

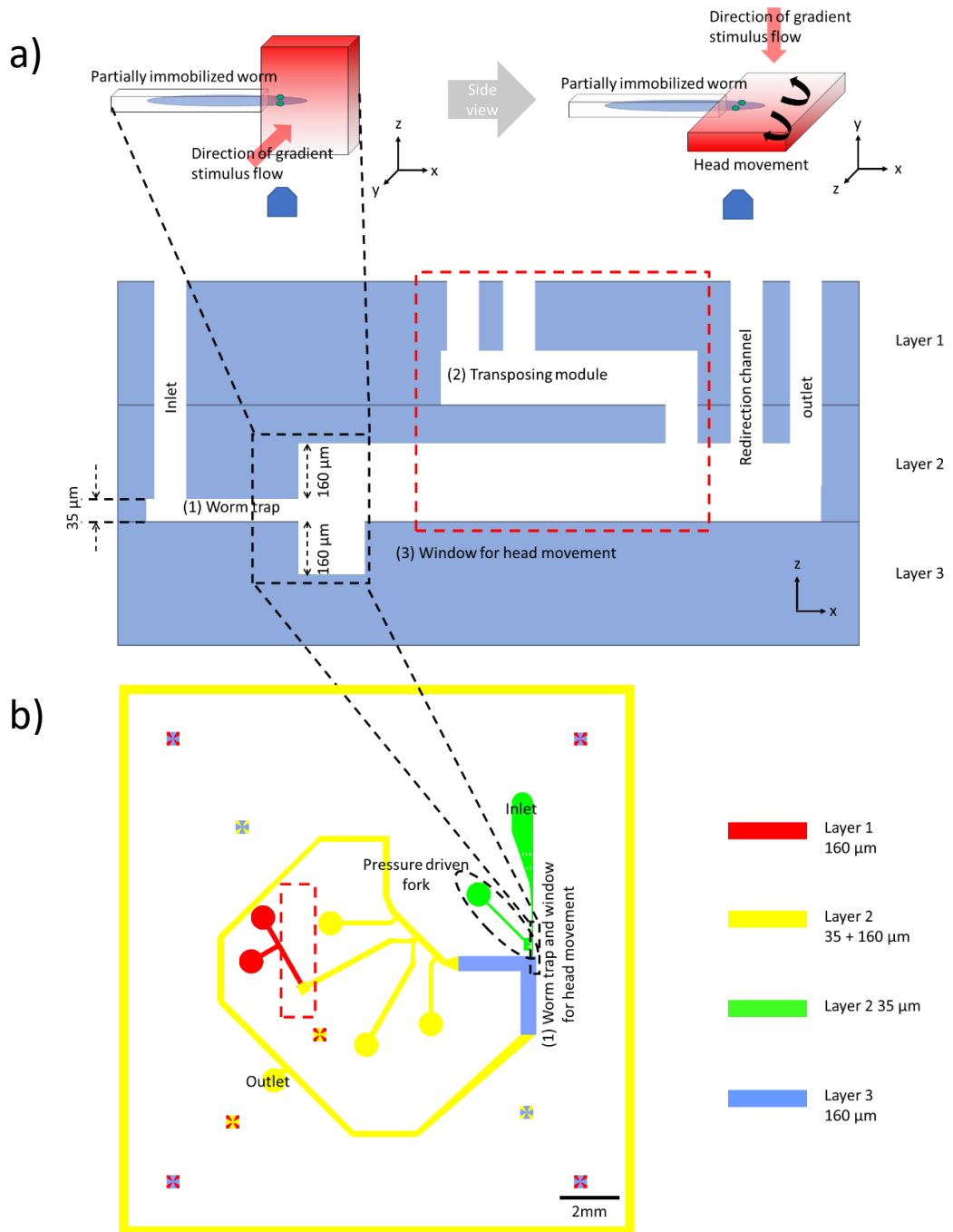


**Figure 4.5** a) Cross-sectional scheme of the device and the master design. The worm is immobilized in the trap (1). Stimulus flow turns 90° by transposing module (2). The space for the head movement is built by aligning an extra layer underneath layer 2 (3). b) Scheme of the device. The worm is partially immobilized and the entire head is protruded to the stimulus supplying channel. The stimulus with gradient concentration is delivered along the z-axis (left to right of the worm).

It is necessary to fabricate a multilayer master and PDMS device to achieve the trap with a wide vertical window and to integrate the transposing module. Three masters for each layer of 3-layered PDMS device was designed, and the detail is dealt with in **Chapter 4.2.4**.

#### **4.2.4 Master fabrication for the wormhead device**

The masters for the device were designed as shown in **figure 4.5b**. The device composes of three-layer PDMS slab, so three masters were fabricated for each layer. Layer 1 has two inlets merging into one straight channel. Two different concentration of the stimuli were injected to the inlets. Layer 1 is connected with the stimulus redirection channel on Layer 2 by a punch hole on the end of the channel. The design of the stimulus redirection module was adapted from the previous study. Layer 2 contains the 35  $\mu\text{m}$  high worm trap and 160  $\mu\text{m}$  high stimulus redirection module. An additional fork-shaped air-pressure driven worm immobiliser is set up next to the worm trap as the previous head shaped narrowing trap was replaced with a straight channel, which might allow the worm to escape the trap. Layer 3 is for space where the head of the worm can move in response to the concentration of the stimulus. The layer 3 is supposed to be aligned upside down so that it replaces the substrate. Each connecting area has the sharing region to minimise the risk in alignment.

Layer 2 was fabricated by double spinning to make either 35  $\mu\text{m}$  (the trap and the fork) or 160  $\mu\text{m}$  (flow redirection module) to achieve two different heights in one master. First, SU8-2025 was spun on the silicon wafer aiming for a 35  $\mu\text{m}$  thick photoresist. Then the wafer was moved to the thermoplate with the temperature ramping up from room temperature and incubated for 30 minutes after the temperature reaches 60°C. The temperature was ramped down to room temperature, which takes 1.5 hours. Then, UV was exposed to the photoresist corresponding to the design for the trap and fork using the direct laser writing system. Post-exposure bake followed the same process as the soft bake but incubated for 60 minutes on the plateau. Then, SU8-2075 was spun on the 1<sup>st</sup> photoresist. Then, soft bake on thermoplate and exposure as the design of the flow redirection module was carried out. Finally, the post-exposure bake and developing was followed.

As a result, the master of layer 1 and layer 3, which has mono-depth, was successively fabricated (**figure 4.6**). However, for layer 2, it was found that the worm trap was bent after the second soft-bake (**figure 4.7**). The 1<sup>st</sup> layer

was pushed after the post-exposure bake and second soft bake. It might be because the 1<sup>st</sup> layer of the photoresist was not solidified enough and spinning of viscous SU8-2075 would have pushed the pattern.

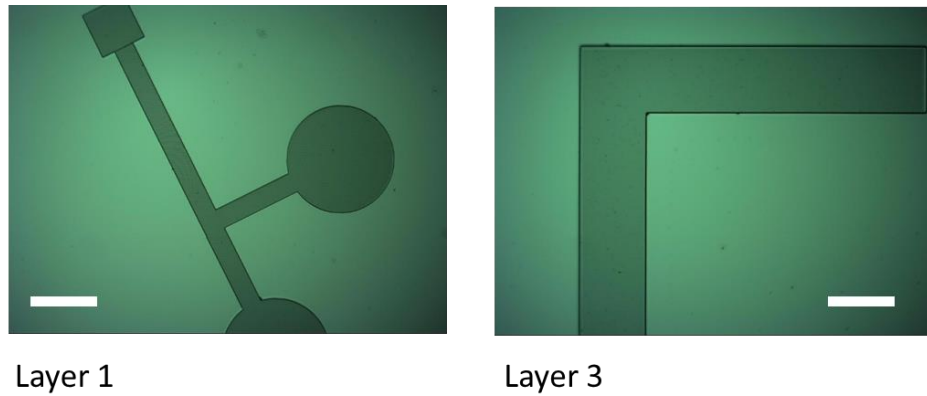


**Figure 4.6** Master for layer 1 and layer 3. It is aimed to achieve 160 $\mu\text{m}$  high. The scale bars indicate 500  $\mu\text{m}$ .

After the development step, it was found that the two layers were not aligned effectively because the exposed photoresist pattern of the bottom layer was pushed and moved at the second spinning for the top layer of the photoresist (**figure 4.7**). Hence, we proceeded to soft-lithography to produce the PDMS device with this master for collecting data for the next prototyping.

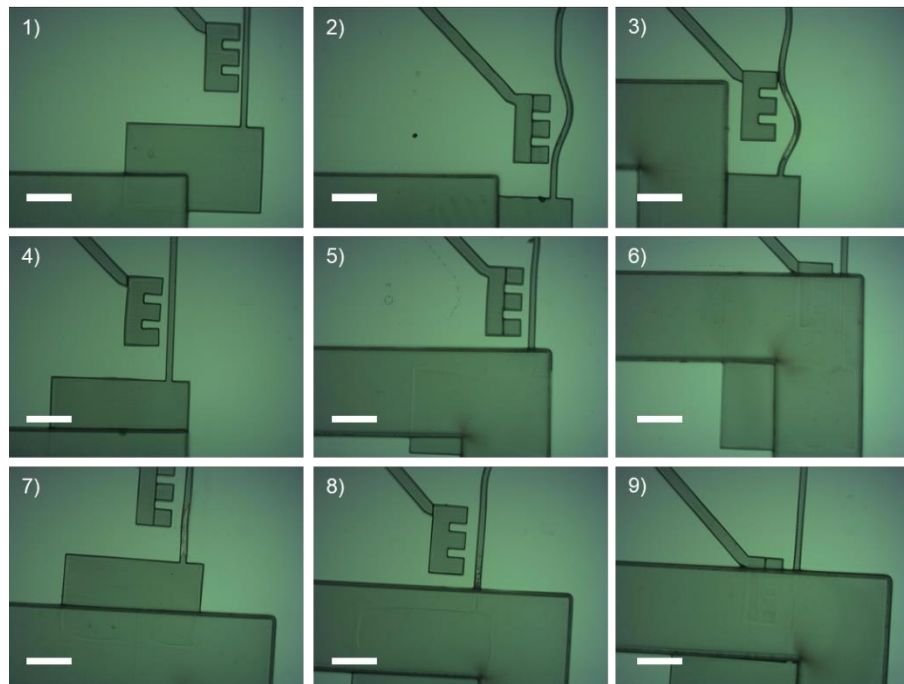


**Figure 4.7** Issue 1 in the multi-layer master fabrication (layer 2). 35  $\mu\text{m}$  pattern and 160  $\mu\text{m}$  pattern are not aligned. Device 1), 4), 5), 7), and 8) were sufficient to test the efficiency of the fork. Device #5 and 8) were usable to preliminary test for the flow. The scale bars indicate 200  $\mu\text{m}$ .

#### 4.2.5 Fork operation

We examined the trap and fork whether the straight trap could immobilise the worm efficiently. The worm was injected into the trap by syringe carefully so that approximately one-third of the body including the head and neck protruded to the flow redirection module. We found the worm was immobilised in the channel. However, the worm easily escaped the trap. So we added a fork-shaped worm holder (fork) next to the trap. The fork was operated by air pressure, and applied pressure pushed the PDMS membrane toward the trap. We examine the effect of the fork how far the membrane pushed into the trap. The width of the trap around the fork was measured with a range of pressures. **(figure 4.8)**. We found that the fork was able to endure pressure up to 45 psi. Leaking of the air occurred at 50 psi. The width of the trap was decrease when the pressure applied.

We compared the cross-sectional area of the trap in the condition that fork is operating with that of the orifice in the side view device. The side view device has 24  $\mu\text{m}$  wide and 40  $\mu\text{m}$  high, of which area is 960  $\mu\text{m}^2$ . To have the same area in the trap in the wormhead device, of which the height is 30  $\mu\text{m}$ , the width of the channel is needed to decrease to 32  $\mu\text{m}$  or smaller. This equivalent to 30 psi **(Figure 4.8)**. The worm was immobilised efficiently with this trap when above 30 psi of pressure was applied to the fork **(figure 4.9)**.

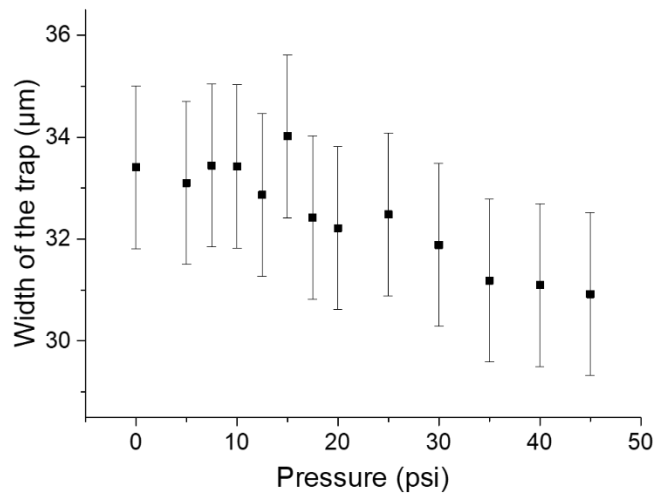
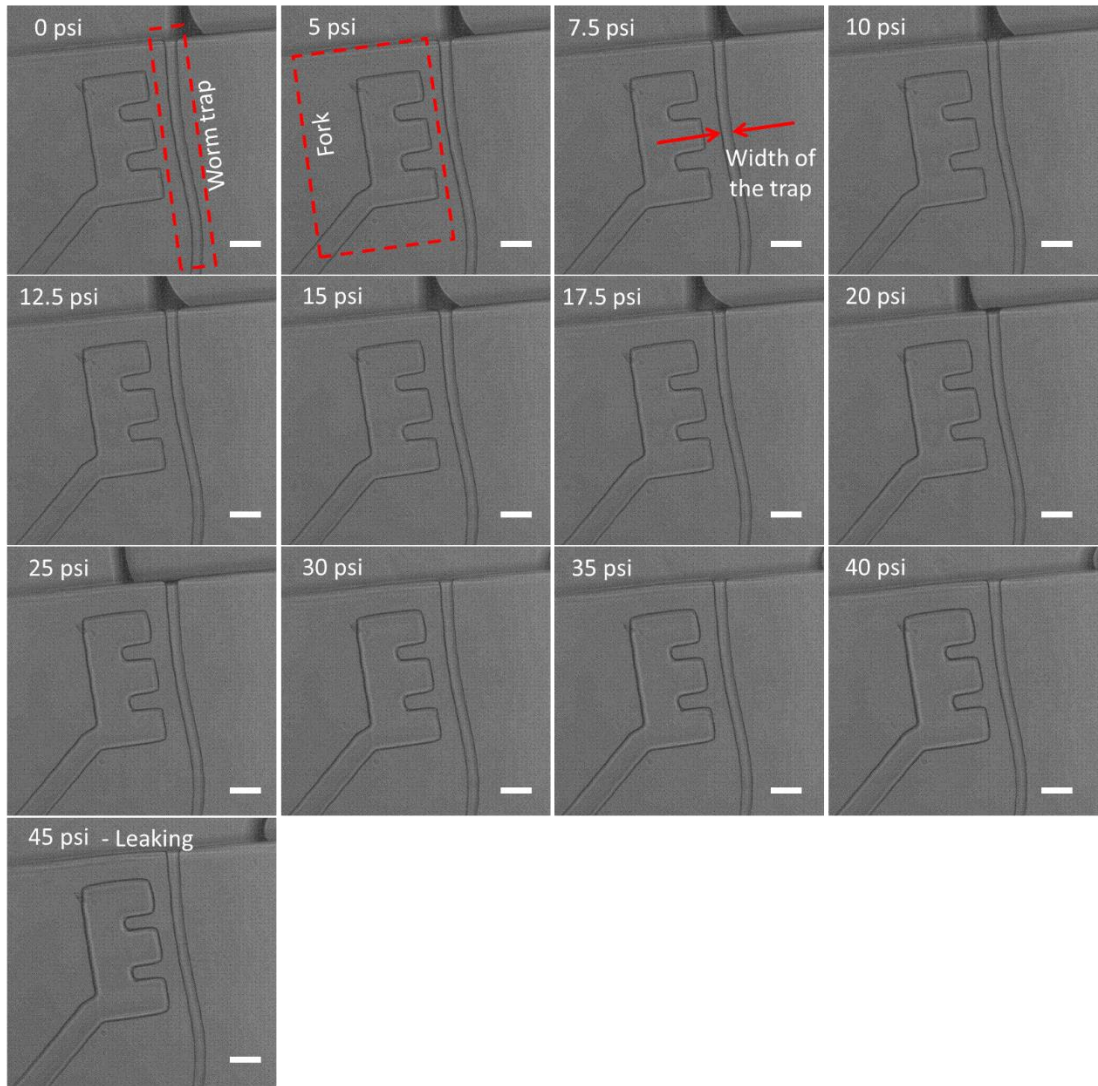


**Figure 4.8** Width of the trap depending on the applied pressure to the fork. Error bar is instrumental uncertainty.

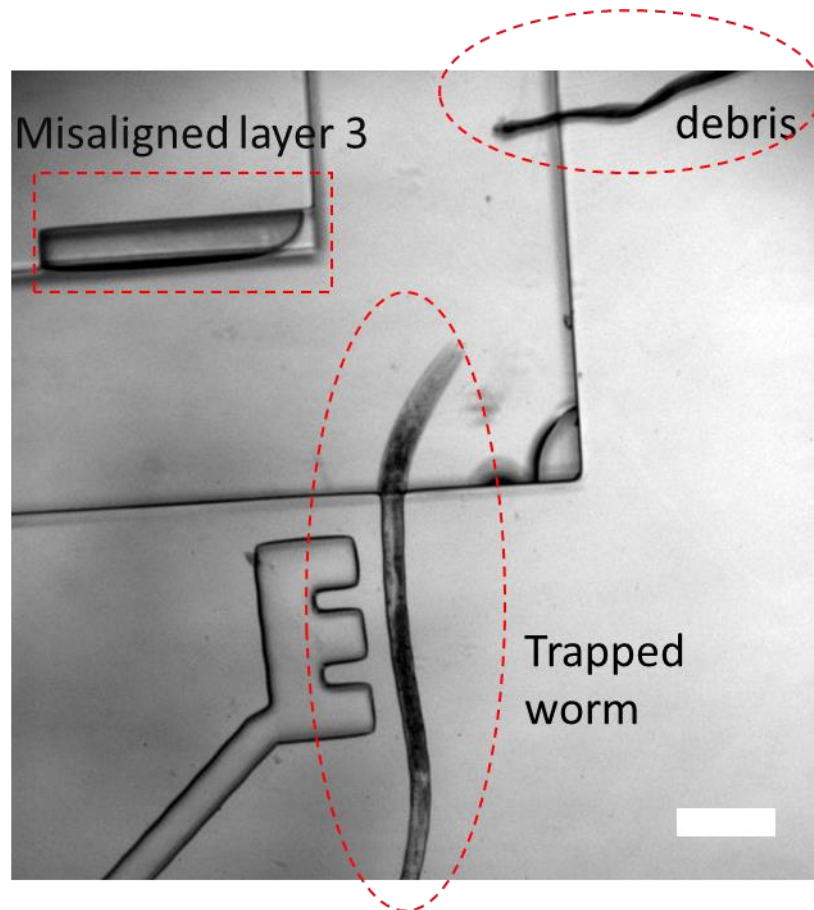


**Figure 4.9** The half-immobilised worm in the trap. Bar indicates 200  $\mu\text{m}$ .

#### 4.2.6 Flow test

We examined the flow redirection of the device. The device is operated by air pressure and redirection of the flow was performed by a solenoid valve out of the device. We examined a range of pressure to find the condition that the redirection is controllable. Pressure applied in (1) and (2) was set as identical to form the interface in the middle of the channel.

We found pressure less than 12 psi in 3-1 was not enough to block the stream (1) from leaking toward the worm trap (located on the right out of the image) at off condition. The redirection was achieved at and above 12 psi. However, we found that the fluorescence gradient was not controllable in this device. **(figure 4.10 and 4.11)**

We examined a simpler device, which has one depth of flow redirection module and a trap. This device was fabricated by bonding two layers of PDMS slabs. We integrated the flow transpose module to the side view device. There was a difference in dimension between the wormhead device (height X width

= 195  $\mu\text{m}$  X 360  $\mu\text{m}$ ) and the side view device (40  $\mu\text{m}$  X 100  $\mu\text{m}$ ). Hence, we performed the integration to investigate the complex structure such as the multiple depths for the movement screening module. We also found the uncontrolled orientation of the fluid in the device (**figure 4.12**)

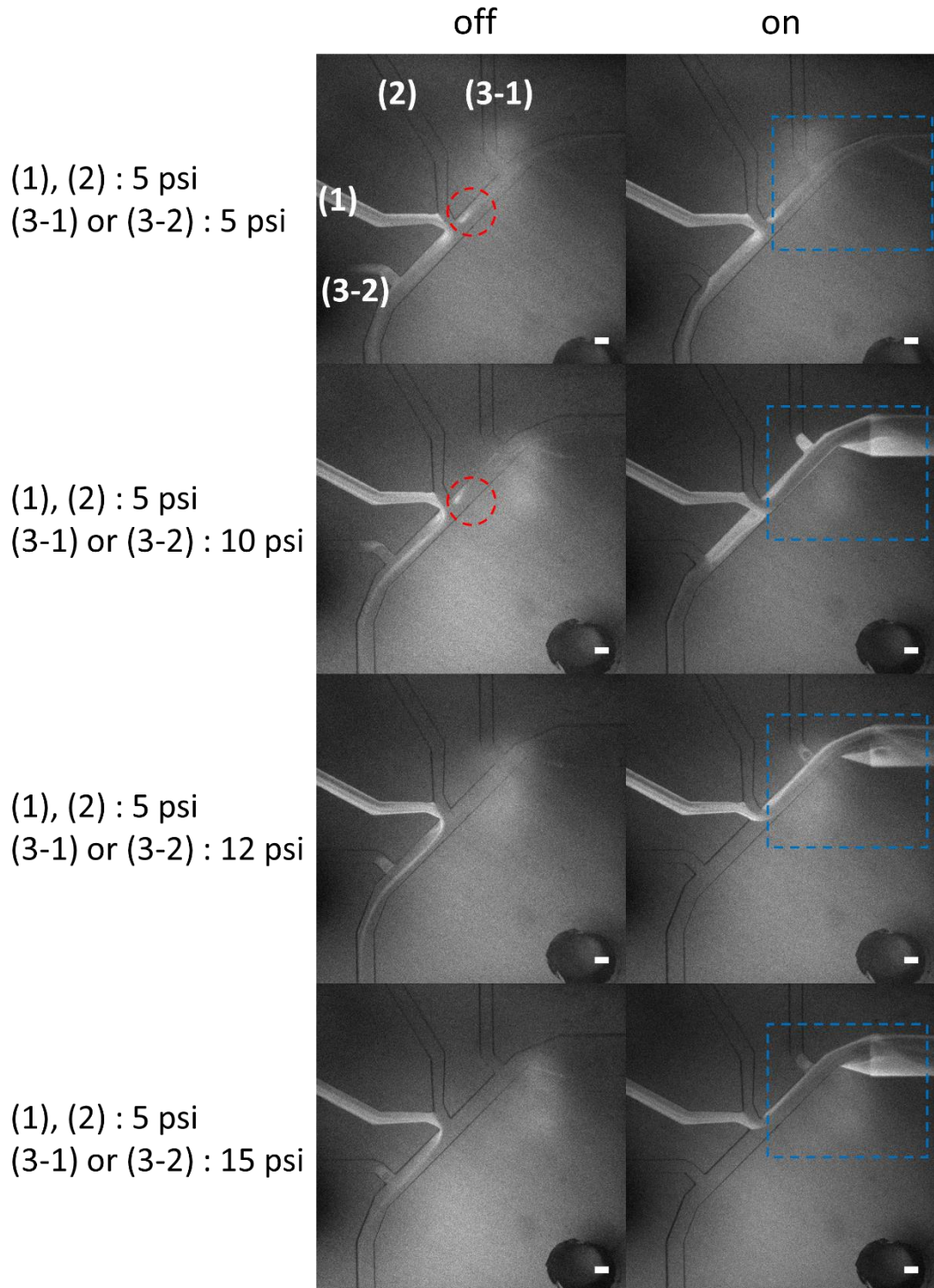


**Figure 4.10** Flow at the redirection module with the pressure of 5 psi in the supply flow ((1) and (2)). Uncontrollable interface formed (dotted area).

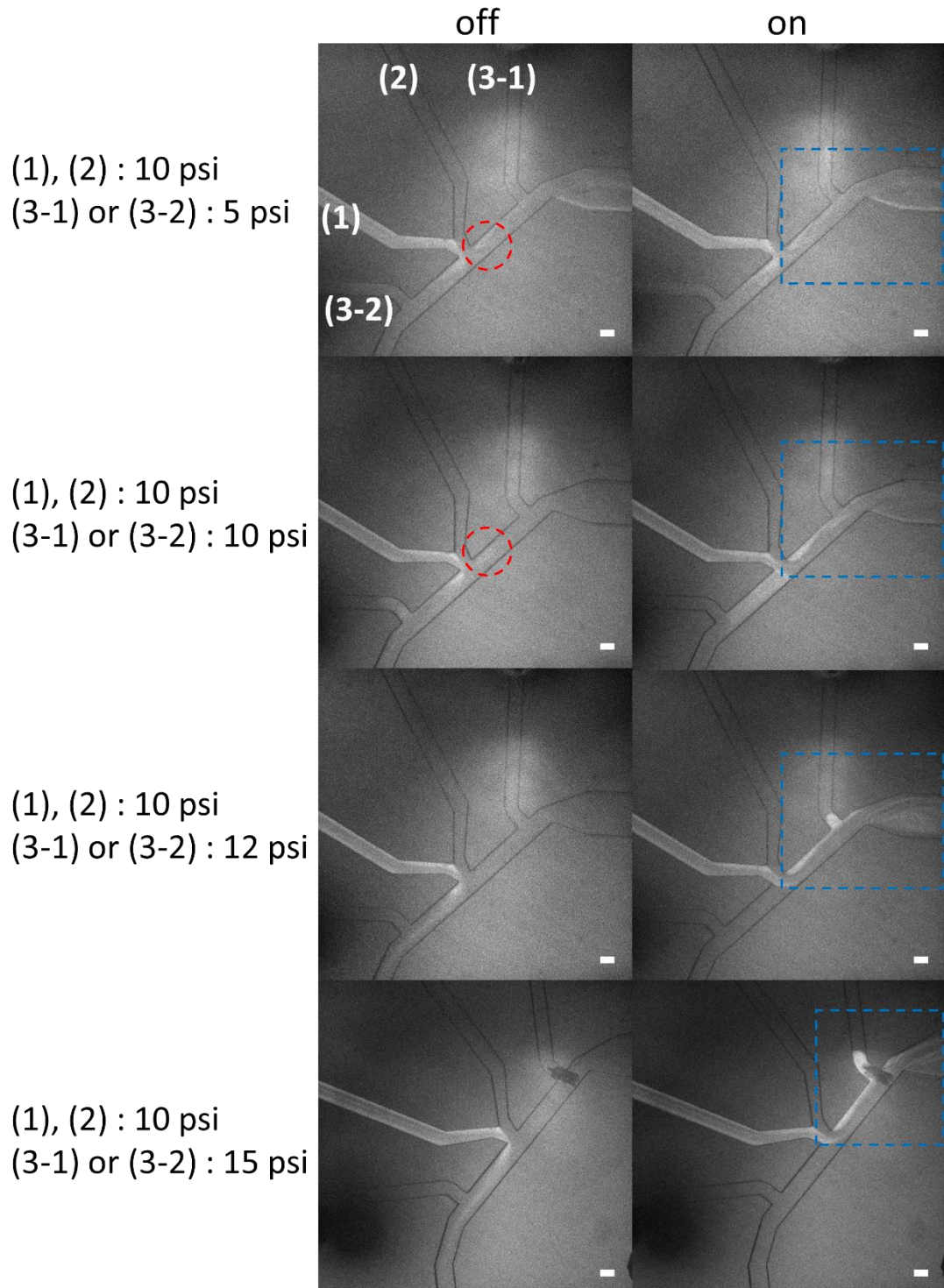


**Figure 4.11** Flow at the redirection module with the pressure of 10 psi in the supply flow ((1) and (2)). Uncontrollable interface formed (dotted area).

We examined the gradient formation through the side view. The fluorescence image was taken at 'on' status of the flow. Then we found not any particular fluorescence gradient was formed (**figure 4.13**).

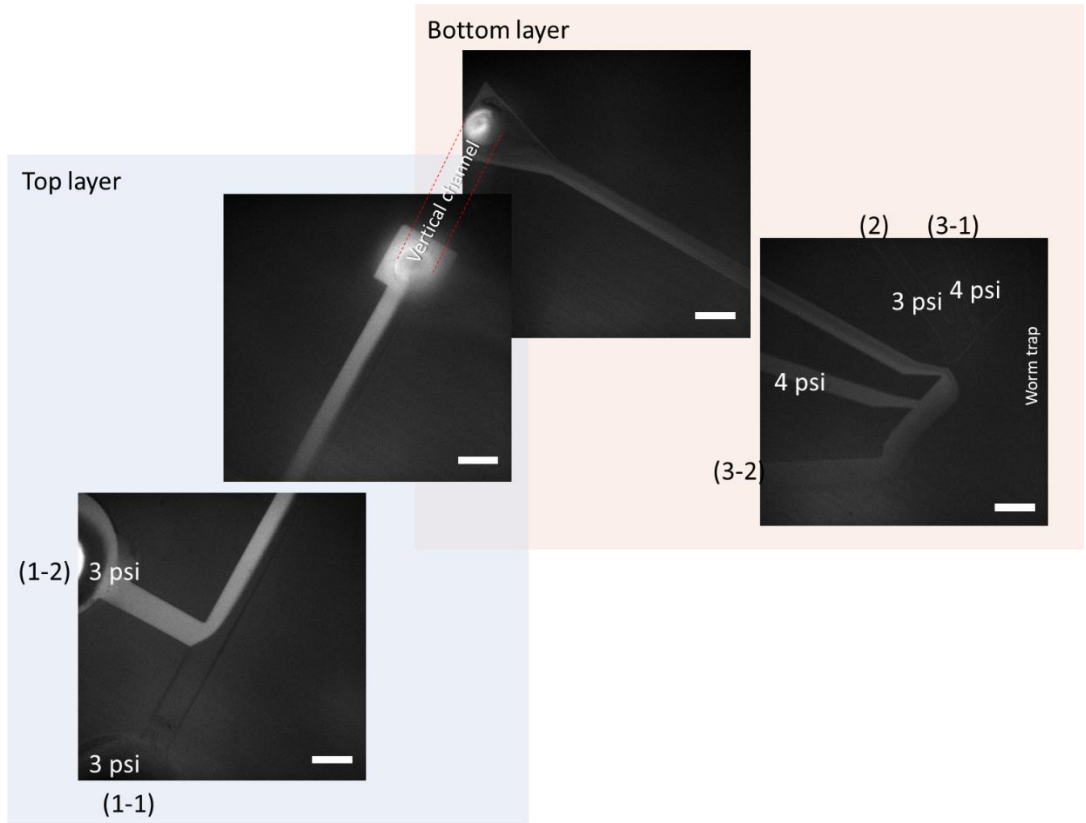


**Figure 4.12** Flow at the redirection module in the device without multidepth channel. The interface is uncontrollable. Bar indicates 200  $\mu\text{m}$ .

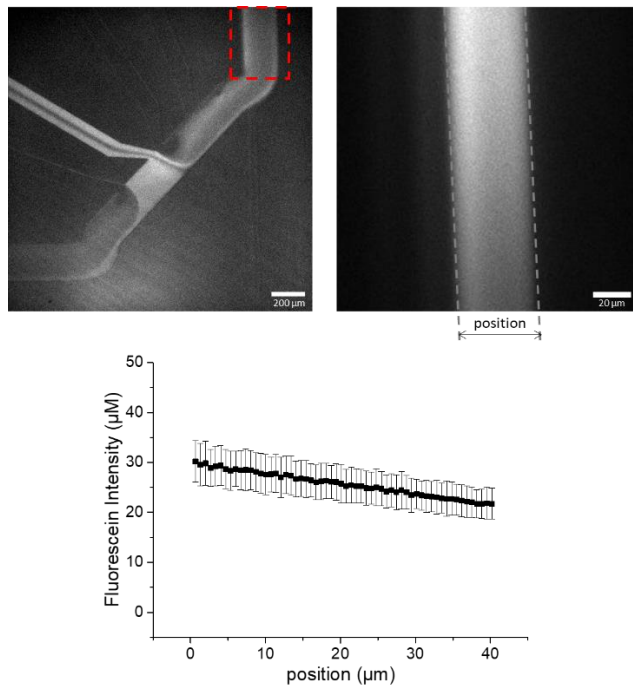


**Figure 4.13** Vertical gradient was not formed. Red dotted area was imaged through the side (right image).

### 4.3 Conclusion

We successively developed a flow transposing module to expose the worm to a vertical gradient concentration of the stimulus, and a trap module enabling half-immobilisation of the worm and allowing only the head movement. We carried out the integration of the modules to the stimulus redirection module of the side view device described in **Chapter 3**; however, not successfully. A further consideration is needed in the design to circumvent the issue of the flow control.

The channel structure modification for stabilisation of the flow shall be the first step of further study. The contact angle of two fluid is related to the laminar flow and separation forming horizontal interface.[234] We suggest to research simplified device to characterise the flow stability, starting with contact angle study.

Simplifying the device to prevent unwished condition could be one of the strategies to bypass the issue. The transposition was successful in the simple straight two-turning device but the interface formed in the integrated device was not controllable. Direct integration of the trap and flow transposition module could be one way.

## Chapter 5

### Immunoassay in femtolitre-sized droplet

This chapter deals with establishing a microfluidic device for detecting a biomarker using a bead based immunoassay in the femtolitre sized droplets (femtodroplet). We aimed to validate existing microfluidic device developed by Shim *et al.* and then port it to a new immunoassay.

#### 5.1 Introduction

We attempted to reproduce the femtodroplet immunoassay system. The microfluidic system generates femtoliter sized droplets and confine the microbead-based immunocomplex in the droplets with fluorogenic reporter molecules. And letting the confined immunocomplex produce the fluorescent product.

In order to confirm the feasibility of the device, we reproduced the microfluidic femtodroplet immunoassay device. Then, the catalytic property of the  $\beta$ -galactosidase converting FDG into fluorescein was studied. Next, the enzyme reaction was performed in the droplet. Then, immunoassay for detecting commercial prostate cancer specific antigen (PSA) was carried out in the droplet using the microfluidic device.

#### 5.2 Validation of microfluidic device for femtodroplet immunoassay

We have adapted a microfluidic device for generation and manipulation of water-in-oil droplets (femtodroplets) with a volume of 5-50 femtolitre developed by Shim *et al.*[205] Microfluidic droplets can be generated with two immiscible fluids by shearing one (water) by the other (oil). In order to generate smaller droplets with higher frequency, large shear force and low surface tension at the oil-water interface was required. More significant shear force can be achieved by either using a higher flow rate of the oil or reducing the dimensions of the channel.[3] The dimension of the flow focusing nozzle, where the oil and water phase approach, was reduced from 100  $\mu\text{m}$  wide X 25  $\mu\text{m}$  high to 10  $\mu\text{m}$  X 5  $\mu\text{m}$  to substantially increased the flow speed during droplet formation without inducing high internal pressure in threntire flow channel in the device (**figure 5.1**).

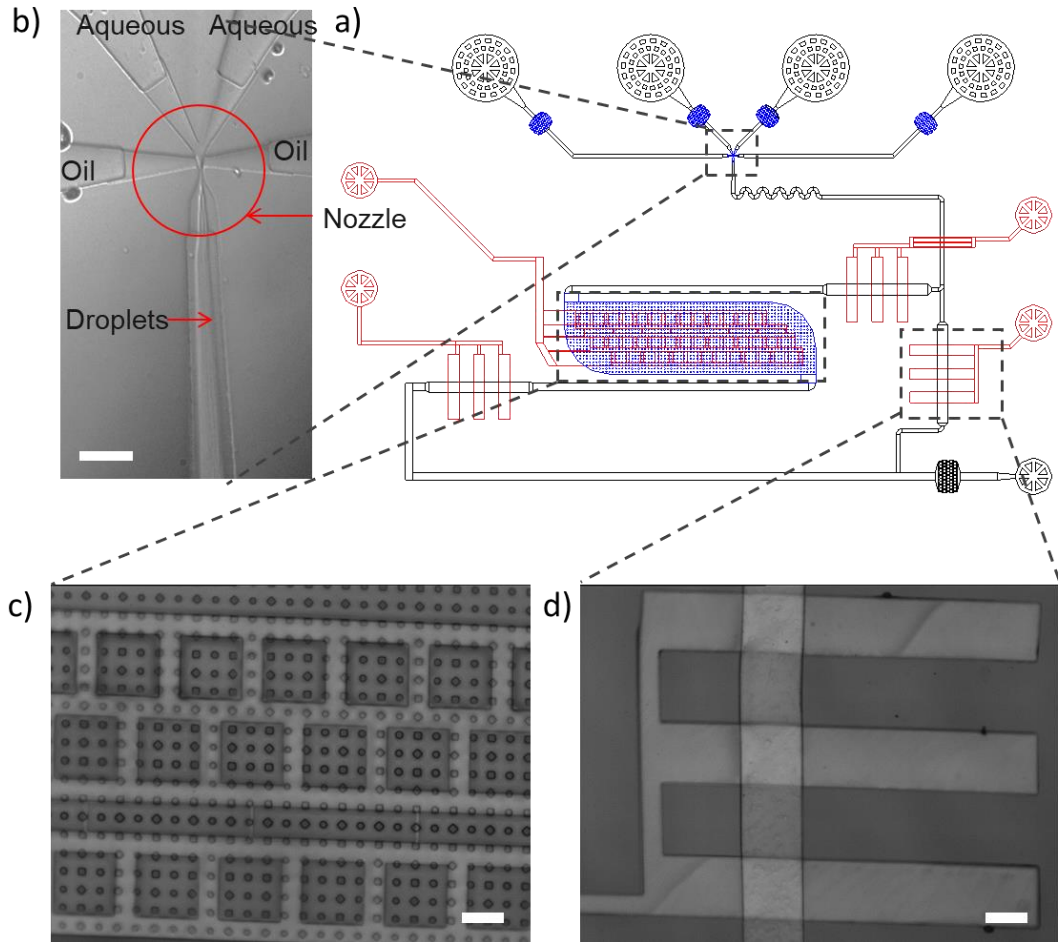


**Figure 5.1** The scheme of the femtodroplet immunoassay device. a) The design of the device. The black (25  $\mu\text{m}$ ) and blue (5  $\mu\text{m}$ ) coloured sketches are for the flow channel including femtodroplet generating nozzle b) at the upper layer and the red for the air-pressure-driven trap c) and valve d).

We aimed to generate 2.5~4.5  $\mu\text{m}$  droplet by controlling the flow rate of the aqueous and oil phase. We fixed the flow rate of the aqueous phase as 30  $\mu\text{L h}^{-1}$  and adjusted the oil phase to control the size of the droplet. The frequency of the droplet production was calculated as

$$F = \frac{S}{\frac{4}{3}\pi(D/2)^3} \quad (\text{Equation 5.1})$$

, where F is the frequency of the production, S is the flow rate of the aqueous phase, D is the diameter of the femtodroplet. In our range of the droplet size with the fixed flow rate, the frequency of the droplet production ranged between 2 ~ 6  $\times 10^5$  droplets  $\text{s}^{-1}$  (figure 5.1b).

These droplets encapsulated enzyme with fluorogenic substrate fluorescein di- $\beta$ -D-galactopyranoside (FDG). Once encapsulated, the enzyme hydrolysed the substrate and accumulated fluorescent product in the droplet. It takes a few minutes to be detectable.

Therefore, the storage area was integrated into the device to trap and store the femtodroplets until the enzyme reaction occurred (**figure 5.1c**). This area was divided into 40 square shaped traps ( $300\ \mu\text{m} \times 300\ \mu\text{m}$ ) by a monolithic valve set up underneath the storage area.[42, 235-237] The depth of the trap was designed as  $5\ \mu\text{m}$ , comparable to the diameter of the femtodroplet, for the droplets to be stored as a single layer, so that allows the imaging and measurement of the droplets with a simple epi-fluorescence microscope. (**figure 5.2**). Additional monolithic valves were installed to control the direction of the stream and flush the droplets into the storage area (**figure 5.1d**).

This multilayered PDMS with multiple depths was fabricated with two masters. One was for the droplet flow channel with the nozzle (top layer PDMS) and storage area and the other for the trap and valves (bottom layer PDMS). The top layer PDMS was moulded using a commercial PDMS kit (Sylgard184, Dow Corning) containing a base and cross-linker. The weight ratios between base and cross-linker for the top layer PDMS and bottom layer PDMS were 5:1 and 20:1. A thin PDMS layer was constructed by spinning the liquid PDMS mixture on the master. Then, it was baked at  $95^\circ\text{C}$  for 6 minutes. Then, the top layer PDMS was attached to the bottom layer PDMS. Then both layers were baked for 30 minutes. It formed cross-links between the top layer and bottom layer strong enough to operate the immunoassay.

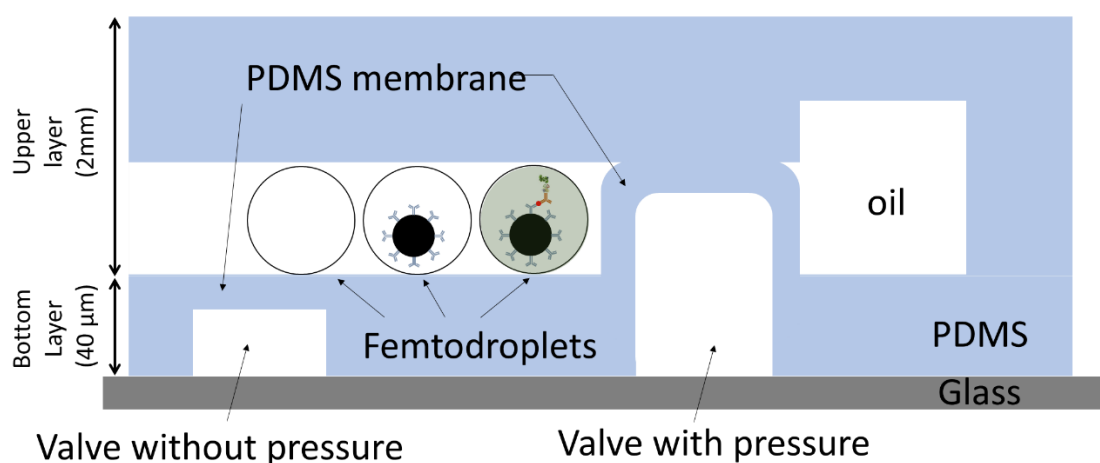


**Figure 5.2** The scheme of the femtodroplet immunoassay device. The monolithic air-pressure-driven trap stretched the PDMS membrane between the upper and bottom layer of the channel and blocked the flow of the upper channel so that the square-shaped traps immobilise the femtodroplets.

We aimed to make the bottom layer of the PDMS as  $40\ \mu\text{m}$ , slightly thicker than the photoresist so that a thin PDMS film formed on the top of the channel.

If the PDMS layer is too thick, high air pressure is required to stretch the film. Conversely, if it is thinner than the height of the photoresist, the top of the PDMS would become undulating along with the structure of the photoresist. This curvature critically affected the structure, mainly when it occurred at the trap valve, as the depth of the storage area is only 5  $\mu\text{m}$ . It induced a collapse between the trap valve and the storage area. We tested three different thickness of the PDMS by altering the spinning rate and found thicker PDMS induced less collapse (**Table 5.1**). In our range of thickness, there was no issue of the valve operation as the covalent bond between the valve layer PDMS and glass substrate was durable enough to apply over 80 psi. The valves blocked the flow completely at 60 psi in the experiment.

**Table 5.1** Finding the condition of PDMS spin coating on the master for the bottom layer. Too thin PDMS induced the collapse of the channel after the binding two layers of the PDMS. One master contains six devices.

Spinning speed (RPM)	2000	1800	1600
Total	6	6	6
Collapsed	2	4	0

### 5.3 Validation of enzyme: kinetics of free $\beta$ -galactosidase

Then, in order to determine the concentration of the substrate and incubation time, we calculated the turnover rate of the streptavidin  $\beta$ -galactosidase. Although FDG is a widely used fluorogenic substrate for  $\beta$ -galactosidase, its diglycosylated structure results in a sequential two-step hydrolysis mechanism. The kinetics of each has been the subject of some debate in the literature.[238-240] While this complication prohibits detailed kinetic analysis of the data, the similar saturation behaviour to a single enzyme reaction would be expected.[205, 241]

Enzyme reaction kinetics study was carried out. The reaction rate of streptavidin  $\beta$ -galactosidase ( $2.32 \times 10^{-3}$  unit /mL) converting the FDG (1 to 500  $\mu\text{M}$ ) into fluorescein and galactoses was measured. The increase of the fluorescence intensity was directly converted to the concentration of the product and the reaction velocity.

We found the  $K_m$  and maximum velocity  $V_{max}$  was estimated by the Michaelis Menten equation. We found the maximum velocity was  $9.40 \pm 1.1$  nM /min, and the Michaelis constant  $K_m$ , the substrate concentration at which the reaction rate is half of the maximum velocity, was  $173 \pm 48$   $\mu$ M. It was higher than the value of 18  $\mu$ M, which is measured by Huang *et al.* [240, 242] and close to 94  $\mu$ M by Shim *et al.*[205]

Then we estimated how fast the enzyme converted the substrate into the product when the enzyme was saturated with the substrate. Turnover number ( $K_{cat}$ ) was defined as

$$K_{cat} = \frac{V_{max}}{[E]} \quad (\text{Equation 5.2})$$

, where  $[E]$  is the concentration of the enzyme. Enzyme concentration was estimated as 0.2 pM under the assumption that the streptavidin and  $\beta$ -galactosidase have been conjugated at a 1:1 ratio and that the molecular weight of the protein was 116 kD. It was found that  $4.70 \times 10^4$  molecules were produced per minute. Additionally, we computed the reaction rate and the at the concentration of 250  $\mu$ M, where our femtodroplet immunoassay system employs. We found the reaction rate was 6.11 nM/ min, which is 65% of the maximum velocity, equivalent to  $2.78 \times 10^4$  molecules per minutes.

Then we computed the incubation time of the reaction. As shown in **figure 5.11**, the accumulation of the fluorescein should be achieved more than 1  $\mu$ M to be visible in the system. 1  $\mu$ M of fluorescein confined in a single femtodroplet of which the volume is 50 fL, would be equivalent to the condition that  $3.0 \times 10^4$  molecules of the products are in the droplet. In the assumption when the condition in the femtodroplet is the same with the condition used for the kinetics study, the accumulation of 1  $\mu$ M fluorescein can be achieved in 65 seconds.

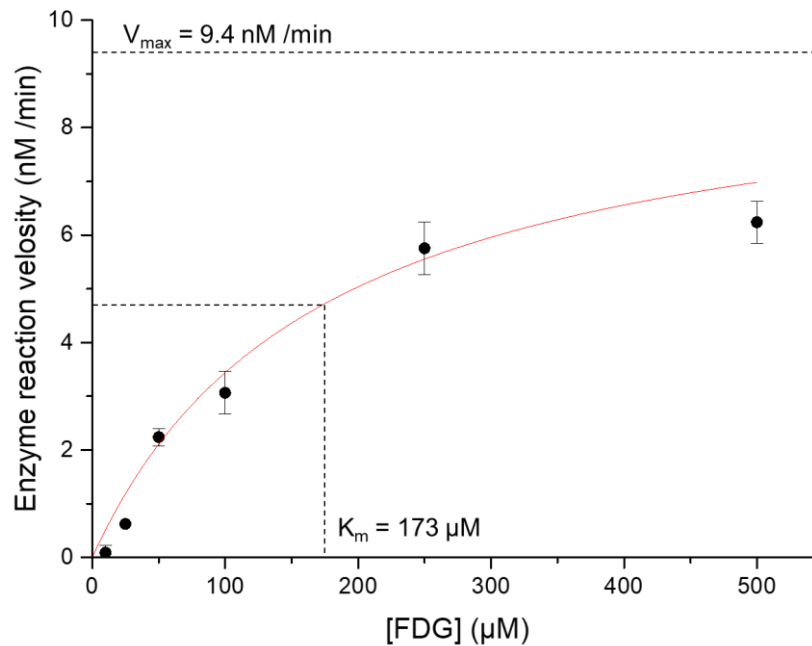


**Figure 5.3** Kinetic study of streptavidin- $\beta$ -galactosidase. Michaelis constant  $K_m = 173 \pm 48 \mu\text{M}$  and the maximum velocity  $V_{\text{max}} = 9.40 \pm 1.1 \text{ nM/ min}$

#### 5.4 Validation of the system: enzyme reaction in the droplet

In a typical bulk assay, the catalytic properties of individual enzyme molecules are concealed. However, the use of small chambers such as femtodroplets, capillary or an optical fibre bundle enables measurement of the enzyme reaction of a single molecule.[219, 243] Single enzyme confined with an excessive amount of fluorogenic substrate can produce fluorescence molecules in the droplet. In our assay, small numbers of the enzyme were confined into a large number of femtodroplets. Then, small numbers out of all the femtodroplets yielded detectable fluorescence by the catalytic reaction. By observing the occupancy of single molecules in the femtodroplets, we can count the number of the molecules using Poisson distribution and determine the concentration of the enzyme based on the volume of the femtodroplets.

When all the generated monodispersed 50 fL femtodroplets contained one enzyme, the average concentration of enzyme would be 33 pM. However, the enzyme molecules in the solution injected into the array of femtodroplets will not result in the distribution of exactly one enzyme per one femtodroplet. Statistically, it is more plausible that some droplets contain no enzyme molecules while other single molecules and others more than two. When the number of enzyme molecules per femtodroplet is high, the data can be fit a

Gaussian distribution. On the other hand, when the number of the enzyme molecule is much smaller than the number of droplets, Poisson distribution can be applied for a rare event occurring in a large number of trials. (15)

Probability of droplet containing  $v$  molecules of the enzyme was computed as

$$P(v) = e^{-\mu} \left( \frac{\mu^v}{v!} \right) \quad (\text{Equation 5.3})$$

, where  $\mu$  is the expected average number of the enzyme out of the number of femtodroplets.

$$\mu = \frac{[E]}{nV} \quad (\text{Equation 5.4})$$

, where  $[E]$  is the concentration of the enzyme,  $n$  is the number of the femtodroplet,  $V$  is the volume of one femtodroplet.

If the concentration of the enzyme was much less than 33 pM, the probability of finding femtodroplets containing other than one or zero molecules of enzyme becomes exceptionally low. For example, at 1.0 pM molecules in this system, less than  $6 \times 10^{-2}$  per cent of the droplets would contain more than one enzyme molecule, which is nearly improbable in the system.

We performed the enzyme reaction in the droplet. The final concentration of 94 pM  $\beta$ -galactosidase and FDG was loaded in identical gastight syringes and injected into the device through the inner inlets using a syringe pump. The fluorinated oil (HEF-7500, 3M) containing a surfactant) was injected through the outer inlets. The droplets confining the substrate and enzyme were generated and flew to the outlet of the device. The direction of the flow was controlled by the main valve actuated by air pressure. Then the droplets were immobilised by the trap and incubated until the fluorescence intensity exceeded the threshold of the detection. This was the concentration that an average number of the molecules in one femtodroplet was 2.8. The probability that the femtodroplet contains one enzyme is 17%, two enzymes 24% and three enzymes 22%.

The area surrounded by the surface of the droplet was set as ROI in brightfield image. As the diameter of the droplet was 2.5 - 4  $\mu\text{m}$ , 1  $\mu\text{m}$  by 1  $\mu\text{m}$  square ROIs were set for individual 2,740 droplets. Then the fluorescence intensity of each ROI was measured. AS a result, we confirmed the accumulation of the fluorescence reporter by enzyme reaction (**figure 5.4a and b**). However, the increase of fluorescence intensities in each droplet didn't distribute multimodally. (figure5.4b), which means our system was not able to

discriminate the enzyme occupancy clearly (figure 5.4b). This might be because the activities of individual enzyme molecules range broadly (**figure 5.4**).[194]

Then, we decreased the concentration of the enzyme and investigated a single enzyme reaction of the fluorescein di- $\beta$ -D-galactopyranoside (FDG)/  $\beta$ -galactosidase reporter system in the femtodroplet to optimise the substrate concentration and reaction time. The same assay was carried out with a smaller concentration of  $\beta$ -galactosidase (0, 0.94, 9.4, and 94 pM respectively). The fluorescence microscope images in **figure 5.5a** show that the fluorescent molecules were produced in the femtodroplet, and the product in the droplet was accumulated in the droplet without significant leakage or coalescence during the measuring time. The number of fluorescent femtodroplets was counted, and the quantified signal was converted to the concentration. The fraction of the number of enzymes out of total droplets was calculated by the fraction of the number of fluorescent droplets out of total droplets (0.102 for the 9.4 pM, 0.023 for 0.94 pM., 0.0022 for 0.001 for 0.094 pM., and 0 for 0 pM respectively) (**figure 5.5b**). The possibility in these cases of a droplet being occupied by more than 2 enzymes was 0.49 %, 0.026 %,  $2.4 \times 10^{-3}$  %, and 0 %, respectively (**figure 5.5b and 5.5c**). The linear correlation between the prepared and determined concentration is shown in **figure 5.5d**. Consequently, the linear correlation between the prepared and the calculated by droplet counting shows the potential availability of the system applying for the bead-based single molecule immunoassay.

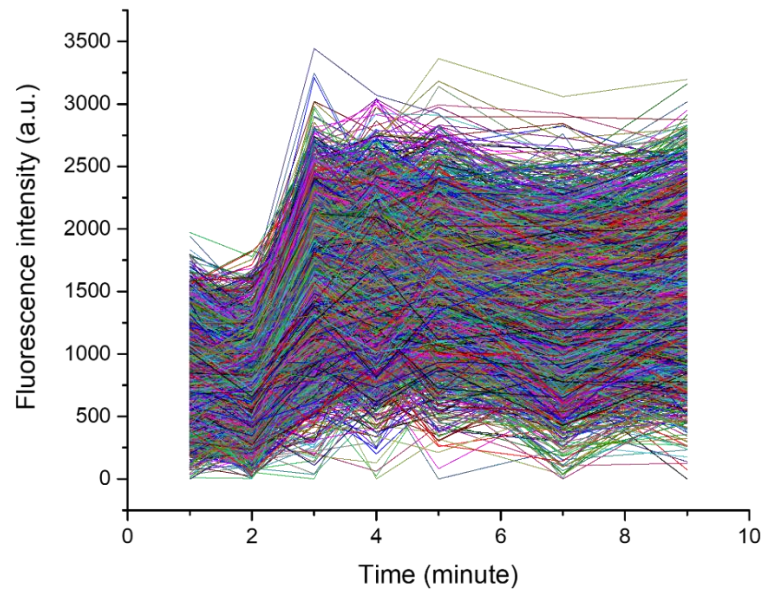
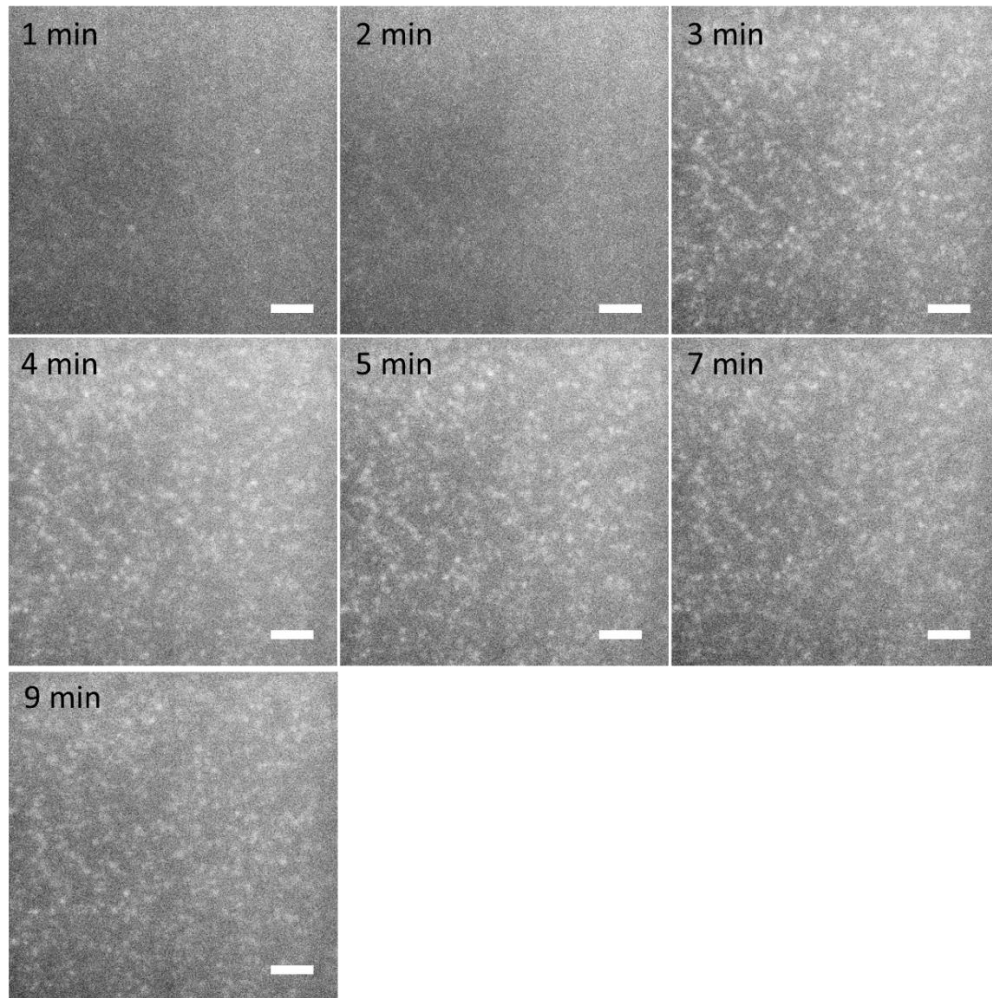


**Figure 5.4** Fluorescein production by  $\beta$ -galactosidase in the femtodroplets. The increase of fluorescence in individual 50 droplets show the accumulation of the fluorescein in the femtodroplet.

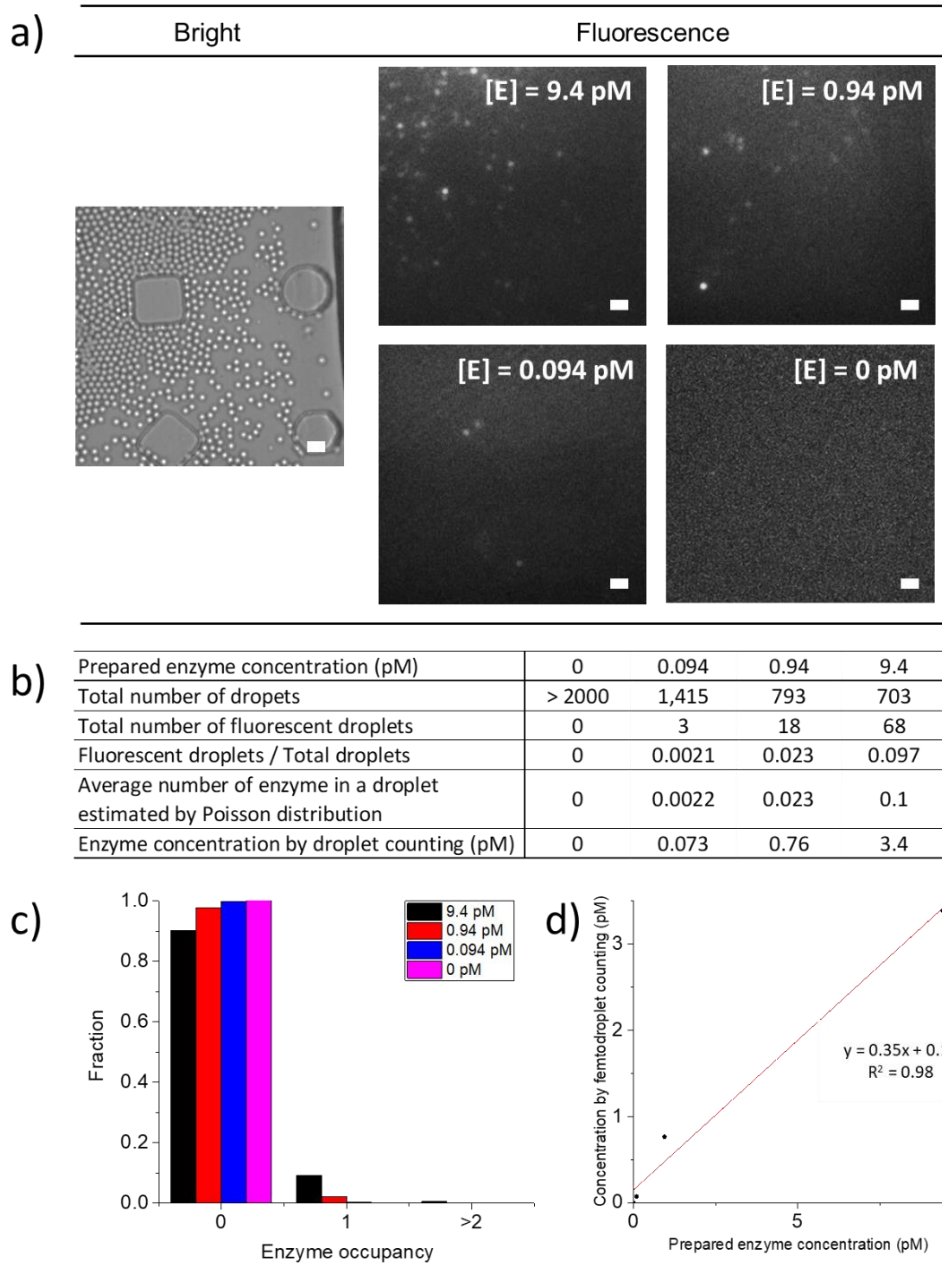


**Figure 5.5** Enzyme reaction in femtodroplet a) monodispersed size of femtodroplets containing  $\beta$ -galactosidase and fluorogenic substrate FDG were trapped and incubated. The femtodroplets became fluorescent after 10 minutes by the accumulation of converted fluorescein. Error bars indicate 10  $\mu$ m; b) The fractions of the number fluorescent femtodroplet out of a total number of the droplet was converted to the determined concentration of the enzyme after correction by Poisson distribution; c) The femtodroplets could contain zero, one or more than one enzymes. In the concentration between 0 to 9.4 pM, the probabilities of occupancy that more than one enzyme was confined in one droplet yield was less than 0.5 per cent of the total femtodroplets; d) The determined concentration of the enzyme by femtodroplet counting showed a linear correlation with the prepared concentration.

## **5.5 Immunocomplex construction and femtodroplet immunoassay**

Bead-based single molecule immunoassay was carried out in the femtodroplet. Typically, ELISA is performed in a vessel where capture antibody (the primary Ab) is bound on the surface. Existence of the target molecule in the sample induces target-dependent immunocomplex formation by following consecutive steps of 1) binding of the detection antibody (the secondary Ab) onto the target molecule and 2) binding of enzyme onto the detection antibody. Then, the immunocomplex yields the enzyme reaction, so that accumulates the reporter molecules.

On the other hand, bead-based immunoassay requires the formation of the immunocomplex on the bead instead of the surface of the vessel. So we constructed the capture bead specific to the target. Before employing the renal grafting failure biomarker specific antibodies, we tested commercial prostate cancer specific antigen(PSA) and antibodies specific to PSA to confirm the feasibility of the system.

### **5.5.1 Capture bead construction**

Capture beads were constructed as shown in **figure 5.6**. It was constructed by cross-linking the primary anti-PSA-antibody (CabAb) (R&D system) onto the surface of amino-functionalised polystyrene beads (Polyscience) with glutaraldehyde using a commercial coupling kit (Polyscience) according to the manufacturer's instructions. 1  $\mu\text{m}$  diameter polystyrene microbeads were selected so that they are small enough to be encapsulated in 2.5-4.5  $\mu\text{m}$  diameter droplets. Glutaraldehyde functioned as a cross-linker between the primary amine group of the protein and the surface of the microbead. Then bovine serum albumin (BSA) was treated to quench the remaining reactive site of glutaraldehyde, reduce any non-specific binding on the surface of the bead, and prevent the agglomeration of the particle as BSA is negatively charged in PBS). A detailed procedure of bioconjugation is described in **Chapter 2**.

### **5.5.2 Qualification of the conjugation by intrinsic fluorescence of the protein**

The protein conjugation on the microbead was confirmed by investigation of the intrinsic fluorescence of the protein on the microbead. The formed capture beads were located on the glass slide and the red fluorescence under the illumination of green light was imaged by epi-fluorescence with a Texas red cube filter setup. As a result, the red autofluorescence was detected on the

capture beads (shown in the first and second row of **figure 5.7**). It is possibly due to the intrinsic fluorescence of the monoclonal antibody.[205]

We designed the system to take advantage of this to easily count the immunocomplex in the droplet. However, the fluorescence of the capture bead was not detected when they were injected into the device (**figure 5.7**). It is possibly due to absorbance and reflectance of the thin PDMS layer (bottom layer) between the bead in the trap and the glass slide even it is thin, or roughness of the PDMS which inevitably occurs in the procedure of soft-lithography. [244]

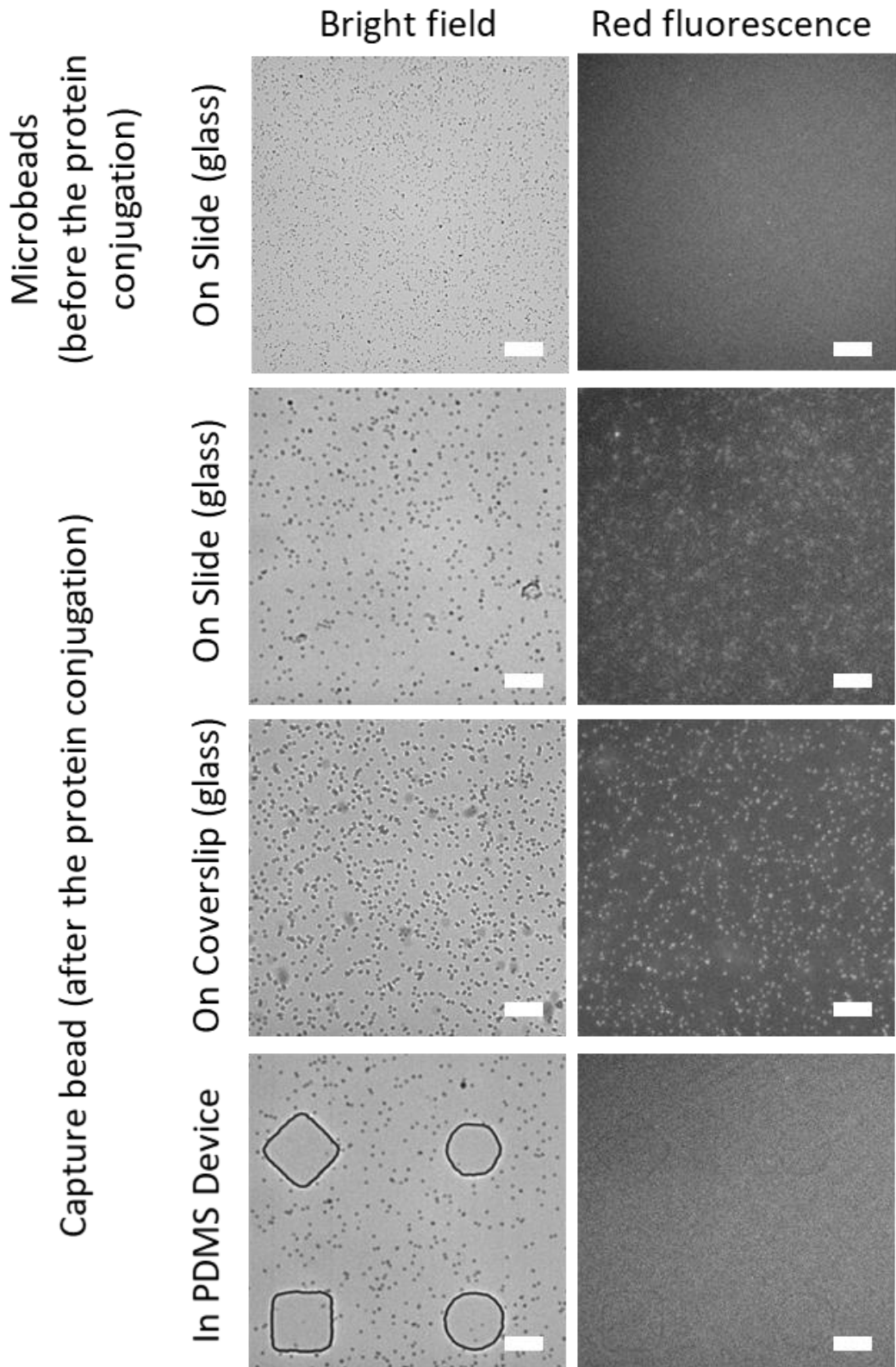


**Figure 5.6** Autofluorescence of the polystyrene microbead and capture bead. The red fluorescence was detected for beads on the fused silica glass, but not in the PDMS device. Bars indicate 20  $\mu\text{m}$ .

### 5.5.3 Estimation of the amount of capture antibody bound on the microbead.

The capture antibodies were covalently coated on the surface of the amino-functionalised polystyrene bead. In order to estimate the amount of the capture antibody conjugated on the microbead, we measure the protein concentration of the antibody solution before and after the conjugation procedure. Measurement of the absorbance at the wavelength of 280nm, a typical method of protein quantification, was carried out by nanodrop. However, the absorbance increased after the cross-linking by glutaraldehyde molecules at the wavelength of 280 nm (data not shown). It might be because the glutaraldehyde absorbs ultraviolet spectra at the range of 220 – 340 nm.[245]

So, we indirectly estimated the amount of the capture antibody on the surface of the microbead, based on the size of the immunoglobulin G and the surface area of the microbead. Cantarero *et al.* reported that the immunoglobulin could bind to the surface of the polystyrene with a density of 3.1 mg m<sup>-2</sup>. [246] Assuming that the microbead is spherical, the immunoassay surface area of a 1 µm bead was 3.14 X 10<sup>-12</sup> m<sup>2</sup>. The mass of the immunoglobulin is known as 160 kD, then the number of molecules that can bind to the surface of a single 1 µm polystyrene bead is computed as

$$3.1\text{mg}/\text{m}^2 = \frac{x \text{ mol} \times 160,000 \text{ g/mol}}{\text{surface area of the microbead}} \quad (\text{Equation 5.5})$$

Base on this calculation, we expect that one bead holds maximum 3.7 X 10<sup>4</sup> immunoglobulin G. As excessive amount of the antibody was used for the conjugation procedure, we believe that the microbead binds the maximum amount of the capacity.

### 5.5.4 Femtodroplet Immunoassay

The femtodroplet immunoassay is carried out by the formation of the immunocomplex and confining the immunocomplex into the femtodroplets with FDG, the fluorogenic reporter molecule. The immunocomplex formation pre-requested the binding of the PSA onto the capture antibody conjugated on the surface of the capture bead, followed by the binding of the biotinylated detection antibody on the bound PSA and binding of streptavidin conjugated enzyme onto the detection antibody by streptavidin-biotin interaction. The immunocomplex formation occurred out of the device and was then injected

into the device. The immunocomplex was loaded in one syringe and the FDG solution the other identical syringe so that the immunocomplex is surrounded by FDG molecules only in the femtodroplets.

When the femtodroplets were generated, three features of the bead constitutes the droplet population as shown in **figure 5.8**. When there was no bead in the droplet (top) or bead on which the target molecule is not bound (middle), the substrate encapsulated in the droplet is not converted. However, when the bead where the immunocomplex formed is confined in the droplet, the enzyme consisting of the complex hydrolyses the fluorogenic substrate into fluorescein (bottom).

The femtodroplets were immobilised in the trap and imaged by epi-fluorescence microscope. Only the droplets containing immunocomplex were fluorescent. The concentration of the PSA was calculated using Poisson distribution.

When PSA is bound to the capture beads, the maximum amount of PSA is supposed to be captured as the dissociation constant of immunoglobulin G is micromolar to nanomolar.[247] As one bead conjugates ten thousand capture antibodies, multiple PSA can be captured onto the bead. We bound 60 pM PSA onto 10 pM capture bead. At this concentration, 99.8% of the bead was expected to be occupied by at least one PSA and form the immunocomplex; only 0.2% of the bead was expected to remain unoccupied. The femtodroplets confining the capture bead are anticipated to emit green fluorescence by the biocatalytic reaction of the  $\beta$ -galactosidase converting the FDG into fluoresceins. So we calculated the fraction of the number of fluorescent femtodroplets out of the number of capture beads. The capture beads were visible in the bright field. However, only 36% of the capture bead produced fluorescein enough to be detected. From this, we can estimate that the concentration of PSA was 4.5 pM, which is one order lower than the prepared concentration. When tested at 6 pM, the concentration that is expected to have 26% of fluorescent droplet out of fluorescent droplet, no fluorescence droplet was detected. The signal efficiency of the bead was 7.5%, which was one order lower than what previously reported; Rissin *et al.* >70% and Shim *et al.* 89%.[203] We conclude that this system is not applicable for further studies.

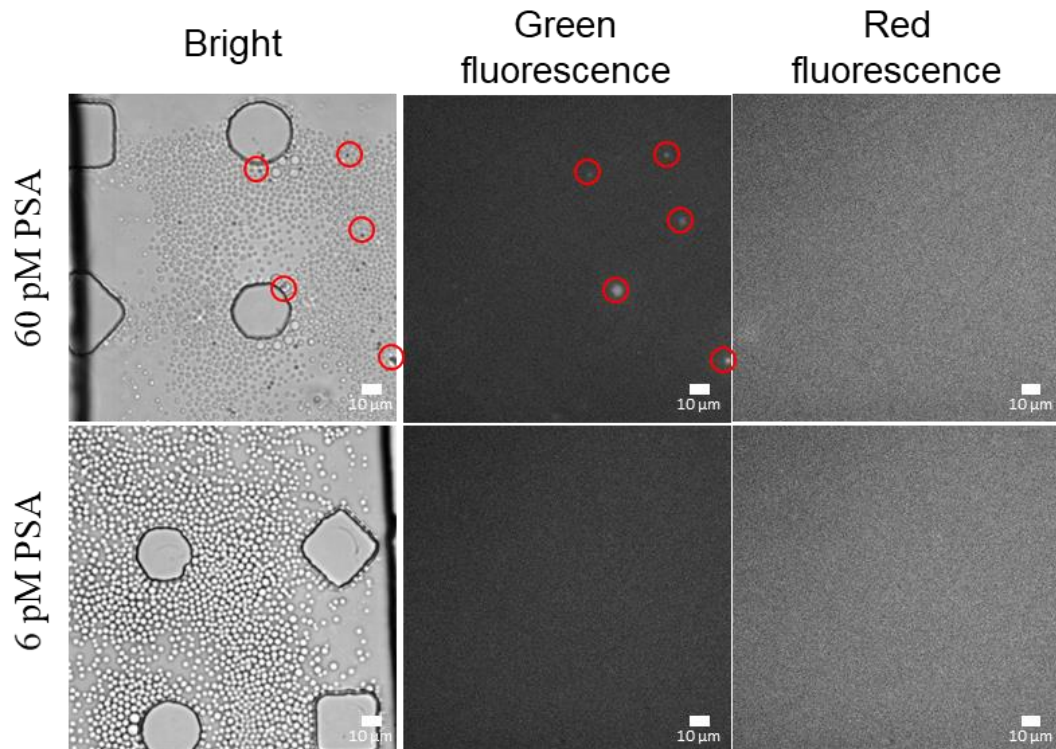


**Figure 5.7** Femtodroplet immunoassay. The signal efficiency was too low.

## 5.6 Conclusion

In summary, **Chapter 5** describes a microfluidic system to generate femtolitre droplets with the diameter between 2.5 to 4.5  $\mu\text{m}$  at a hundred thousand hertz frequency. These droplets can confine purposed molecules by microfluidic manipulation and enables the measurement of the single enzyme reaction. This approach enables quantification of low abundance biomarkers by carrying out microbead-based immunoassay in femtodroplet with direct counting of the droplets containing a single immunocomplex. However, our system was not able to discriminate the fluorescent signal.

We detected accumulation of catalytic product in the femtodroplet (**Figure 5.4** and **5.5**) but not clear accumulation in immunoassay (**Figure 5.7**). So, we suggest that the less efficiency in immunocomplex formation might be one reason for the unsuccessful study. ELISA assay should be carried out to confirm this.

The renal graft failure biomarker and the antibodies for the biomarker remained untested. However, after the confirmation of the microfluidic system, we anticipate the application of the new biomolecules for the femtodroplet immunoassay system can be carried out without difficulty.

## Chapter 6 Discussion and conclusion

This work in **chapter 3** demonstrates a novel rotatable microfluidic chip (side view chip) that is used for multiangle imaging of *C. elegans*, especially for imaging bilateral sensory neurons in the control of stimulus treatment. Unlike other microfluidic devices which have been reported previously for rotating the worm, [177, 178] Our device enables rotating the worm without physical touch. Instead, we rotate the chip itself and image through the transparent wall of the device. The manipulation of rotating the chip itself places the bilateral left and right neurons in the same focal plane. Furthermore, we integrated the stimulus delivery module previously reported by Chronis *et al.* [56], which enables to study chemoresponse of individual worm reliably. Altogether, our device is suitable for reliable measurement in the response of bilateral neuron simultaneously.

We imaged calcium response of bilateral sensory neurons of ASH and ASE and statistically estimated whether the response of each left-right pair of neurons is functionally synchronised. It is known that ASE left and right neurons are functionally asymmetric,[86] On the other hand, ASH neuron is known as symmetric. However, whether ASH left and right are sharing the information has never been reported.

As a result, in intermediate concentration, where not all or none of the neurons are responsive, the response of ASH neurons pairs are not independent based on the Fisher's exact test, and the fraction of synchronous neuron pair is higher than the probability of synchrony. These support the existence of functional connection between ASH left and right neuron.

Gap junctions between two ASH neurons might support the result anatomically. However, our strain development was not successful. Reliable production of *inx-19* knocked out strain might enable elucidation of the role of the gap junction in the synchronisation between bilateral ASH.

The side view chip can multi-angle image the trapped organism. It could be useful in other biological research which need to image the object from different angle in the experiment. The strength of this system is its simplicity and low cost comparing to sophisticated 3d image systems. A limitation of this technique is that the PDMS wall cannot be built as thin as glass material. Flexibility of PDMS is far higher than glass, pressure in the channel might swell the PDMS. This limits the selection of the lenses to the long working distance objective.

This side-view device is very similar to what Hochstetter *et al.* reported[179]. They construct the device with the hydrophobically coated glass wall structure, and we built it curing additional PDMS on the surface of the wall. Their study focuses on the integration of the 4-side clear PDMS onto imaging systems. On the other hand, we applied our system to actual multi-angle imaging in biological research.

The work in **chapter 4** demonstrates the development of a multi-layered microfluidic device to image the response of bilateral neurons and the movement of the head at the same time in the controlled field of gradient of stimulus. Integrating the module to the side-view chip, the stimulus field should spread through the z-axis. We successfully developed a flow transposition module using two turning 3D channel. Simple turning the x-axis flow to z-axis, and then y-axis rotates the vertical interface into horizontal. Vertical gradient would form easily by adding a mixing module to the flow transposition module. Numerous mixers have been introduced.[3, 248]

This transposition module could be applied to another useful field. For example, we anticipate that the transposing module can be used for sorting any buoys or sediments by separating the material by gravity and transposing them to collect. Transposition of the flow would spread the material separated through the z-axis to the y-axis.

Then, we demonstrate a fork reinforced trap to hold the posterior half of the worm body so that the head of the worm can move freely. The air pressure driven fork is located in the same layer of the trap and presses the side of the trap to prevent the worm from escaping. Typically air pressure driven trap for the worm trap is located above or beneath the trap, which requires an additional layer and additional process of fabrication.[146] Another advantage of the trap in the same layer is that it can be selected as a good alternative when an additional module should be located vertically.

Then we integrated the transposition module, and the fork reinforced trap to the stimulus redirection module of the side view device described in **Chapter 3**, however it was not successful. The uncontrolled interface was formed instead of horizontal interface. The most challenging issue in realisation of the worm head device is to build a stable interface between two flows.

The channel structure modification for stabilisation of the flow shall be the first step of further study. The interface between flow was not controllable in the wormhead device, which has complex structure comparing to the straight two-turning device. Or, simplifying the device to prevent unwished condition could

be one of the strategies to bypass the issue. Direct integration of the trap and flow transposition module could be one way. An alternative system for forming horizontal interface has been introduced by Miyazaki *et al.*[234] Instead of transposing the flow, they built multi-depth channel and realised the horizontal interface between two fluids.

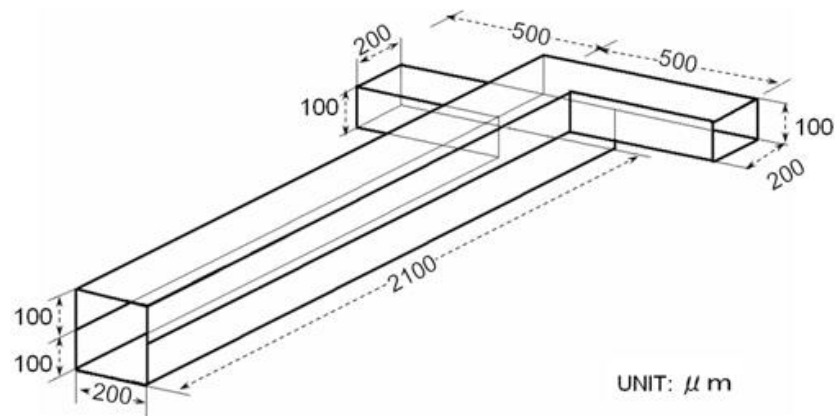


**Figure 6.1 3D device for horizontal interface. Instead of transposition, two fluids were injected from each inlet with different height. Adapted from Miyazaki *et al.*[234]**

**In Chapter 5**, we validated the existing microfluidic device invented by Shim *et al.* Using this microfluidic system to generate femtolitre droplets with the diameter between 2.5 to 4.5 μm at a hundred thousand hertz frequency. This femtodroplet can confine purposed molecules by microfluidic manipulation and enables the measurement of the single enzyme reaction. This approach enables to quantify low abundant biomarker by carrying out the microbead-based immunoassay in the femtodroplet with direct counting of the droplets containing single immunocomplex. However, our system was not able to discriminate the fluorescent signal. It might be due to the inefficient imaging system or less efficient immunocomplex formation. ELISA assay should be carried out to confirm the issue.

## Reference

1. Nguyen, N. Wereley, S. *Fundamentals and Applications of Microfluidics* (Artech House, Boston, London). 2006.
2. McDonald, J.C. *et al.*, *Fabrication of microfluidic systems in poly(dimethylsiloxane)*. ELECTROPHORESIS, 2000. **21**(1): p. 27-40.
3. David J. Beebe, A. Glennys A. Mensing, and G.M. Walker, *Physics and Applications of Microfluidics in Biology*. 2002. **4**(1): p. 261-286.
4. Hong, J.W. Quake, S.R. *Integrated nanoliter systems*. Nature Biotechnology, 2003. **21**(10): p. 1179-1183.
5. Stone, H.A., Stroock, A.D. and Ajdari, A. *Engineering Flows in Small Devices: Microfluidics Toward a Lab-on-a-Chip*. Annual Review of Fluid Mechanics, 2004. **36**(1): p. 381-411.
6. Squires, T.M. Quake, S.R. *Microfluidics: Fluid physics at the nanoliter scale*. Reviews of modern physics, 2005. **77**(3): p. 977.
7. Dittrich, P.S., Tachikawa, K. and Manz A., *Micro Total Analysis Systems. Latest Advancements and Trends*. Analytical Chemistry, 2006. **78**(12): p. 3887-3908.
8. Whitesides, G.M., *The origins and the future of microfluidics*. Nature, 2006. **442**(7101): p. 368-373.
9. Liu, R.H. *et al.*, *Passive mixing in a three-dimensional serpentine microchannel*. Journal of Microelectromechanical Systems, 2000. **9**(2): p. 190-197.
10. Song, H. Tice, J.D. Ismagilov, R.F. *A Microfluidic System for Controlling Reaction Networks in Time*. Angewandte Chemie International Edition, 2003. **42**(7): p. 768-772.
11. Stroock, A.D. *et al.*, *Chaotic Mixer for Microchannels*. Science, 2002. **295**(5555): p. 647-651.
12. Kopp, M.U. A.J.d. Mello, and A. Manz, *Chemical Amplification: Continuous-Flow PCR on a Chip*. Science, 1998. **280**(5366): p. 1046-1048.
13. Sun, B, *et al.*, *Application of microfluidics technology in chemical engineering for enhanced safety*. Process Safety Progress, 2016. **35**(4): p. 365-373.
14. Elvira, K.S. *et al.*, *The past, present and potential for microfluidic reactor technology in chemical synthesis*. Nature chemistry, 2013. **5**(11): p. 905.
15. Rondelez, Y. *et al.*, *Microfabricated arrays of femtoliter chambers allow single molecule enzymology*. Nature biotechnology, 2005. **23**(3): p. 361-365.
16. Tsui, N.B.Y. *et al.*, *Noninvasive prenatal diagnosis of hemophilia by microfluidics digital PCR analysis of maternal plasma DNA*. Blood, 2011. **117**(13): p. 3684-3691.
17. Wang, Y. *et al.*, *A microfluidic digital single-cell assay for the evaluation of anticancer drugs*. Analytical and bioanalytical chemistry, 2015. **407**(4): p. 1139-1148.
18. Chung, J. *et al.*, *Fast and continuous microorganism detection using aptamer-conjugated fluorescent nanoparticles on an optofluidic platform*. Biosensors and Bioelectronics, 2015. **67**: p. 303-308.

19. Young, E.W. Beebe D.J., *Fundamentals of microfluidic cell culture in controlled microenvironments*. Chemical Society Reviews, 2010. **39**(3): p. 1036-1048.
20. Nekimken, A.L. et al., *Pneumatic stimulation of C. elegans mechanoreceptor neurons in a microfluidic trap*. Lab on a Chip, 2017. **17**(6): p. 1116-1127.
21. Lucchetta, E.M. et al., *Dynamics of Drosophila embryonic patterning network perturbed in space and time using microfluidics*. Nature, 2005. **434**: p. 1134-1138.
22. Reza, G. Ponnambalam, R.S. *Microfluidic Devices for Automation of Assays on Drosophila Melanogaster for Applications in Drug Discovery and Biological Studies*. Current Pharmaceutical Biotechnology, 2016. **17**(9): p. 822-836.
23. Vogelstein, B. Kinzler, K.W., *Digital Pcr*. Proceedings of the National Academy of Sciences, 1999. **96**(16): p. 9236-9241.
24. Margulies, M. et al., *Genome sequencing in microfabricated high-density picolitre reactors*. Nature, 2005. **437**(7057): p. 376-380.
25. Li, X. et al., *A microchip electrophoresis-mass spectrometric platform for fast separation and identification of enantiomers employing the partial filling technique*. Journal of Chromatography A, 2013. **1318**: p. 251-256.
26. Küster, S.K. et al., *Interfacing Droplet Microfluidics with Matrix-Assisted Laser Desorption/Ionization Mass Spectrometry: Label-Free Content Analysis of Single Droplets*. Analytical chemistry, 2013. **85**(3): p. 1285-1289.
27. Harvey, D.T., *Analytical Chemistry: A Modern Approach to Analytical Science, 2nd Edition*. Journal of Chemical Education, 2006. **83**(3): p. 385.
28. Ong, S.-E. et al., *Fundamental principles and applications of microfluidic systems*. Front. Biosci, 2008. **13**: p. 2757-2773.
29. Gersten, K., *Boundary-layer theory*. 2017: Springer.
30. Holman, J.P., *Heat Transfer-Si Units-Sie*. 2002: Tata McGraw-Hill Education.
31. Atkins, P.W., De Paula, J. and Keeler, J. *Atkins' physical chemistry*. 2006.
32. Iliescu, C., *Microfluidics in glass: technologies and applications*. INFORMACIJE MIDEM-LJUBLJANA-, 2006. **36**(4): p. 204.
33. Becker, H., Locascio, L.E. *Polymer microfluidic devices*. Talanta, 2002. **56**(2): p. 267-287.
34. Wolfe, D.B., Qin, D. Whitesides, G.M. *Rapid Prototyping of Microstructures by Soft Lithography for Biotechnology*, Microengineering in Biotechnology, 2010. p. 81-107.
35. Shadpour, H. et al., *Multichannel microchip electrophoresis device fabricated in polycarbonate with an integrated contact conductivity sensor array*. Analytical chemistry, 2007. **79**(3): p. 870-878.
36. Liang, C. et al., *One-step selective-wettability modification of PMMA microfluidic devices by using controllable gradient UV irradiation (CGUI)*. Sensors and Actuators B: Chemical, 2018. **273**: p. 1508-1518.
37. Klank, H., Kutter, J.P., Geschke, O. *CO<sub>2</sub>-laser micromachining and back-end processing for rapid production of PMMA-based microfluidic systems*. Lab on a Chip, 2002. **2**(4): p. 242-246.

38. Romoli, L., Tantussi, G. Dini, G. *Experimental approach to the laser machining of PMMA substrates for the fabrication of microfluidic devices*. Optics and Lasers in Engineering, 2011. **49**(3): p. 419-427.
39. Aghvami, S.A. *et al.*, *Rapid prototyping of cyclic olefin copolymer (COC) microfluidic devices*. Sensors and Actuators B: Chemical, 2017. **247**: p. 940-949.
40. Anderson, J.R. *et al.*, *Fabrication of Topologically Complex Three-Dimensional Microfluidic Systems in PDMS by Rapid Prototyping*. Analytical Chemistry, 2000. **72**(14): p. 3158-3164.
41. Eddings, M.A., Johnson, M.A. Gale, B.K. *Determining the optimal PDMS-PDMS bonding technique for microfluidic devices*. Journal of Micromechanics and Microengineering, 2008. **18**(6): p. 067001.
42. Unger, M.A. *et al.*, *Monolithic microfabricated valves and pumps by multilayer soft lithography*. Science, 2000. **288**(5463): p. 113-116.
43. Lan, W. *et al.*, *Controllable preparation of nanoparticle-coated chitosan microspheres in a co-axial microfluidic device*. Lab on a Chip, 2011. **11**(4): p. 652-657.
44. Cramer, C., Fischer, P. Windhab, E.J. *Drop formation in a co-flowing ambient fluid*. Chemical Engineering Science, 2004. **59**(15): p. 3045-3058.
45. Liu, H., Zhang, Y. *Droplet formation in a T-shaped microfluidic junction*. Journal of applied physics, 2009. **106**(3): p. 034906.
46. Xu, J., *et al.* *Preparation of highly monodisperse droplet in a T-junction microfluidic device*. AIChE journal, 2006. **52**(9): p. 3005-3010.
47. Anna, S.L., Bontoux, N. Stone, H.A., *Formation of dispersions using "flow focusing" in microchannels*. Applied physics letters, 2003. **82**(3): p. 364-366.
48. White, J.G., *et al.* *The Structure of the Nervous System of the Nematode Caenorhabditis elegans*. Philosophical Transactions of the Royal Society of London. B, Biological Sciences, 1986. **314**(1165): p. 1-340.
49. Altun, Z.F., Herndon, L.A., Wolkow, C.A., Crocker, C., Lints, R. Hall, D.H. *WormAtlas*. WormAtlas, 2002-2019.
50. Corsi, A.K., Wightman, B. Chalfie, M. *A Transparent window into biology: A primer on Caenorhabditis elegans*, in *WormBook*, The *C. elegans* Research Community, 2015, WormBook.
51. Brenner, S., *The genetics of Caenorhabditis elegans*. Genetics, 1974. **77**: p. 71-94.
52. Huang, L. Sternberg P.W., *Genetic dissection of developmental pathways*, in *WormBook*, T.C.e.R. Community, Editor., WormBook.
53. Sulston, J.E. *et al.*, *The embryonic cell lineage of the nematode Caenorhabditis elegans*. Developmental Biology, 1983. **100**(1): p. 64-119.
54. Hart, A.C., Sims, S. and Kaplan, J.M. *Synaptic code for sensory modalities revealed by C. elegans GLR-1 glutamate receptor*. Nature, 1995. **378**(6552): p. 82-85.
55. Suzuki, H. *et al.*, *In Vivo Imaging of C. elegans Mechanosensory Neurons Demonstrates a Specific Role for the MEC-4 Channel in the Process of Gentle Touch Sensation*. Neuron, 2003. **39**(6): p. 1005-1017.

56. Chronis, N., Zimmer, M., Bargmann, C.I. *Microfluidics for in vivo imaging of neuronal and behavioral activity in Caenorhabditis elegans*. Nature Methods, 2007. **4**(9): p. 727-731.
57. Bargmann, C.I., *Genetic and cellular analysis of behavior in C. elegans*. Annual review of neuroscience, 1993. **16**(1): p. 47-71.
58. Frøkjær-Jensen, C. *et al.*, *Effects of voltage-gated calcium channel subunit genes on calcium influx in cultured C. elegans mechanosensory neurons*. Journal of Neurobiology, 2006. **66**(10): p. 1125-1139.
59. Sulston, J.E. Horvitz, H.R. *Post-embryonic cell lineages of the nematode, Caenorhabditis elegans*. Developmental Biology, 1977. **56**(1): p. 110-156.
60. Ward, S. *et al.*, *Electron microscopical reconstruction of the anterior sensory anatomy of the nematode caenorhabditis elegans*. The Journal of Comparative Neurology, 1975. **160**(3): p. 313-337.
61. Chen, B.L., Hall, D.H. Chklovskii, D.B., *Wiring optimization can relate neuronal structure and function*. Proceedings of the National Academy of Sciences of the United States of America, 2006. **103**(12): p. 4723-4728.
62. Varshney, L.R. *et al.*, *Structural properties of the Caenorhabditis elegans neuronal network*. PLoS computational biology, 2011. **7**(2): p. e1001066.
63. Kitano, H., *Computational systems biology*. Nature, 2002. **420**(6912): p. 206-210.
64. Abbott, L.F., *Theoretical Neuroscience Rising*. Neuron, 2008. **60**(3): p. 489-495.
65. Chalfie, M. *et al.*, *The neural circuit for touch sensitivity in Caenorhabditis elegans*. Journal of Neuroscience, 1985. **5**(4): p. 956-964.
66. Hart, A.C., *Behavior*, in *WormBook*, The *C. elegans* Research Community, 2006, WormBook.
67. Kaplan, J.M., *Sensory signaling in Caenorhabditis elegans*. Current Opinion in Neurobiology, 1996. **6**(4): p. 494-499.
68. Tobin, D.M Bargmann, C.I. *Invertebrate nociception: behaviors, neurons and molecules*. Developmental Neurobiology, 2004. **61**(1): p. 161-174.
69. Bargmann, C.I., Hartwig, E. Horvitz, H.R. *Odorant-selective genes and neurons mediate olfaction in C. elegans*. Cell, 1993. **74**(3): p. 515-527.
70. Hart, A.C. Chao, M.Y. *From odors to behaviors in Caenorhabditis elegans*. The neurobiology of olfaction, 2010. CRC Press/Taylor & Francis
71. Gayed, P.M., *Neuroscience*. The Yale Journal of Biology and Medicine, 2008. **81**(1): p. 54-55.
72. Richmond, J., *Synaptic function*, in *WormBook*, The *C. elegans* Research Community.,2005, WormBook.
73. Liu, Q., Hollopeter, G. Jorgensen, E.M. *Graded synaptic transmission at the Caenorhabditis elegans neuromuscular junction*. Proceedings of the National Academy of Sciences, 2009. **106**(26): p. 10823-10828.
74. Lockery, S.R. Goodman, M.B., *The quest for action potentials in C. elegans neurons hits a plateau*. Nature Neuroscience, 2009. **12**: p. 377.

75. Liu, Q. *et al.*, *C. elegans* AWA Olfactory Neurons Fire Calcium-Mediated All-or-None Action Potentials. *Cell*, 2018. **175**(1): p. 57-70.e17.
76. Majewska, A. Yuste, R, *Topology of Gap Junction Networks in C. elegans*. *Journal of Theoretical Biology*, 2001. **212**(2): p. 155-167.
77. Altun, Z.F. *et al.*, *High resolution map of Caenorhabditis elegans gap junction proteins*. *Developmental Dynamics*, 2009. **238**(8): p. 1936-1950.
78. Bennett, M.V.L. Zukin, R.S. *Electrical Coupling and Neuronal Synchronization in the Mammalian Brain*. *Neuron*, 2004. **41**(4): p. 495-511.
79. Bossinger, O. Schierenberg, E. *Cell-cell communication in the embryo of Caenorhabditis elegans*. *Developmental Biology*, 1992. **151**(2): p. 401-409.
80. Hall, D.H., *Gap junctions in C. elegans: Their roles in behavior and development*. *Developmental Neurobiology*, 2017. **77**(5): p. 587-596.
81. Labouesse, M., *Epithelial junctions and attachments*, in *WormBook*, The *C. elegans* research community, 2006, WormBook.
82. Starich, T. *et al.*, *Innexins in C. elegans*. *Cell Communication & Adhesion*, 2001. **8**(4-6): p. 311-314.
83. Bargmann, C.I., Horvitz, H.R. *Chemosensory neurons with overlapping functions direct chemotaxis to multiple chemicals in C. elegans*. *Neuron*, 1991. **7**(5): p. 729-742.
84. Chuang, C.-F. *et al.*, *An Innexin-Dependent Cell Network Establishes Left-Right Neuronal Asymmetry in C. elegans*. *Cell*, 2007. **129**(4): p. 787-799.
85. Hobert, O. *Development of left/right asymmetry in the Caenorhabditis elegans nervous system: From zygote to postmitotic neuron*. *genesis*, 2014. **52**(6): p. 528-543.
86. Suzuki, H. *et al.*, *Functional asymmetry in Caenorhabditis elegans taste neurons and its computational role in chemotaxis*. *Nature*, 2008. **454**: p. 114.
87. Alqadah, A. *et al.*, *Asymmetric development of the nervous system*. *Developmental Dynamics*, 2018. **247**(1): p. 124-137.
88. Poole, R.J., Hobert O., *Early Embryonic Programming of Neuronal Left/Right Asymmetry in C. elegans*. *Current Biology*, 2006. **16**(23): p. 2279-2292.
89. Cochella, L. Hobert, O. *Embryonic Priming of a miRNA Locus Predetermines Postmitotic Neuronal Left/Right Asymmetry in C. elegans*. *Cell*, 2012. **151**(6): p. 1229-1242.
90. Troemel, E.R., Sagasti, A. Bargmann, C.I. *Lateral signaling mediated by axon contact and calcium entry regulates asymmetric odorant receptor expression in C. elegans*. *Cell*, 1999. **99**: p. 387-398.
91. Ward, S., *Chemotaxis by the nematode Caenorhabditis elegans: identification of attractants and analysis of the response by use of mutants*. *Proceedings of the National Academy of Sciences*, 1973. **70**(3): p. 817-821.
92. Lee, J., Jee, C., McIntire S.L., *Ethanol preference in C. elegans*. *Genes, brain, and behavior*, 2009. **8**(6): p. 578-585.
93. Swierczek, N.A. *et al.*, *High-throughput behavioral analysis in C. elegans*. *Nature Methods*, 2011. **8**: p. 592.

94. Colbert, H.A. and Bargmann C.I., *Odorant-specific adaptation pathways generate olfactory plasticity in C. elegans*. 1995. **14**(4): p. 803-812.
95. Au - Kauffman, A. et al., *C. elegans Positive Butanone Learning, Short-term, and Long-term Associative Memory Assays*. JoVE, 2011(49): p. e2490.
96. Troemel, E.R., Kimmel, B.E. Bargmann,C.I., *Reprogramming Chemotaxis Responses: Sensory Neurons Define Olfactory Preferences in C. elegans*. Cell, 1997. **91**(2): p. 161-169.
97. Pierce-Shimomura, J.T., Morse, T.M., Lockery,S.R. *The Fundamental Role of Pirouettes in Caenorhabditis elegans Chemotaxis*. The Journal of Neuroscience, 1999. **19**(21): p. 9557-9569.
98. Frøkjær-Jensen, C., Ailion, M., Lockery, S.R.J.P.O. *Ammonium-acetate is sensed by gustatory and olfactory neurons in Caenorhabditis elegans*. PLOS ONE, 2008. **3**(6): p. e2467.
99. Bargmann, C., Thomas, J., Horvitz, H., *Chemosensory cell function in the behavior and development of Caenorhabditis elegans*. Cold Spring Harbor symposia on quantitative biology. 1990.
100. Sambongi, Y. et al., *Sensing of cadmium and copper ions by externally exposed ADL, ASE, and ASH neurons elicits avoidance response in Caenorhabditis elegans*. Neuroreport. 1999. **10**(4): p. 753-757.
101. Hilliard, M.A. Bargmann, C.I., Bazzicalupo, P.J.C.B. *C. elegans responds to chemical repellents by integrating sensory inputs from the head and the tail*. 2002. **12**(9): p. 730-734.
102. Hilliard, M.A. et al., *Worms taste bitter: ASH neurons, QUI-1, GPA-3 and ODR-3 mediate quinine avoidance in Caenorhabditis elegans*. 2004. **23**(5): p. 1101-1111.
103. Kaplan, J.M. Horvitz, H.R., *A dual mechanosensory and chemosensory neuron in Caenorhabditis elegans*. Proceedings of the National Academy of Sciences of the United States of America, 1993. **90**(6): p. 2227-2231.
104. Culotti, J.G. and Russell, R.L., *Osmotic avpodamce defectove mutaions fo the nematode Caenorhabditis elegans*. Genetics, 1978. **90**(2): p. 243-256.
105. Bargmann, C.I., *Chemosensation in C. elegans*, in *WormBook*, The *C. elegans* Research Community,., WormBook.
106. Hilliard, M.A. et al., *In vivo imaging of C. elegans ASH neurons: cellular response and adaptation to chemical repellents*. The EMBO Journal, 2005. **24**(1): p. 63-72.
107. Ward, A. et al., *Light-sensitive neurons and channels mediate phototaxis in C. elegans*. Nature neuroscience, 2008. **11**(8): p. 916-922.
108. Maricq, A.V. et al., *Mechanosensory signalling in C. elegans mediated by the GLR-1 glutamate receptor*. Nature, 1995. **378**(6552): p. 78-81.
109. Walker, D.S. et al., *Inositol 1, 4, 5-trisphosphate signalling regulates the avoidance response to nose touch in Caenorhabditis elegans*. 2009. **5**(9): p. e1000636.
110. Chatzigeorgiou, M. et al., *tmc-1 encodes a sodium-sensitive channel required for salt chemosensation in C. elegans*. Nature, 2013. **494**(7435): p. 95-99.

111. Rogers, C. *et al.*, *Behavioral Motifs and Neural Pathways Coordinating O<sub>2</sub> Responses and Aggregation in C. elegans*. *Current Biology*, 2006. **16**(7): p. 649-659.
112. de Bono, M. *et al.*, *Social feeding in Caenorhabditis elegans is induced by neurons that detect aversive stimuli*. *Nature*, 2002. **419**(6910): p. 899-903.
113. Pierce-Shimomura, J.T. *et al.*, *The homeobox gene lim-6 is required for distinct chemosensory representations in C. elegans*. *Nature*, 2001. **410**(6829): p. 694-698.
114. Bretscher, A.J. *et al.*, *Temperature, oxygen, and salt-sensing neurons in C. elegans are carbon dioxide sensors that control avoidance behavior*. *Neuron*, 2011. **69**(6): p. 1099-1113.
115. Appleby, P.A., *A model of chemotaxis and associative learning in C. elegans*. 2012. **106**(6): p. 373-387.
116. Milward, K. *et al.*, *Neuronal and molecular substrates for optimal foraging in Caenorhabditis elegans*. *Proceedings of the National Academy of Sciences*, 2011. **108**(51): p. 20672-20677.
117. Tomioka, M. *et al.*, *The insulin/PI 3-kinase pathway regulates salt chemotaxis learning in Caenorhabditis elegans*. *Neuron*, 2006. **51**(5): p. 613-625.
118. Shimomura, O., *Structure of the chromophore of Aequorea green fluorescent protein*. *FEBS letters*, 1979. **104**(2): p. 220-222.
119. Shimomura, O., *Discovery of Green Fluorescent Protein (GFP) (Nobel Lecture)*. *Angewandte Chemie International Edition*, 2009. **48**(31): p. 5590-5602.
120. Heim, R., Cubitt, A.B. Tsien R.Y., *Improved green fluorescence*. *Nature*, 1995. **373**(6516): p. 663-664.
121. Ormö, M. *et al.*, *Crystal structure of the Aequorea victoria green fluorescent protein*. *Science*, 1996. **273**(5280): p. 1392-1395.
122. Campbell, R.E. *et al.*, *A monomeric red fluorescent protein*. *Proceedings of the National Academy of Sciences*, 2002. **99**(12): p. 7877-7882.
123. Shaner, N.C. *et al.*, *Improved monomeric red, orange and yellow fluorescent proteins derived from Discosoma sp. red fluorescent protein*. *Nature biotechnology*, 2004. **22**(12): p. 1567.
124. Shaner, N.C., Steinbach, P.A., Tsien, R.Y., *A guide to choosing fluorescent proteins*. *Nature methods*, 2005. **2**(12): p. 905.
125. Yuste, R., *Fluorescence microscopy today*. *Nature methods*, 2005. **2**(12): p. 902.
126. Chudakov, D.M., Lukyanov, Lukyanov, S K.A., *Fluorescent proteins as a toolkit for in vivo imaging*. *Trends in biotechnology*, 2005. **23**(12): p. 605-613.
127. Livet, J. *et al.*, *Transgenic strategies for combinatorial expression of fluorescent proteins in the nervous system*. *Nature*, 2007. **450**: p. 56.
128. Nakai, J., Ohkura, M., Imoto, K., *A high signal-to-noise Ca<sup>2+</sup> probe composed of a single green fluorescent protein*. *Nature Biotechnology*, 2001. **19**: p. 137.
129. Tallini, Y.N. *et al.*, *Imaging cellular signals in the heart in vivo: Cardiac expression of the high-signal Ca<sup>2+</sup> indicator GCaMP2*. *Proceedings of the National Academy of Sciences*, 2006. **103**(12): p. 4753-4758.

130. Tian, L. *et al.*, *Imaging neural activity in worms, flies and mice with improved GCaMP calcium indicators*. *Nature methods*, 2009. **6**(12): p. 875.
131. Ohkura, M. *et al.*, *Genetically encoded green fluorescent Ca<sup>2+</sup> indicators with improved detectability for neuronal Ca<sup>2+</sup> signals*. *PLoS one*, 2012. **7**(12): p. e51286.
132. Clark, D.A. *et al.*, *Temporal Activity Patterns in Thermosensory Neurons of Freely Moving Caenorhabditis elegans Encode Spatial Thermal Gradients*. *The Journal of Neuroscience*, 2007. **27**(23): p. 6083-6090.
133. Ben Arous, J. *et al.*, *Automated imaging of neuronal activity in freely behaving Caenorhabditis elegans*. *Journal of Neuroscience Methods*, 2010. **187**(2): p. 229-234.
134. Faumont, S. *et al.*, *An Image-Free Opto-Mechanical System for Creating Virtual Environments and Imaging Neuronal Activity in Freely Moving Caenorhabditis elegans*. *PLOS ONE*, 2011. **6**(9): p. e24666.
135. Suster, M.L. *et al.*, *Targeted expression of tetanus toxin reveals sets of neurons involved in larval locomotion in Drosophila*. *Journal of Neurobiology*, 2003. **55**(2): p. 233-246.
136. Naumann, E.A. *et al.*, *Monitoring neural activity with bioluminescence during natural behavior*. *Nature Neuroscience*, 2010. **13**(4): p. 513-520.
137. Muto, A. *et al.*, *Real-Time Visualization of Neuronal Activity during Perception*. *Current Biology*, 2013. **23**(4): p. 307-311.
138. Luo, L. *et al.*, *Navigational Decision Making in Drosophila Thermotaxis*. *The Journal of Neuroscience*, 2010. **30**(12): p. 4261-4272.
139. Prevedel, R. *et al.*, *Simultaneous whole-animal 3D imaging of neuronal activity using light-field microscopy*. *Nature Methods*, 2014. **11**(7): p. 727-730.
140. Aimon, S. *et al.*, *Fast near-whole-brain imaging in adult Drosophila during responses to stimuli and behavior*. *PLOS Biology*, 2019. **17**(2): p. e2006732.
141. Perez, C.C. *et al.*, *Calcium neuroimaging in behaving zebrafish larvae using a turn-key light field camera*. *Journal of Biomedical Optics*, 2015. **20**(9): p. 1-5,
142. Cong, L. *et al.*, *Rapid whole brain imaging of neural activity in freely behaving larval zebrafish (Danio rerio)*. *Elife*, 2017. **6**: p. e28158.
143. Crittenden, S.L., Kimble, J., *Confocal Methods for Caenorhabditis elegans*, in *Confocal Microscopy Methods and Protocols*, 1999, Humana Press: Totowa, p. 141-151.
144. Venkatachalam, V. *et al.*, *Pan-neuronal imaging in roaming Caenorhabditis elegans*. *Proceedings of the National Academy of Sciences*, 2016. **113**(8): p. E1082-E1088.
145. Nguyen, J.P. *et al.*, *Whole-brain calcium imaging with cellular resolution in freely behaving Caenorhabditis elegans*. *Proceedings of the National Academy of Sciences*, 2016. **113**(8): p. E1074-E1081.
146. Chokshi, T.V., Ben-Yakar A., Chronis N., *CO<sub>2</sub> and compressive immobilization of C. elegans on-chip*. *Lab on a Chip*, 2009. **9**(1): p. 151-157.
147. Hulme, S.E. *et al.*, *A microfabricated array of clamps for immobilizing and imaging C. elegans*. *Lab on a Chip*, 2007. **7**(11): p. 1515-1523.

148. Chung, K., Crane, M.M, Lu, H., *Automated on-chip rapid microscopy, phenotyping and sorting of C. elegans*. Nat Meth, 2008. **5**(7): p. 637-643.
149. Krajniak, J., Lu H, *Long-term high-resolution imaging and culture of C. elegans in chip-gel hybrid microfluidic device for developmental studies*. Lab on a Chip, 2010. **10**(14): p. 1862-1868.
150. Shi, W. *et al.*, *Droplet-based microfluidic system for individual Caenorhabditis elegans assay*. Lab on a Chip, 2008. **8**(9): p. 1432-1435.
151. Chalasani, S.H. *et al.*, *Dissecting a circuit for olfactory behaviour in Caenorhabditis elegans*. Nature, 2007. **450**: p. 63.
152. Chokshi, T.V., Bazopoulou, D, Chronis, N., *An automated microfluidic platform for calcium imaging of chemosensory neurons in Caenorhabditis elegans*. Lab on a Chip, 2010. **10**(20): p. 2758-2763.
153. Zimmer, M. *et al.*, *Neurons detect increases and decreases in oxygen levels using distinct guanylate cyclases*. Neuron, 2009. **61**(6): p. 865-879.
154. Gourgou, E, Chronis, N., *Chemically induced oxidative stress affects ASH neuronal function and behavior in C. elegans*. Scientific Reports, 2016. **6**: p. 38147.
155. Gilleland, C.L. *et al.*, *Microfluidic immobilization of physiologically active Caenorhabditis elegans*. Nature Protocols, 2010. **5**(12): p. 1888-1902.
156. Hulme, S.E. *et al.*, *Lifespan-on-a-chip: microfluidic chambers for performing lifelong observation of C. elegans*. Lab on a Chip, 2010. **10**(5): p. 589-597.
157. Rezai, P. *et al.*, *Electrotaxis of Caenorhabditis elegans in a microfluidic environment*. Lab on a Chip, 2010. **10**(2): p. 220-226.
158. Rezai, P. *et al.*, *Electrical sorting of Caenorhabditis elegans*. Lab on a Chip, 2012. **12**(10): p. 1831-1840.
159. i Solvas, X.C. *et al.*, *High-throughput age synchronisation of Caenorhabditis elegans*. Chemical Communications, 2011. **47**(35): p. 9801-9803.
160. Ghaemi, R., *Microfluidic device for microinjection of Caenorhabditis elegans*. McMaster University Library, 2014.
161. Song, P., Dong, X., Liu, X., *A microfluidic device for automated, high-speed microinjection of Caenorhabditis elegans*. Biomicrofluidics, 2016. **10**(1): p. 011912.
162. Albrecht, D.R., Bargmann,C.I., *High-content behavioral analysis of Caenorhabditis elegans in precise spatiotemporal chemical environments*. Nature Method, 2011. **8**(7): p. 599-605.
163. Gray, J.M. *et al.*, *Oxygen sensation and social feeding mediated by a C. elegans guanylate cyclase homologue*. Nature, 2004. **430**(6997): p. 317-322.
164. McCormick, K.E. *et al.*, *Microfluidic devices for analysis of spatial orientation behaviors in semi-restrained Caenorhabditis elegans*. PloS one, 2011. **6**(10): p. e25710.
165. Mondal, S., *et al.* *Imaging in vivo Neuronal Transport in Genetic Model Organisms Using Microfluidic Devices*. Traffic, 2011. **12**(4): p. 372-385.

166. Chuang, H.-S. *et al.*, *Immobilization of the nematode caenorhabditis elegans with addressable light-induced heat knockdown (ALINK)*. Lab on a Chip, 2013. **13**(15): p. 2980-2989.
167. Krajniak, J. *et al.*, *C.L.I.P.–continuous live imaging platform for direct observation of C. elegans physiological processes*. Lab on a Chip, 2013. **13**(15): p. 2963-2971.
168. Guo, S.X., *Femtosecond laser nanoaxotomy lab-on-a-chip for in vivo nerve regeneration studies*. Nat. Methods, 2008. **5**: p. 531-533.
169. Pierce-Shimomura, J.T. *et al.*, *Genetic analysis of crawling and swimming locomotory patterns in C. elegans*. 2008. **105**(52): p. 20982-20987.
170. Evans, T.C., *Transformation and microinjection*, in *WormBook*, The C. elegans Research Community, WormBook.
171. Zhang, M. *et al.*, *A Self-Regulating Feed-Forward Circuit Controlling C. elegans Egg-Laying Behavior*. Current Biology, 2008. **18**(19): p. 1445-1455.
172. Schrödel, T. *et al.*, *Brain-wide 3D imaging of neuronal activity in Caenorhabditis elegans with sculpted light*. Nature Methods, 2013. **10**: p. 1013.
173. Tobin, D.M. *et al.*, *Combinatorial Expression of TRPV Channel Proteins Defines Their Sensory Functions and Subcellular Localization in C. elegans Neurons*. Neuron, 2002. **35**(2): p. 307-318.
174. Larsch, J. *et al.*, *High-throughput imaging of neuronal activity in Caenorhabditis elegans*. Proceedings of the National Academy of Sciences, 2013. **110**(45): p. E4266-E4273.
175. Guo, M. *et al.*, *Reciprocal inhibition between sensory ASH and ASI neurons modulates nociception and avoidance in Caenorhabditis elegans*. Nature Communications, 2015. **6**: p. 5655.
176. Ardeshiri, R. *et al.*, *A hybrid microfluidic device for on-demand orientation and multidirectional imaging of C. elegans organs and neurons*. Biomicrofluidics, 2016. **10**(6): p. 064111.
177. Ahmed, D. *et al.*, *Rotational manipulation of single cells and organisms using acoustic waves*. Nature Communication, 2016. **7**.
178. Reilly, D.K., *et al.*, *Using an Adapted Microfluidic Olfactory Chip for the Imaging of Neuronal Activity in Response to Pheromones in Male C. Elegans Head Neurons*. Journal of Visualized Experiments, 2017(127): p. 56026.
179. Hochstetter, A., *Presegmentation Procedure Generates Smooth-Sided Microfluidic Devices: Unlocking Multiangle Imaging for Everyone?* ACS Omega, 2019.
180. Hu, L., *et al.*, *Quantitative analysis of Caenorhabditis elegans chemotaxis using a microfluidic device*. Analytica Chimica Acta, 2015. **887**: p. 155-162.
181. Han, B., *et al.*, *A sorting strategy for C. elegans based on size-dependent motility and electrotaxis in a micro-structured channel*. Lab on a Chip, 2012. **12**(20): p. 4128-4134.
182. Ai, X. *et al.*, *A high-throughput device for size based separation of C. elegans developmental stages*. Lab on a Chip, 2014. **14**(10): p. 1746-1752.

183. Dong, L. *et al.*, *Versatile size-dependent sorting of C. elegans nematodes and embryos using a tunable microfluidic filter structure*. *Lab on a Chip*, 2016. **16**(3): p. 574-585.
184. Ma, H. *et al.*, *A programmable microvalve-based microfluidic array for characterization of neurotoxin-induced responses of individual C. elegans*. *Biomicrofluidics*, 2009. **3**(4): p. 044114.
185. Wen, H., Shi, W., Qin, J. *Multiparameter evaluation of the longevity in C. elegans under stress using an integrated microfluidic device*. *Biomedical microdevices*, 2012. **14**(4): p. 721-728.
186. Belfer, S.J. *et al.*, *Caenorhabditis-in-drop array for monitoring C. elegans quiescent behavior*. *Sleep*, 2013. **36**(5): p. 689-698.
187. Lionaki, E., Tavernarakis, N., *High-throughput and longitudinal analysis of aging and senescent decline in Caenorhabditis elegans*, in *Cell senescence*. 2013, Springer. p. 485-500.
188. Nghe, P. *et al.*, *Microfabricated polyacrylamide devices for the controlled culture of growing cells and developing organisms*. *PloS one*, 2013. **8**(9): p. e75537.
189. Turek, M., Besseling, J., Bringmann, H., *Agarose microchambers for long-term calcium imaging of Caenorhabditis elegans*. *JoVE (Journal of Visualized Experiments)*, 2015(100): p. e52742.
190. Cornaglia, M. *et al.*, *Automated longitudinal monitoring of in vivo protein aggregation in neurodegenerative disease C. elegans models*. *Molecular neurodegeneration*, 2016. **11**(1): p. 1.
191. Kim, N. *et al.*, *Automated microfluidic compact disc (CD) cultivation system of Caenorhabditis elegans*. *Sensors and Actuators B: Chemical*, 2007. **122**(2): p. 511-518.
192. Zhao, X. *et al.*, *Microfluidic chip-based C. elegans microinjection system for investigating cell-cell communication in vivo*. *Biosensors and Bioelectronics*, 2013. **50**: p. 28-34.
193. Brégeon, D., *et al.*, *Translational misreading: a tRNA modification counteracts a +2 ribosomal frameshift*. *Genes & development*, 2001. **15**(17): p. 2295-2306.
194. Rissin, D.M., Gorris, H.H., Walt, D.R., *Distinct and Long-Lived Activity States of Single Enzyme Molecules*. *Journal of the American Chemical Society*, 2008. **130**(15): p. 5349-5353.
195. Walt, D.R., *Optical Methods for Single Molecule Detection and Analysis*. *Analytical Chemistry*, 2013. **85**(3): p. 1258-1263.
196. Rissin, D.M., Walt, D.R., *Digital readout of target binding with attomole detection limits via enzyme amplification in femtoliter arrays*. *Journal of the American Chemical Society*, 2006. **128**(19): p. 6286-6287.
197. Sakakihara, S. *et al.*, *A single-molecule enzymatic assay in a directly accessible femtoliter droplet array*. *Lab on a Chip*, 2010. **10**(24): p. 3355-3362.
198. Engvall, E., Perlmann, P., *Enzyme-linked immunosorbent assay (ELISA) quantitative assay of immunoglobulin G*. *Immunochemistry*, 1971. **8**(9): p. 871-874.
199. Engvall, E., Perlmann, P., *Enzyme-Linked Immunosorbent Assay, Elisa. III. Quantitation of Specific Antibodies by Enzyme-Labeled Anti-Immunoglobulin in Antigen-Coated Tubes*, 1972. **109**(1): p. 129-135.
200. Yalow, R.S. Berson, S.A., *Immunoassay of endogeneous plasm insulin in man*. *Journal of Clinical Investigation*, 1960. **39**(7): p. 1157-1175.

201. Hall, M. Kazakova, I., Yao, Y.-M., *High Sensitivity Immunoassays Using Particulate Fluorescent Labels*. Analytical Biochemistry, 1999. **272**(2): p. 165-170.
202. Yang, J.M. et al., *An integrated, stacked microlaboratory for biological agent detection with DNA and immunoassays*. Biosensors and Bioelectronics, 2002. **17**(6-7): p. 605-618.
203. Rissin, D.M. et al., *Single-molecule enzyme-linked immunosorbent assay detects serum proteins at subfemtomolar concentrations*. Nature biotechnology, 2010. **28**(6): p. 595-599.
204. Kim, S.H. et al., *Large-scale femtoliter droplet array for digital counting of single biomolecules*. Lab on a Chip, 2012. **12**(23): p. 4986-4991.
205. Shim, J.-u. et al., *Ultraprapid generation of femtoliter microfluidic droplets for single-molecule-counting immunoassays*. Acs Nano, 2013. **7**(7): p. 5955-5964.
206. Kim, J.A. et al., *Magnetic bead droplet immunoassay of oligomer amyloid  $\beta$  for the diagnosis of Alzheimer's disease using micro-pillars to enhance the stability of the oil-water interface*. Biosensors and Bioelectronics, 2015. **67**: p. 724-732.
207. Tang, M.Y.H., Shum H.C., *One-step immunoassay of C-reactive protein using droplet microfluidics*. Lab on a Chip, 2016. **16**(22): p. 4359-4365.
208. Srinivasan, V., Pamula, V.K., Fair, R.B., *An integrated digital microfluidic lab-on-a-chip for clinical diagnostics on human physiological fluids*. Lab on a Chip, 2004. **4**(4): p. 310-315.
209. Institute, C.L.S., *Protocols for determination of limits of detection and limits of quantitation; approved guideline*. CLSI Document EP17-A, 2004.
210. Armbruster, D.A., Pry, T, *Limit of blank, limit of detection and limit of quantitation*. The Clinical biochemist. Reviews, 2008. **29**(Suppl 1): p. S49-S52.
211. Barker, C.F. Markmann, J.F., *Historical overview of transplantation*. Cold Spring Harbor perspectives in medicine, 2013. **3**(4): p. a014977.
212. Thiru, S., Waldmann, H., *Pathology and Immunology of transplantation and rejection*. 2001: Blackwell Science Oxford, UK.
213. Veenstra, D.L. et al., *Incidence and long-term cost of steroid-related side effects after renal transplantation*. American Journal of Kidney Diseases, 1999. **33**(5): p. 829-839.
214. de Mattos, A.M., Olyaei, A.J., Bennett, W.M., *Nephrotoxicity of immunosuppressive drugs: long-term consequences and challenges for the future*. American Journal of Kidney Diseases, 2000. **35**(2): p. 333-346.
215. Racusen, L.C. et al., *The Banff 97 working classification of renal allograft pathology*. Kidney Int, 1999. **55**(2): p. 713-723.
216. Parikh, C.R., et al., *Urine NGAL and IL-18 are Predictive Biomarkers for Delayed Graft Function Following Kidney Transplantation*. American Journal of Transplantation, 2006. **6**(7): p. 1639-1645.
217. Heidt, S., et al., *Peripheral Blood Sampling for the Detection of Allograft Rejection: Biomarker Identification and Validation*. Transplantation, 2011. **92**(1): p. 1-9.
218. Xia, Y., Whitesides, G.M., *Soft lithography*. Annual review of materials science, 1998. **28**(1): p. 153-184.

219. Edelstein, A. *et al.*, *Computer Control of Microscopes Using  $\mu$ Manager*, in *Current Protocols in Molecular Biology*. 2001, John Wiley & Sons, Inc.
220. Bolme, D.S. *et al.* *Visual object tracking using adaptive correlation filters*. in *2010 IEEE Computer Society Conference on Computer Vision and Pattern Recognition*. 2010.
221. Johnson, K.A., Goody R.S., *The Original Michaelis Constant: Translation of the 1913 Michaelis–Menten Paper*. *Biochemistry*, 2011. **50**(39): p. 8264-8269.
222. Holtze, C. *et al.*, *Biocompatible surfactants for water-in-fluorocarbon emulsions*. *Lab on a Chip*, 2008. **8**(10): p. 1632-1639.
223. Johnston, R.J. Hobert O, *A microRNA controlling left/right neuronal asymmetry in *Caenorhabditis elegans**. *Nature*, 2003. **426**: p. 845.
224. Thiele, T.R., Faumont. S. Lockery S. R., *The Neural Network for Chemotaxis to Tastants in *Caenorhabditis elegans* Is Specialized for Temporal Differentiation*. 2009. **29**(38): p. 11904-11911.
225. Goodman, M.B., *Mechanosensation, The C. elegans Research Community*, WormBook,
226. Shillaber, C.P., *Photomicrography*. 1944: John Wiley: New York.
227. Piggott, B.J. *et al.*, *The neural circuits and synaptic mechanisms underlying motor initiation in *C. elegans**. *Cell*, 2011. **147**(4): p. 922-933.
228. Wang, Q., *et al.* *Fast online object tracking and segmentation: A unifying approach*. in *Proceedings of the IEEE Conference on Computer Vision and Pattern Recognition*. 2019.
229. Chang, S., Johnston, R.J., Hobert, O., *A transcriptional regulatory cascade that controls left/right asymmetry in chemosensory neurons of *C. elegans**. *Genes & Development*, 2003. **17**(17): p. 2123-2137.
230. Diggle, P.J., *Time series; a biostatistical introduction*. 1990.
231. Pearson, K., X. *On the criterion that a given system of deviations from the probable in the case of a correlated system of variables is such that it can be reasonably supposed to have arisen from random sampling*. *The London, Edinburgh, and Dublin Philosophical Magazine and Journal of Science*, 1900. **50**(302): p. 157-175.
232. Freeman, J.V., Julious S.A.J.S., *The analysis of categorical data*. 2007. **16**(1): p. 18-21.
233. Fisher, R.A., *On the Interpretation of  $\chi^2$  from Contingency Tables, and the Calculation of P*. *Journal of the Royal Statistical Society*, 1922. **85**(1): p. 87-94.
234. Miyazaki, M. *et al.*, *Stable horizontal interface formation and separation of a water/oil flow by microfluidic reactor analyzed by direct observation and numerical simulation*. *The Open Chemical Engineering Journal*, 2011(**5**): p. 13-17.
235. Grover, W.H. *et al.*, *Monolithic membrane valves and diaphragm pumps for practical large-scale integration into glass microfluidic devices*. *Sensors and Actuators B: Chemical*, 2003. **89**(3): p. 315-323.
236. Shim, J.-u. *et al.*, *Control and measurement of the phase behavior of aqueous solutions using microfluidics*. *Journal of the American Chemical Society*, 2007. **129**(28): p. 8825-8835.
237. Shim, J.-u. *et al.*, *Controlling the contents of microdroplets by exploiting the permeability of PDMS*. *Lab on a Chip*, 2011. **11**(6): p. 1132-1137.

238. Fiedler, F, Hinz, H., *No intermediate channelling in stepwise hydrolysis of fluorescein di- $\beta$ -D-galactoside by  $\beta$ -galactosidase*. European Journal of Biochemistry, 1994. **222**(1): p. 75-81.
239. Hofmann, J., Sernetz, M, *A kinetic study on the enzymatic hydrolysis of fluoresceindiacetate and fluorescein-di- $\beta$ -d-galactopyranoside*. Analytical Biochemistry, 1983. **131**(1): p. 180-186.
240. Huang, Z., *Kinetic assay of fluorescein mono-.beta.-D-galactoside hydrolysis by .beta.-galactosidase: a front-face measurement for strongly absorbing fluorogenic substrates*. Biochemistry, 1991. **30**(35): p. 8530-8534.
241. Piraino, F. *et al.*, *A Digital–Analog Microfluidic Platform for Patient-Centric Multiplexed Biomarker Diagnostics of Ultralow Volume Samples*. ACS nano, 2016. **10**(1): p. 1699-1710.
242. Arayanarakool, R. *et al.*, *Single-enzyme analysis in a droplet-based micro- and nanofluidic system*. Lab on a Chip, 2013. **13**(10): p. 1955-1962.
243. Xue, Q., Yeung E.S., *Differences in the chemical reactivity of individual molecules of an enzyme*. Nature, 1995. **373**(6516): p. 681-683.
244. Zahid, A., *et al.*, *Optical properties study of silicone polymer PDMS substrate surfaces modified by plasma treatment*. Materials Research Express, 2017. **4**(10): p. 105301.
245. Gillett, R. and Gull, K., *Glutaraldehyde—its purity and stability*. Histochemie, 1972. **30**(3): p. 162-167.
246. Cantarero, L.A., J.E. Butler, and J.W. Osborne, *The adsorptive characteristics of proteins for polystyrene and their significance in solid-phase immunoassays*. Analytical Biochemistry, 1980. **105**(1): p. 375-382.
247. Choe, W., T.A. Durgannavar, and S.J. Chung, *Fc-Binding Ligands of Immunoglobulin G: An Overview of High Affinity Proteins and Peptides*. Materials, 2016. **9**(12): p. 994.
248. Lee, C.-Y., *et al.*, *Microfluidic mixing: a review*. International journal of molecular sciences, 2011. **12**(5): p. 3263-3287.